Mathematical Biosciences 360 (2023) 109012

Contents lists available at ScienceDirect

Mathematical Biosciences

journal homepage: www.elsevier.com/locate/mbs

Original Research Article

Coupling dynamics of 2D Notch-Delta signalling

Francisco Berkemeier [a,*], Karen M. Page [b]

[a] Department of Pathology, University of Cambridge, UK
[b] Department of Mathematics and IPLS, University College London, UK

ARTICLE INFO

Keywords:
Notch
Signalling
Stability
Protrusions
Lateral inhibition

ABSTRACT

Understanding pattern formation driven by cell–cell interactions has been a significant theme in cellular biology for many years. In particular, due to their implications within many biological contexts, lateral-inhibition mechanisms present in the Notch-Delta signalling pathway led to an extensive discussion between biologists and mathematicians. Deterministic and stochastic models have been developed as a consequence of this discussion, some of which address long-range signalling by considering cell protrusions reaching non-neighbouring cells. The dynamics of such signalling systems reveal intricate properties of the coupling terms involved in these models. In this work, we investigate the advantages and drawbacks of a single-parameter long-range signalling model across diverse scenarios. By employing linear and multi-scale analyses, we discover that pattern selection is not only partially explained but also depends on nonlinear effects that extend beyond the scope of these analytical techniques.

1. Introduction

In epithelial tissue, depending on the nature of the contact between cells, the Notch-Delta signalling pathway leads to fundamentally different patterns [1–3]. In highly packed epithelial layers, some cells have the ability to create extensions of themselves, developing protrusions that reach non-neighbouring cells and yielding a new and fundamental factor in the signalling dynamics. These basal actin-based filopodia are elongated and oriented in different directions, extending signalling to second or third neighbour cells [4–8].

In recent years, long-range signalling via filopodia has been shown to significantly impact the distribution and sparse patterning of sensory organ precursor (SOP) cells in the fly notum [9–11]. In other work, spatiotemporal patterns of spinal neuron differentiation were revealed to be mediated by basal protrusions [12]. In contrast to the frequently observed short-ranged patterns induced by short-range signalling, cell protrusions result in sparser SOP cell patterning.

The stochastic nature of these biological systems crucially affects patterning. For example, noise arising from dynamic protrusions has been shown to have a significant role in pattern refinement when studying the organisation of bristles on the *Drosophila melanogaster* notum [9]. A cellular automaton model of cell–cell signalling revealed that rule-dependent structured noise also triggers refined and biased patterning [10], hinting at the self-organising nature of such systems. Intrinsic noise, driven by stochastic gene expression, has been studied via the Chemical Langevin Equation [13] and shown to directly affect juxtacrine-based pattern formation [14].

In addition to constructing realistic long-range signalling models capable of numerically describing long-range patterning, linear stability analysis (LSA) has revealed inherent characteristics of lateral inhibition models [15–17]. Biased and long-range signalling was also studied in [18], where weight-based coupling functions were considered for several one-dimensional signalling systems. We aim to partially extend this work by studying the two-dimensional hexagonal array under specific signalling weights.

In 1996, Joanne Collier and colleagues developed the first model of Notch-mediated lateral inhibition [19]. In this work, the authors considered purely juxtacrine signalling dynamics, where the signalling cell and the target cell are in direct physical contact. We define a model of long-range Notch-Delta signalling, which is a relative weight-based extension of the original Collier model, and name it the ϵ-Collier model. We introduce a weighting parameter ϵ that relatively weights juxtacrine and long-range signalling contributions, creating a complex non-local signalling network.

Under different filopodium behaviour and lifespan assumptions, one can explore the robustness of the extended Collier model via LSA, providing a general framework for analysing autonomous systems of signalling cells, as detailed in Supplementary Note 1 (SN1). Furthermore, such a parameterised model allows us to investigate the limits on cell coupling sufficient to obtain long-range patterns. In parallel, we explore the effects of stochastic filopodium dynamics on patterning. Finally, we expand some of the techniques from LSA to describe a general framework for multiple-scale methods and weakly nonlinear

* Correspondence to: Department of Pathology, University of Cambridge, 10 Tennis Court Road, Cambridge, CB2 1QP, UK.
E-mail address: fp409@cam.ac.uk (F. Berkemeier).

https://doi.org/10.1016/j.mbs.2023.109012

Available online 2 May 2023

stability analysis (WNSA) of coupled and decoupled dynamical systems (SN2).

In this paper, we first present the Collier model of Notch-Delta signalling, followed by its extension to long-range signalling, which we call the ϵ-Collier model. We then perform a linear stability analysis of this system. The results of the LSA are compared with numerical simulations. The cases of longer/oriented protrusions and stochastic protrusions are analysed. In the latter case, we assume that protrusions link and unlink at random. Stochastic protrusions can lead to pattern refinement over time. We perform a numerical bifurcation analysis of the ϵ-Collier model, showing which modes are expected to grow near a bifurcation, and show that these accurately predict the results of numerical simulations there. Finally, we present a multiscale method for analysing weakly nonlinear dynamics, and show that it is difficult to apply to this system.

2. Main methods

2.1. Lateral inhibition

We consider a periodic $N \times M$ hexagonal lattice (hexagonal torus), where each cell has 6 neighbouring cells (see Fig. 1(a)). For a given cell, we assume juxtacrine signalling occurs with all 6 of its neighbours via the usual Collier model [19]. Here, the authors used experimental data to build an ordinary differential equation (ODE) model of the feedback loop between two adjacent cells induced by Notch signalling (lateral inhibition). The model consists of a system of coupled ODEs per cell. Denoting by n_i and d_i the levels of Notch and Delta activity in cell i, we have the following system

$$\frac{d}{dt}n_i = f(\langle d_i \rangle) - n_i \tag{1}$$

$$\frac{d}{dt}d_i = \nu(g(n_i) - d_i), \tag{2}$$

where $f, g : [0,\infty) \to [0,\infty)$ are continuous increasing and decreasing functions, respectively, often taken to be Hill functions

$$f(x) = \frac{x^k}{a + x^k} \tag{3}$$

$$g(x) = \frac{1}{1 + bx^h} \tag{4}$$

for $x \geq 0$ and $h, k \geq 1$. $r_t \equiv 1/a$ and b are the trans-interactions strength and ligand inhibition strength parameters, respectively[1]. $\nu > 0$ is the ratio between Notch and Delta decay rates, determining the strength of decay. Finally, $\langle d_i \rangle$ is the average level of Delta activity in the cells adjacent to cell i, that is,

$$\langle d_i \rangle = \frac{1}{|\mathbf{nn}(i)|} \sum_{j \in \mathbf{nn}(i)} d_j, \tag{5}$$

where the sum is taken over the nearest neighbours $\mathbf{nn}(i)$ of cell i and $|\mathbf{nn}(i)|$ is the total number of neighbours. In general, depending on the hexagonal lattice orientation, either N or M must be even to ensure periodicity. From the previous equations, one can see that the rate of production of Notch activity is an increasing function of the level of Delta activity in neighbouring cells. In contrast, the rate of production of Delta activity is a decreasing function of the level of activated Notch within the same cell. The production of Notch and Delta activity is balanced by decay.

[1] The quantity $a^{1/k}$ is the neighbour Delta activity level necessary for half-maximal Notch activation, while $b^{-1/h}$ is the Notch activity level necessary for half-maximal Delta inhibition.

2.2. Long-range signalling

In addition to lateral cell–cell signalling, we also consider the possibility of long-range signalling with respect to non-neighbouring cells. We loosely refer to cell protrusions as the main mechanism for general, isotropic long-range signalling, interchangeably using these terms. A detailed discussion of protrusion dynamics is presented in [20]. For now, our notion of protrusions remains relatively abstract. There are several ways to implement protrusion-cell signalling. As a first simplification, we assume $\langle d_i \rangle$ is the only term affected by long-range signalling and extend its definition to include non-neighbouring cells that contact cell i. We also investigate the cases where ligand density decays with distance and protrusions are stochastic.

In general, we consider the approach suggested in [18]. Here, the authors used a weighting function $\omega(s,r)$ defining the signalling level from a signaller cell s to a receiver cell r. ω determines which cells are connected through protrusions, defining a connectivity matrix whose entries yield the signalling intensity. In a simplistic protrusion model, all non-zero entries of such a matrix are equal. The weighting function ω captures the matrix information, and we may rewrite the interaction term as follows

$$\langle d_i \rangle = \sum_{j \in \mathbf{n}(i)} \omega(i,j) d_j, \tag{6}$$

where the sum is made over the neighbours of i, $\mathbf{nn}(i)$, and the non-neighbouring cells that are reached by the protrusions, $\mathbf{np}(i)$, of cell i. Such an array of indexes is defined as $\mathbf{n}(i) = \mathbf{nn}(i) \cup \mathbf{np}(i)$. The further assumption that each cell has a finite amount of active ligand to distribute at any given time point results in the following restriction

$$\sum_{j \in \mathbf{n}(i)} \omega(i,j) = \overline{\omega} < +\infty. \tag{7}$$

Although there is some freedom in the interpretation of $\overline{\omega}$, we assume $\overline{\omega} = 1$ for simplicity.

2.3. The ϵ-Collier model

Our model, hereafter named the ϵ-Collier model, extends the mathematical systems in [19] by considering the inclusion of long-range signalling via protrusions balanced by the relative weighting factor $\epsilon \in [0,1]$. We begin by weighting each signalling contribution, juxtacrine (ω_J) and protrusion-based (ω_P), by the factor ϵ, to define the combined weighting function

$$\omega \equiv (1-\epsilon)\omega_J + \epsilon\omega_P. \tag{8}$$

Eq. (6)–Eq. (8) define the ϵ-Collier model, considering protrusions of relative signalling intensity ϵ. Naturally, Eq. (8) is only interesting when ω_J and ω_P are restricted to $\mathbf{nn}(i)$ and $\mathbf{np}(i)$, respectively. For example, the case $\epsilon = 0$ and $\omega_J(i,j) = \chi_{\mathbf{nn}(i)}(j)/6$, where $\chi_{\mathbf{nn}(i)}$ is the indicator (or characteristic) function of the set $\mathbf{nn}(i)$, corresponds to the original Collier model.

2.4. Coupling dynamics

We perform a linear stability analysis to understand the criteria for pattern formation driven by Notch-Delta signalling. This is a useful tool to not only identify the regions of the parameter space for which spontaneous patterning of SOP cells occurs but also to determine the typical spacing between Delta-expressing cells, often called the characteristic length of the pattern or pattern wavelength [15,17,19]. Our analysis closely follows the methods outlined in [18,19,21] and Murray [22], for the two-dimensional hexagonal array, and is based on the framework presented in SN1.

Eq. (1)–Eq. (2) possesses a single positive homogeneous steady state (n^*, d^*). At this state, we have $f(g(n^*)) = n^*$ and $g(n^*) = d^*$, which is unique because $f(g(n))$ is monotonically decreasing for all $n \geq 0$. Then,

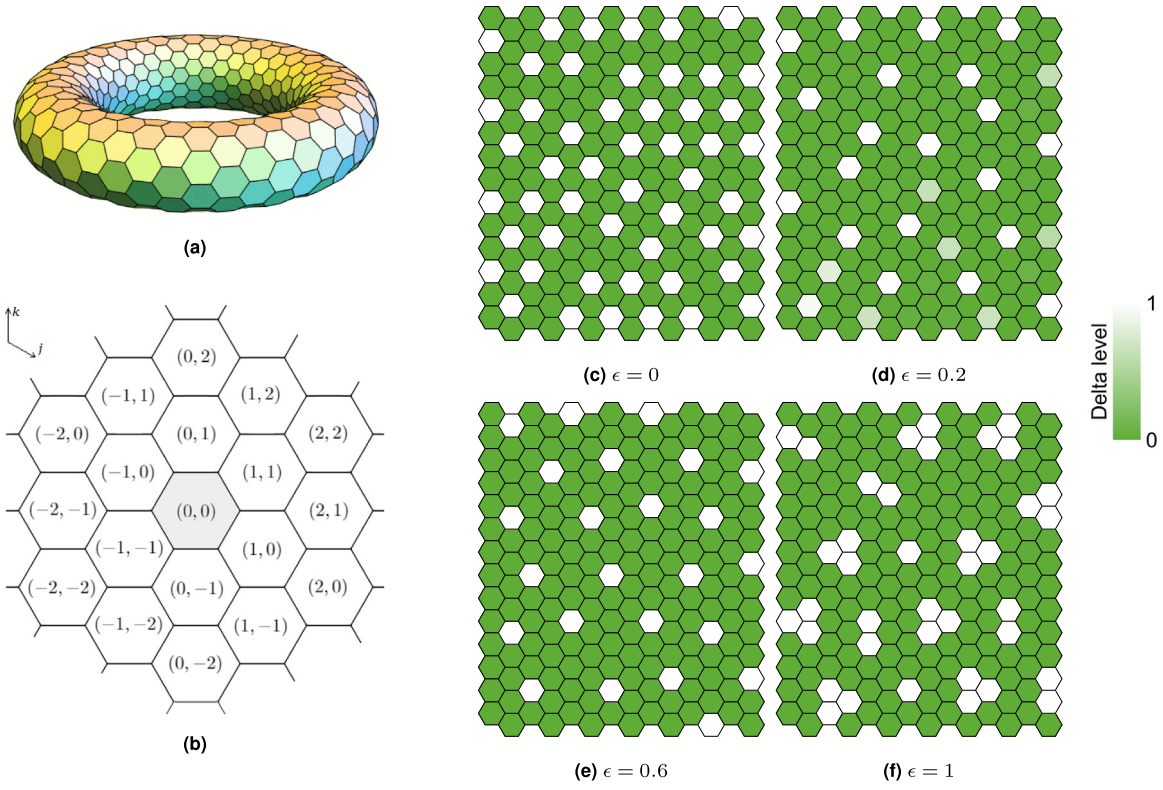

Fig. 1. Long-range Notch-Delta signalling on hexagonal lattices.
(a) Hexagonal torus. Periodic hexagonal lattices can be seen as hexagonal tori. **(b)** Hexagonal lattice main directions (j, k axes) and cell position indexation relative to a focal cell $(0, 0)$. Different cell labelling schemes yield equivalent formulations of $\Omega_{\bar{q},\bar{p}}$, as defined in Eq. (17). **(c–f)** Notch-Delta patterns on a 14×14 periodic lattice for varying ϵ. SOP cells (white, high Delta, low Notch) contrast with non-SOP cells (green, low Delta, high Notch). Here, $h = k = 6$, $a = 10^{-8}$, $b = 10^{2}$, and $\nu = 1$. Initial conditions $n_i(0)$ and $d_i(0)$ have arbitrary values close to the homogeneous steady state $(n^*, d^*) \simeq (0.744, 0.055)$.

for small perturbations $\tilde{n}_i = n_i - n^*$ and $\tilde{d}_i = d_i - d^*$, linearisation leads to

$$\frac{d}{dt}\tilde{n}_i = A\langle\tilde{d}_i\rangle - \tilde{n}_i \tag{9}$$

$$\frac{d}{dt}\tilde{d}_i = \nu B\tilde{n}_i - \nu\tilde{d}_i, \tag{10}$$

where $A = f'(g(n^*))$ is the signal trans-activation by the ligand and $B = g'(n^*)$ is the ligand inhibition by the signal. For a $N \times M$ periodic hexagonal lattice, with $1 \le j \le N$ and $1 \le k \le M$, the perturbations can be written as a discrete Fourier series

$$\tilde{n}_i \equiv \tilde{n}_{j,k} = \sum_{q=1}^{N}\sum_{p=1}^{M} \xi_{q,p} e^{2\pi \mathrm{i}(qj/N + pk/M)} \tag{11}$$

$$\tilde{d}_i \equiv \tilde{d}_{j,k} = \sum_{q=1}^{N}\sum_{p=1}^{M} \eta_{q,p} e^{2\pi \mathrm{i}(qj/N + pk/M)}, \tag{12}$$

where two subindexes have been used to refer to the spatial position of cell i within the two-dimensional hexagonal lattice (see Fig. 1(b)). For $1 \le q \le N$ and $1 \le p \le M$, the inverted transform is

$$\xi_{q,p} = \frac{1}{MN}\sum_{k=1}^{M}\sum_{j=1}^{N} \tilde{n}_{j,k} e^{-2\pi \mathrm{i}(qj/N + pk/M)} \tag{13}$$

$$\eta_{q,p} = \frac{1}{MN}\sum_{k=1}^{M}\sum_{j=1}^{N} \tilde{d}_{j,k} e^{-2\pi \mathrm{i}(qj/N + pk/M)}. \tag{14}$$

Finally, applying this change of variables to Eq. (9)–Eq. (10) leads to the following linear system of coupled ordinary differential equations

$$\frac{d}{dt}\begin{pmatrix}\xi_{q,p}\\ \eta_{q,p}\end{pmatrix} = L\begin{pmatrix}\xi_{q,p}\\ \eta_{q,p}\end{pmatrix}, \tag{15}$$

where matrix L is a specification of matrix $\mathbf{L}_{\bar{q},\bar{p}}$ in Eq. (S43), defined as

$$L = \begin{pmatrix} -1 & A\Omega_{\bar{q},\bar{p}} \\ \nu B & -\nu \end{pmatrix} \tag{16}$$

and $\Omega_{\bar{q},\bar{p}}$ is the function that takes into account the spatial coupling terms of Eq. (9)–Eq. (10) within the hexagonal lattice (in this case, $\Omega_{\bar{q},\bar{p}} \propto \left[\boldsymbol{\Omega}_{\bar{q},\bar{p}}\right]_{12}$, defined by Eq. (S42)). We have then turned Eq. (1)–Eq. (2) into a system of constant-coefficient linear differential equations described by Eq. (15), which has a straightforward family of solutions. For now, however, we focus on the coupling function $\Omega_{\bar{q},\bar{p}}$, which holds the main mechanisms behind the dynamics of juxtacrine and long-range signalling in our system.

$\Omega_{\bar{q},\bar{p}}$ varies according to the weighting function ω. Here, $\bar{q} = q/N$ and $\bar{p} = p/M$ define the discrete wavenumbers (Fourier modes) and thus solutions for $0 < \bar{q}, \bar{p} \le 1$ correspond to patterned solutions with corresponding pattern wavelengths $(1/\bar{q}, 1/\bar{p})$. We assume that connections between cells depend only on their relative positions in the lattice (Fig. 1(b)) and therefore, for a sender cell s in position (j, k) and a receiver cell r in position (j', k'), we set $\omega(s_{j,k}, r_{j',k'}) \equiv \omega(j'-j, k'-k) = \omega(\Delta j, \Delta k)$. Hence, $\Omega_{\bar{q},\bar{p}}$ is, in general, given by

$$\Omega_{\bar{q},\bar{p}} = \sum_{\Delta jk \in S} \omega(\Delta j, \Delta k) e^{2\pi \mathrm{i}(\bar{q}\Delta j + \bar{p}\Delta k)}, \tag{17}$$

where $\Delta jk = (\Delta j, \Delta k)$. Now, if we assume connections are symmetric, i.e, $\omega(\Delta j, \Delta k) = \omega(-\Delta j, -\Delta k)$, we have, by Example 1.1 in SN1,

$$\Omega_{\bar{q},\bar{p}} = \sum_{\Delta jk \in S} \omega(\Delta j, \Delta k)\cos(2\pi(\bar{q}\Delta j + \bar{p}\Delta k)). \tag{18}$$

The diagonalisation of L leads to the temporal eigenvalues

$$\lambda^{\pm}_{\bar{q},\bar{p}} = \frac{1}{2}\left[-(1+\nu) \pm \sqrt{(1+\nu)^2 - 4\nu(1 - AB\Omega_{\bar{q},\bar{p}})}\right]. \tag{19}$$

Then, since $\nu > 0$, $\lambda^{+}_{\bar{q},\bar{p}}$ is a positive real number if and only if $AB\Omega_{\bar{q},\bar{p}} > 1$. A and B are the slopes of the feedback functions f and g at the homogeneous steady state and $|AB|$ is defined as the feedback strength. If $|AB| = 0$, then the homogeneous solution is linearly stable, $\mathrm{Re}(\lambda^{\pm}_{\bar{q},\bar{p}}) < 0$, and thus no periodic pattern is expected to emerge. On the other hand, the feedback strength has to be sufficiently high for patterns to arise, that is, $|AB| > |1/\Omega_{\min}|$, where $\Omega_{\min}$ denotes the minimum of the real function $\Omega_{\bar{q},\bar{p}}$, so that $\mathrm{Re}(\lambda^{+}_{\bar{q},\bar{p}})$ is maximal. With $A > 0$, $B < 0$ and assuming $\Omega_{\min} < 0$, we expect patterned solutions provided

$$AB < \frac{1}{\Omega_{\min}}. \tag{20}$$

In particular, this feedback is controlled by the tuple (a, b, h, k) as follows

$$A = f'(g(n^*)) = \frac{akd^{*k-1}}{(a + d^{*k})^2} \tag{21}$$

$$B = g'(n^*) = -\frac{bhn^{*h-1}}{(1 + bn^{*h})^2}, \tag{22}$$

where, again, (n^*, d^*) is the homogeneous steady state, $r_t = 1/a$ is the trans-interactions strength and b is the ligand inhibition strength. (n^*, d^*) can be found by setting $\langle d_i \rangle = d_i$ and finding the intersection of the nullclines $n_i = f(d_i)$ and $d_i = g(n_i)$. Assuming for convenience $h = k$, this can be rewritten as

$$n^* = f(g(n^*)) \tag{23}$$

$$d^* = g(n^*), \tag{24}$$

which can be numerically solved for each triple (h, r_t, b) in the parameter space. Such a solution, together with Eq. (20), defines the discrete analogues of Turing spaces consisting of $r_t - b = h$ parameter regions where spontaneous patterns occur. Outside such regions, pattern formation is not expected, since all of the linear modes have negative growth rates.

We now explore different weighting functions to capture the effects of juxtacrine signalling and protrusions, and discuss what features of ω affect $\Omega_{\min}$. We recall that ω determines the family of systems Eq. (1)–Eq. (2) via the weighting dynamics defined by Eq. (6)–Eq. (8).

For a given cell on a hexagonal lattice, we denote the closest ring of order $k \in \mathbb{N}_0$ by R_k, such that R_0 the cell itself, R_1 are its 6 neighbouring cells, R_2 is the ring of 12 second-neighbour cells, and so forth. Notice that $|R_k| = 6k$ $(k > 0)$. We further expand the definition of S in SN1 by defining S_k as the relative index set of cells in R_k (according to Fig. 1(b)), that is,

$$\begin{cases} S_0 = \{(0,0)\} \\ S_1 = \{(\pm 1, 0), (0, \pm 1), \pm(1,1)\} \\ S_2 = \{(0, \pm 2), (\pm 2, 0), \pm(1,-1), \\ \qquad \pm(1,2), \pm(2,1), \pm(2,2)\} \\ \quad \vdots \end{cases} . \tag{25}$$

This notation will be used throughout this work. Notice that such a definition can be ambiguous in different contexts, as discussed in Remark 1.2 (SN1).

3. Results

3.1. Juxtacrine signalling and simplistic protrusions

For juxtacrine signalling on a hexagonal lattice, without protrusions, we set

$$\omega_J(\Delta j, \Delta k) = \begin{cases} \frac{1}{6} & \text{if } (\Delta j, \Delta k) \in S_1, \\ 0 & \text{otherwise,} \end{cases} \tag{26}$$

so that

$$\Omega_{\bar{q},\bar{p}} = \frac{1}{3}\left[\cos(2\pi\bar{q}) + \cos(2\pi\bar{p}) + \cos(2\pi(\bar{q}+\bar{p}))\right]. \tag{27}$$

Notice that $\Omega_{\bar{q},\bar{p}}$ takes discrete values within the interval $[-0.5, 1]$. The modes that minimise Eq. (27) are those for which N and M are multiples of 3, thus $(\bar{q}, \bar{p}) \in \{(1/3, 1/3), (2/3, 2/3)\}$ and a pattern with wavelength 3 along the main directions of the hexagonal lattice emerges, provided $AB < -2$. In general, and depending on the initial conditions, such patterns may yield 1, 2 or 3 different cell types, as discussed in more detail below.

Considering protrusions, we first look at the more straightforward case where only the first ring of 12 non-neighbouring cells, R_2, is reached by protrusions. Here, signalling is weighted laterally by Eq. (26) and on R_2 by

$$\omega_P(\Delta j, \Delta k) = \begin{cases} \frac{1}{12} & \text{if } (\Delta j, \Delta k) \in S_2, \\ 0 & \text{otherwise.} \end{cases} \tag{28}$$

Figs. 1(c)–1(f) show the observable patterns for different values of ϵ, with initial conditions near the homogeneous steady state, obtained by solving Eq. (23)–Eq. (24). Notice that the limit case $\epsilon = 1$ has the extreme feature of no juxtacrine signalling, hence the small clusters of Delta-expressing cells in Fig. 1(f). Even for small values of ϵ, sparse patterns are evident.

We may then weight each signalling contribution with a factor $\epsilon > 0$ and define the combined weighting function $\omega = (1-\epsilon)\omega_J + \epsilon\omega_P$. Using this leads to

$$\begin{aligned} \Omega_{\bar{q},\bar{p}} = {} & \frac{(1-\epsilon)}{3}\left[\cos(2\pi\bar{q}) + \cos(2\pi\bar{p}) + \cos(2\pi(\bar{q}+\bar{p}))\right] \\ & + \frac{\epsilon}{6}\Big[\cos(4\pi\bar{q}) + \cos(2\pi(\bar{p}-\bar{q})) + \cos(4\pi\bar{p}) \\ & \quad + \cos(2\pi(2\bar{q}+\bar{p})) + \cos(2\pi(\bar{q}+2\bar{p})) \\ & \quad + \cos(4\pi(\bar{q}+\bar{p}))\Big]. \end{aligned} \tag{29}$$

In this case, minimising $\Omega_{\bar{q},\bar{p}}$ is trickier and therefore we consider a numerical approach. For different values of the long-range signalling strength ϵ, Fig. 2(a) shows the change of $1/|\Omega_{\min}|$ for increasing values of ϵ. Notice that $\Omega_{\max} = 1$ for all ϵ. Equal juxtacrine-protrusion weighting occurs when $\epsilon = 2/3$ $(\Omega_{\min}(2/3) \simeq -0.24)$. For each ϵ, the number of modes varies, as seen in Fig. 2(b). Notice that $\Omega_{\bar{q},\bar{p}} = \Omega_{1-\bar{q},1-\bar{p}}$ and, in fact, $\Omega_{\bar{q},\bar{p}}$ is symmetric with respect to the planes $\bar{q} = \bar{p}$ and $\bar{q} = 1 - \bar{p}$ for all ϵ. An interesting observation is that at around $\epsilon = 0.4$ there are a total of 8 minimising modes, contrasting to the single pair of modes for $\epsilon < 0.4$ and the 6 distinct modes for $\epsilon > 0.4$ (Figs. 2(d)–2(f), Video S1). The bifurcation observed in Fig. 2(b) at $\epsilon = 0.4$ is predicted independently of the Hill functions, and can be mathematically shown by solving, for ϵ,

$$\Omega_{\frac{1}{3},\frac{1}{3}}(\epsilon) = \Omega_{\bar{q},\bar{p}}(\epsilon) \tag{30}$$

and a minimising pair $(\bar{q}, \bar{p}) \notin \{(1/3, 1/3), (2/3, 2/3)\}$ (see SN1 for details). Figs. 2(g)–2(i) show some of the simulations for corresponding values of ϵ.

As discussed before, the critical wave numbers maximise the real part of the temporal eigenvectors. Equivalently, Fig. 2(c) shows $\max_{\bar{q},\bar{p}} \mathrm{Re}(\lambda^{\pm}_{\bar{q},\bar{p}})$ as a function of the relative weight parameter ϵ, corresponding to the critical $AB = 1/(\max_{\epsilon} \Omega_{\min}) \simeq -5.207$. Here, $\max_{\bar{q},\bar{p}}(\mathrm{Re}(\lambda^{\pm}_{\bar{q},\bar{p}})) > 0$ for all ϵ, and thus patterns are expected to emerge with the maximising wavelength modes. As suggested by Eq. (21)–Eq. (24), we may go a step further and work out the specific parameter regions for which $|AB|$ yields pattern formation. The phase diagrams in Fig. 3 (Video S2) represent the regions in the $r_t - b$ plane such that $AB < 1/\Omega_{\min}(\epsilon)$, or more specifically,

$$n^{*1-h} d^{*1-k}((1 + bn^{*h})(a + d^{*k}))^2 < -abhk\Omega_{\min}(\epsilon) \tag{31}$$

for different values of $\Omega_{\min}$ and corresponding ϵ. The ϵ-Collier model is robust with respect to the pair (r_t, b), corresponding to the trans-interactions strength and ligand inhibition strength parameters, respectively. Increasing ϵ from zero initially reduces the size of the discrete

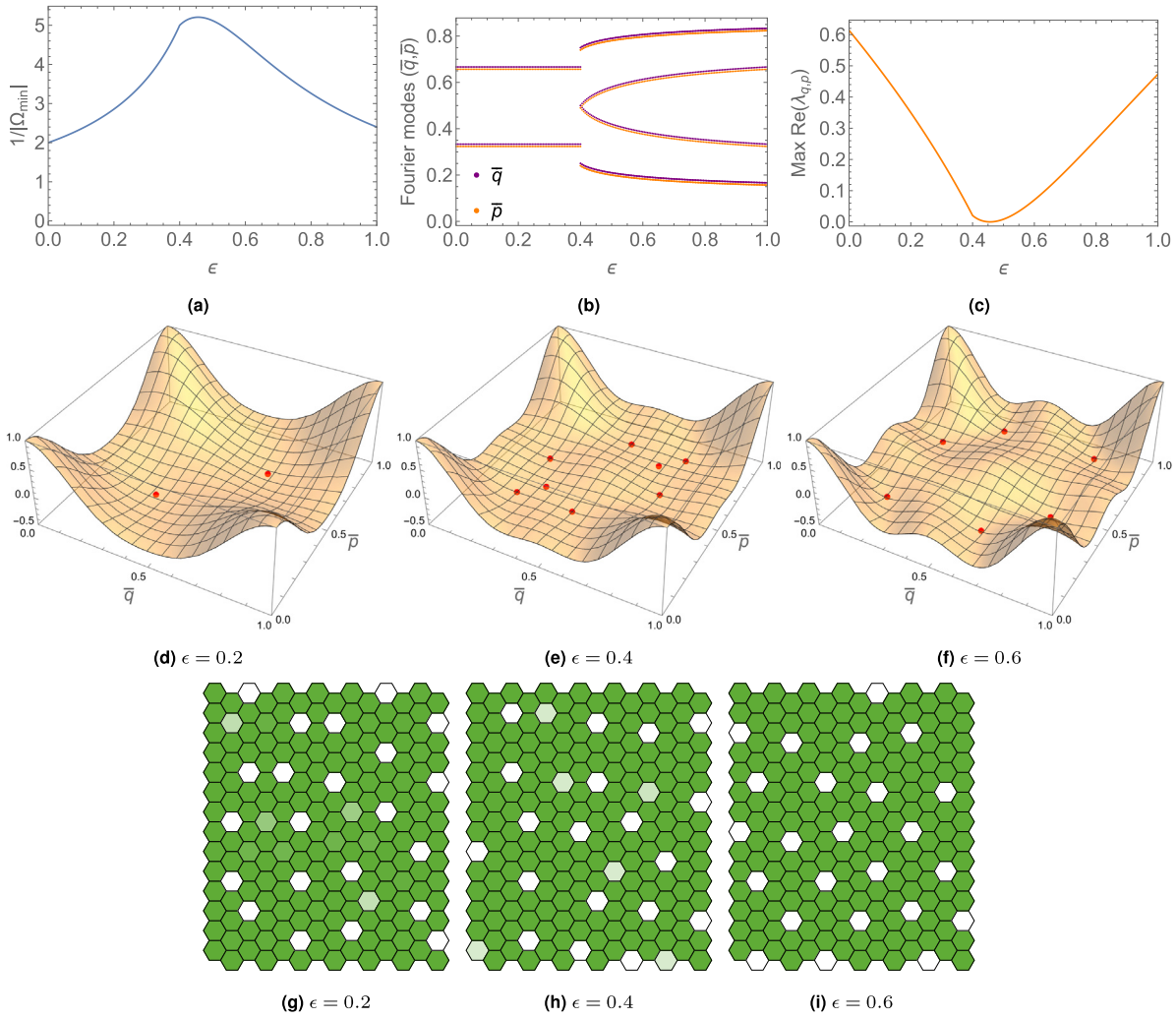

Fig. 2. Coupling dynamics of simplistic protrusions as functions of ϵ.
(a) $1/|\Omega_{\min}|$. In this case, $(\bar{q},\bar{p})|_{\epsilon=0} \in \{(1/3,1/3),(2/3,2/3)\}$ and $\max_\epsilon \Omega_{\min} \simeq -0.192$. **(b)** Plot of the fastest growing modes $(\bar{q},\bar{p})$. $\bar{q}$ (purple) and $\bar{p}$ (orange, artificially shifted) have identical plots. **(c)** Maximum value of $\mathrm{Re}(\lambda^{\pm}_{\bar{q},\bar{p}})$ as function of ϵ, with $AB = 1/(\max_\epsilon \Omega_{\min}) \simeq -5.207$. **(d–f)** Plot of $\Omega_{\bar{q},\bar{p}}$ and respective minimising modes (in red). **(g–i)** Simulations on a 14×14 lattice for different values of ϵ. Parameters similar to Fig. 1 (see Table 1 in Supplementary Note 3).

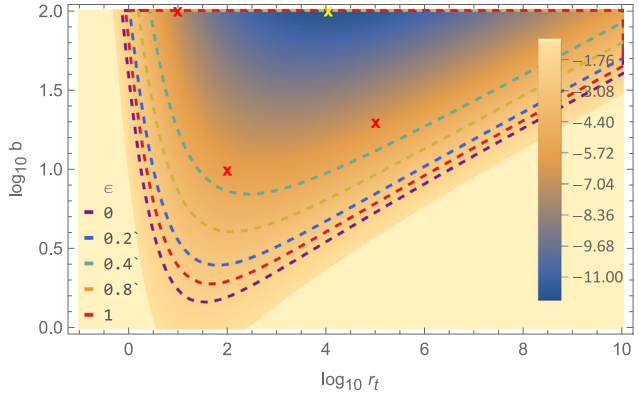

Fig. 3. Phase diagrams.
Log–log contour plot of AB as a function of r_t, b. The regions delimited by the dashed lines indicate the Turing spaces where spontaneous pattern formation occurs ($AB < 1/\Omega_{\min}(\epsilon)$), for each $\epsilon \in \{0, 0.2, 0.4, 0.8, 1\}$. Here, $h = k = 6$. In this region, $\min_{r_t,b} AB \simeq -11.986$ at $(r_t, b) \simeq (10^{4.041}, 10^2)$ (yellow cross). The purple line corresponds to $AB = -2$ ($\epsilon = 0$). Red crosses indicate the critical points $(r_t, b) \in \{(10, 10^2), (10^2, 10), (10^5, 10^{1.3})\}$. Parameter values are shown in Table 1.

Turing space, in which patterning occurs, followed by an increase after intermediate values of ϵ ($\Omega_{\min}(\epsilon)$ has a maximiser at $\epsilon \simeq 0.455$), which is in accordance with the monotonicity change of $1/|\Omega_{\min}|$ (Fig. 2(a)). Note that Turing spaces for different values of ϵ are strictly contained sets, via Eq. (31). In the region $(r_t, b) \in [10^{-1}, 10^{10}] \times [10^0, 10^2]$, patterns emerge for any ϵ, since there are always non-empty Turing spaces ($\min_{r_t,b} AB \simeq -11.986 < -5.207 \simeq 1/\max_\epsilon \Omega_{\min}$). As discussed below, we are interested in the dynamics near bifurcations, where LSA is expected to better predict pattern selection. In particular, we highlight three critical points $(r_t, b) \in \{(10, 10^2), (10^2, 10), (10^5, 10^{1.3})\}$ (red crosses in Fig. 3), for later reference.

Patterning timing is also affected by relative weighting. To measure it, we define a constraint that ensures that the overall change in activity across the lattice does not exceed a certain limit. This can be interpreted as a control mechanism that prevents rapid and drastic changes in Delta activity levels, which could be indicative of unstable or erratic behaviour in the system. We define patterning time as the instant t for which

$$\frac{1}{NM} \sum_{j,k} |d_{j,k}(t) - d_{j,k}(t-1)| \leq \overline{d} \tag{32}$$

holds, for some threshold $\overline{d}$. With $\overline{d} \simeq 0.001$, Fig. S5 shows that patterning converges fast for different ranges of ϵ depending on the critical points. On 14×14 lattices, patterning is slower around $0.35 <$

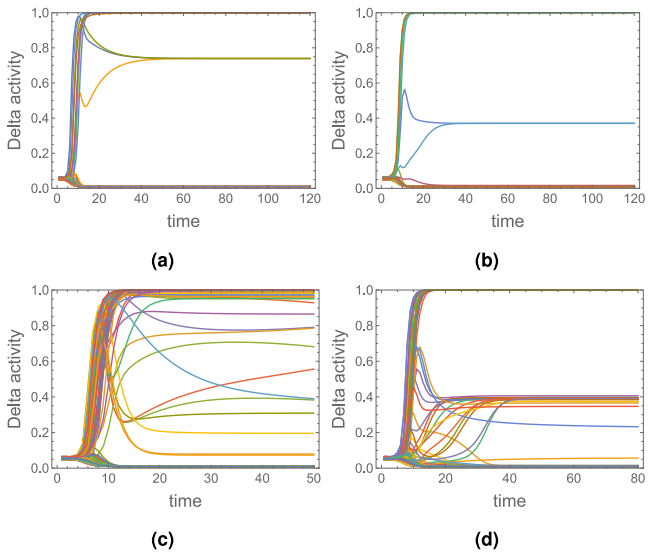

Fig. 4. Dynamics at critical ϵ values.
Delta activity dynamics on **(a–b)** 6×6 and **(c–d)** 14×14 periodic lattice, for **(a,c)** $\epsilon \simeq 0.09$, and **(b,d)** $\epsilon \simeq 0.78$. Patterns with multiple cell types emerge for critical values of ϵ.

$\epsilon < 0.55$. In particular, the peak around $\epsilon = 0.4$ is consistent with the dynamics predicted by LSA and $\max \mathrm{Re}(\lambda^{\pm}_{\vec{q},\vec{p}})$, in Fig. 2(c). Naturally, other refined patterning criteria are conceivable. Our argument is merely an illustration of the predictive power of LSA.

3.2. Multiple cell types

For a narrow range of ϵ values, alternative steady state solutions that include more than two cell types (based on Delta levels) are possible. This effect is observable at both ends of the ϵ spectrum, defining thresholds of pattern selection. To two decimal places, for $\epsilon \simeq 0.09$ and $\epsilon \simeq 0.78$, 6×6 periodic lattices yield approximately 3 different cell types (Figs. 4(a)–4(b)). For 14×14 lattices, we get a gradient of cell types (Figs. 4(c)–4(d)). Whether some of these solutions eventually converge to others, reducing the number of distinct cell types, is not known. The definition of a cell type is therefore ambiguous and, for larger timescales, processes such as proneural positive feedback or cell proliferation take over, rendering the subject of long-term pattern resolution purely academic. Nonetheless, we believe this effect to be noteworthy.

3.3. Long and oriented protrusions

A possible first extension is to consider the effects of longer or oriented protrusions. Examples of applications regarding this type of long-range signalling can be found in studies of the stripe and spot patterns observed in the skin of *zebrafish* and *pearl danio*, respectively [3,23,24].

In [18], a general weighting function was considered to account for protrusion length and orientation. Here, we adapt such a framework by focusing only on the protrusion weighting component ω_{p_g}, given by

$$\omega_{p_g}(\Delta j, \Delta m) = \begin{cases} \omega^* e^{-\sigma_1 (d_{s,r} - \hat{d})^2} e^{\sigma_2 \cos(\alpha(\theta_{s,r} - \hat{\theta}))} \\ \qquad \text{if } 1 < d_{s,r} \le p_\ell \\ \qquad \text{and } |\theta_{s,r}| \ge p_\theta, \\ 0 \qquad \text{otherwise,} \end{cases} \tag{33}$$

where $d_{s,r}$ and $\theta_{s,r} \in (-\pi, \pi]$ are defined as the relative distance and the angular bearing between the signalling and receiving cells, respectively. $\sigma_1, \sigma_2, \hat{d}, \hat{\theta}$ and α are parameters that control the shape and form of the weighting function, and ω^* is the normalising coefficient implicitly defined by Eq. (7). Furthermore, p_ℓ is the maximum protrusion length and p_θ is an angle bound.

We assume $d_{s,r}$ is the same for each cell in R_k, $k \ge 2$, and thus we may rewrite it, using our previous index notation, as a function of $(\Delta j, \Delta m)$

$$d_{s,r} \equiv d_{s,r}(\Delta j, \Delta m) = k, \text{ if } (\Delta j, \Delta m) \in S_k, \tag{34}$$

which yields $1 < k \le p_\ell$. Notice that Δm replaces Δk in Fig. 1(b) to avoid confusion with the index of S_k. Eq. (34) is equivalent to the hexagonal-Manhattan distance d_H defined in Remark 1.2 (SN1). Notice also that, with $p_\ell = 2$, $p_\theta = 0$, $\sigma_{1,2} = 0$ and $\omega^* = 1/12$, we recover the R_2 weighting function ω_P given by Eq. (28). We set, in this case, $\omega = (1-\epsilon)\omega_J + \epsilon\omega_{p_g}$.

We focus only on the case of longer protrusions and thus we impose radial symmetry by taking $\sigma_2 = 0$, $p_\theta = 0$ (cases with $\sigma_2 > 0$ lead to axial and polarised signalling systems, as discussed in [18]). Intuitively, σ_1 represents the strength of ligand density decay with distance. In the following, we assume long-range signalling strength to decrease as a function of $d_{s,r}$ and therefore take $\hat{d} = d_{s,r}(\Delta j, \Delta m)|_{(\Delta j, \Delta m) \in R_2} = 2$ and $\sigma_1 > 0$. Hence Eq. (33) simplifies to

$$\omega_{p_g}(\Delta j, \Delta m) = \begin{cases} \omega^* e^{-\sigma_1 (d_{s,r}(\Delta j, \Delta m) - 2)^2} \\ \qquad \text{if } 1 < d_{s,r} \le p_\ell, \\ 0 \qquad \text{otherwise,} \end{cases} \tag{35}$$

where, from Eq. (7),

$$\overline{\omega_{p_g}}(p_\ell, \sigma_1) \equiv \frac{1}{\omega^*} \tag{36}$$

$$= \sum_{(\Delta j, \Delta m) \in \bigcup_{k=2}^{p_\ell} S_k} e^{-\sigma_1 (d_{s,r}(\Delta j, \Delta m) - 2)^2} \tag{37}$$

$$= 6 \sum_{k=2}^{p_\ell} k e^{-\sigma_1 (k-2)^2}. \tag{38}$$

Under the assumption that protrusions may reach up to R_4 ($p_\ell = 4$), we have that, as an example, $\overline{\omega_{p_g}}(4, \sigma_1) = 12 + 18e^{-\sigma_1} + 24e^{-4\sigma_1}$. For different values of σ_1, Fig. 5(d) shows the minimal feedback strength required for patterning, derived from $\Omega_{\vec{q},\vec{p}}$. The case $\sigma_1 = 0$ yields equal R_k ($2 \le k \le 4$) weighting and thus $\omega^* = 1/|\bigcup_{k=2}^{p_\ell} R_k| = 1/54$, in this case (Figs. 5(a)–5(c)). As $\sigma_1 \to \infty$, $\omega^* \to 1/12$ and we recover the dynamics for R_2 protrusions (Fig. 5(e)). Figs. 6(a)–6(c) show simulations for different values of p_ℓ. Interestingly, the pattern wavelengths for $p_\ell = 4$ are not correctly predicted by LSA, as seen by comparing the minimisers of Fig. 5(c) with the simulation in Fig. 6(c). For this value of p_ℓ, the minimising modes remain unchanged for a wider range of ϵ.

Considering bounded protrusions significantly alters the coupling function and symmetry may be broken. Interesting pattern may arise in this case when $\epsilon = 1$, especially regarding the emergence of clustering effects or *zebrafish*-type patterns, as shown in Figs. 6(d)–6(e) and discussed in some of the work by Binshtok and Sprinzak [25], Kondo et al. [24], Moreira and Deutsch [26].

3.4. Stochastic protrusions

One way of generalising the weighting function ω is to consider some level of randomness in protrusion-cell signalling. Previous studies have suggested that pattern regularity and refinement can be greatly improved by considering dynamic lifespan-based protrusions [9]. Here, we extend such an approach to the ϵ-Collier model on the R_2 ring.

Depending on the protrusion type and level of biological detail, different stochastic models may be implemented. For example, in the case of the eukaryotic flagellum [27] and stereocilia [28], the length evolution can be studied using a master equation with length-dependent rates of protrusion attachment and detachment. For such systems, the length fluctuations can be mapped onto an Ornstein–Uhlenbeck process. In other work, the length dynamics of bacterial protrusions (*pili*) have

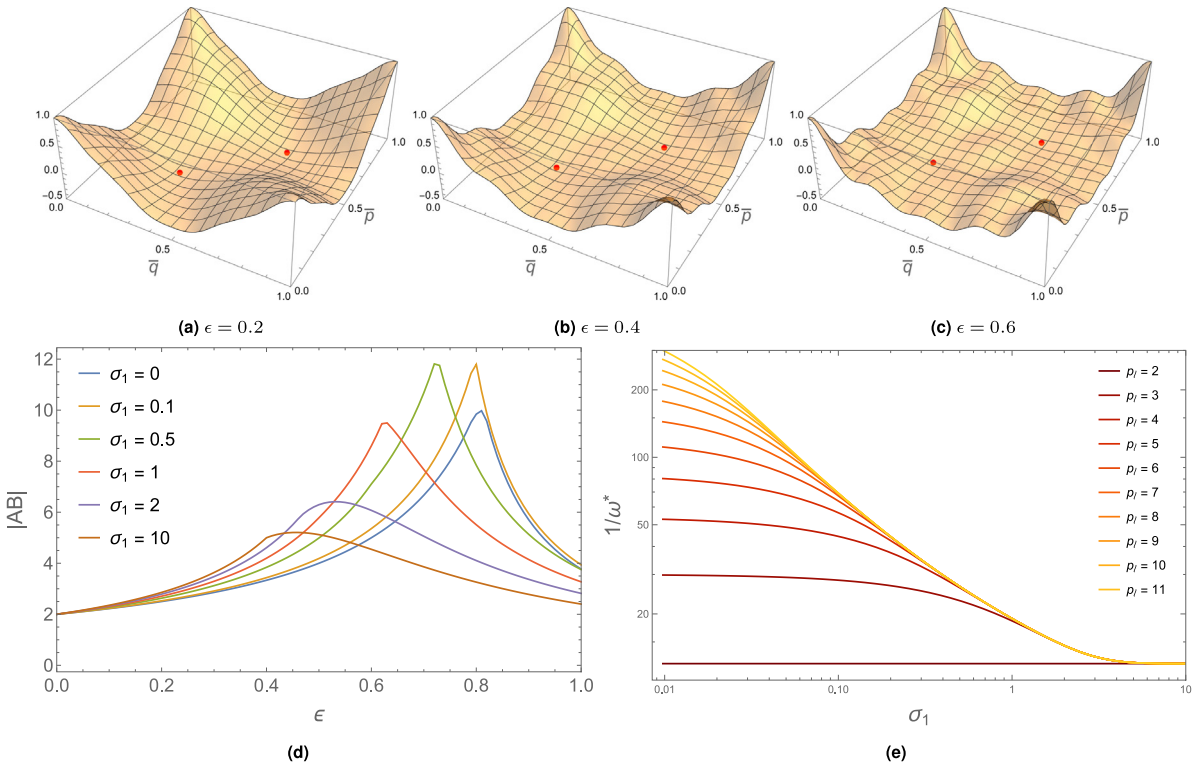

Fig. 5. Coupling dynamics of long protrusions as functions of ϵ.
(a–c) Plot of $\Omega_{\bar{q},\bar{p}}$ and respective minimising modes (in red) with $\sigma_1 = 0$. Wavier plots are observable due to the more complex nature of the weighting function, considering $p_\ell = 4$. **(d)** Critical $|AB|$ for different values of σ_1, given by $|1/\Omega_{\min}|$, with $p_\ell = 4$. **(e)** $1/\omega^*$ as a function of p_ℓ and σ_1. $\omega^* \to 1/12$ as $\sigma_1 \to \infty$. Parameters are shown in Table 1.

been described by a three-state Markov process [29]. Further details on the physics of filopodial protrusions can be found in [20,30] and an extensive discussion on length control of long cell protrusions of various types was presented in [31].

Here, however, we assume isotropic protrusions and consider dynamic binding and unbinding of filopodia to non-neighbouring cells throughout the simulation. The lifespan of protrusions is determined by birth and death rates, p_b and p_d, respectively. These correspond to the attachment and detachment rates of protrusions to non-neighbouring cells. Within a short time interval Δt, a link is formed between a cell and one of its second neighbours with probability $p_b \Delta t$. Such a link is destroyed with probability $p_d \Delta t$. This leads to the formulation of a continuous-time *telegraph process* [32–35] with rates p_b and p_d. This process is also known as a *dichotomic* or two-valued Markov process. In the following, we first present well-known results on telegraph processes, followed by the application to our case.

From stochastic theory, the general telegraph process is defined as a memoryless continuous-time stochastic process that has two distinct values. If the two possible values that a random variable $X(t)$ can take are x_1 and x_2, then the process can be described by the following master equations

$$\partial_t P(x_1, t|x, t_0) = -\gamma_1 P(x_1, t|x, t_0) + \gamma_2 P(x_2, t|x, t_0) \tag{39}$$

$$\partial_t P(x_2, t|x, t_0) = \gamma_1 P(x_1, t|x, t_0) - \gamma_2 P(x_2, t|x, t_0), \tag{40}$$

where γ_1 is the transition rate from state x_1 to state x_2 and γ_2 is the transition rate from state x_2 to state x_1. In this case, x_1 represents the state where a protrusion is absent and x_2 where it is present.

We are now interested in studying the asymptotic dynamics of the telegraph process, approximating its discrete realisations to a Bernoulli process, given a suitable condition on the realisation timescales. With $\Delta t \equiv t - t_0 \gg (\gamma_1 + \gamma_2)^{-1}$, the solution approaches a stationary distribution $\mathbf{P}_s$ given by

$$\mathbf{P}_s \equiv \lim_{\Delta t \gg (\gamma_1+\gamma_2)^{-1}} \mathbf{P}(t) = \frac{1}{\gamma_1 + \gamma_2} \begin{pmatrix} \gamma_2 \\ \gamma_1 \end{pmatrix}, \tag{41}$$

where $\mathbf{P} = \big(P(x_1, t|x, t_0), P(x_2, t|x, t_0)\big)^T$. The stationary average is then given by

$$\langle X \rangle_s = \frac{x_1 \gamma_2 + x_2 \gamma_1}{\gamma_1 + \gamma_2}. \tag{42}$$

In our case, we have $\gamma_1 = p_b$, $\gamma_2 = p_d$, $x_1 = 0$ and $x_2 = 1$. Hence, in the limit where $\Delta t \gg (p_b + p_d)^{-1}$, the probability of finding a protrusion is $p_b/(p_b + p_d)$. We may then treat such a process as a Bernoulli process with probability $p_b/(p_b + p_d)$. In other words, if the timescale at which we make the observation is longer than the inverse of the event rates, we may expect the process to be memoryless every time we observe, describing a Bernoulli process.

For each k in R_2 (cells reached by protrusions), we extend the ϵ-Collier model to account for these stochastic dynamics by defining the following random variables

$$\tilde{\epsilon}_k \overset{\text{iid}}{\sim} \text{Bern}\left(\frac{p_b}{p_b + p_d}\right). \tag{43}$$

We assume that neighbouring R_1 cells are always linked, with weight $(1-\epsilon)/6$, and R_2 cells are linked with stochastic weight $\epsilon\tilde{\epsilon}_k/12$. At each time step, the stochastic coupling term is then given by

$$\langle \tilde{d}_i \rangle(t) = \frac{1-\epsilon}{6} \sum_{j \in R_1} d_j(t) + \frac{\epsilon}{12} \sum_{k \in R_2} d_k(t) \tilde{\epsilon}_k, \tag{44}$$

where the second term is a sum of weighted i.i.d. Bernoulli distributions. Note that $\tilde{d}_i$ here should not be confused with the homogeneous state perturbation introduced in other sections. One of the key aspects of having dynamic protrusions is the possibility of pattern refinement over time. As suggested in [9], we define the coefficient of variation, ζ_V, of a pattern as the ratio between the standard deviation and mean of the distances from each SOP cell to its 6 closest SOP cells. This coefficient yields a measure of the global order of the emergent pattern, which we then track for different values of (p_b, p_d), as seen in Fig. 7(a). The case $(p_b, p_d) = (10, 3.5)$ is particularly interesting as the pattern converges to ideal cell packing ($\zeta_V = 0$) at around $t = 390$ (Fig. 7(e)).

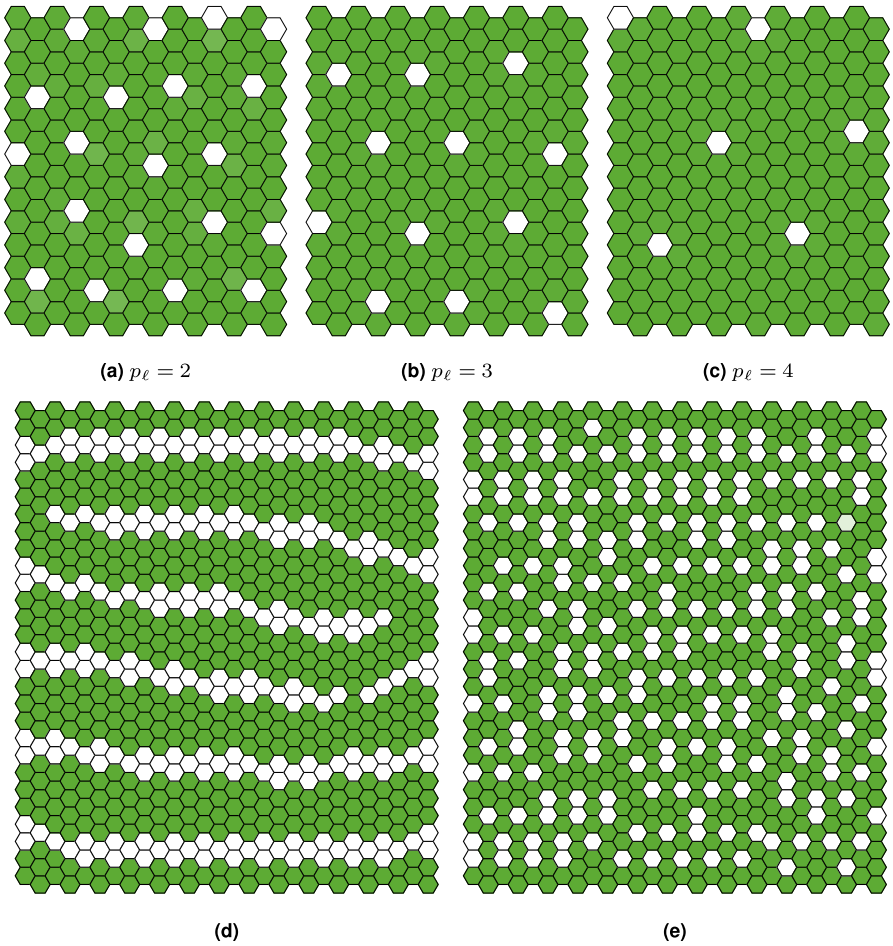

Fig. 6. Patterning with long and oriented protrusions.
(a–c) Simulations on a 14×14 lattice for different values of p_ℓ. Here, $\epsilon = 0.6$ and $h = k = 6$. **(d–e)** Bounded protrusions may lead to other patterns, relevant to other applications. Here, **(d)** $(\epsilon, p_\ell, p_\theta) = (1, 3, \pi/3)$, and **(e)** $(\epsilon, p_\ell, p_\theta) = (0.8, 2, \pi/4)$.

Some patterns only stabilise once optimal packing is attained, depending on the tissue dimensions. For a periodic tissue whose dimensions are multiples of 14, which guarantees optimal R_2-signal sparse patterning is possible (notice that 14×7 would also work), once the coefficient of variation is minimised, patterning does stabilise. In many cases, given enough time, the stable R_3 pattern is obtained after gradual refinement determined by p_b and p_d. In a perfectly refined pattern, one should expect $\zeta_V = 0$, which means each SOP cell is surrounded in R_3 by 6 other equally spaced SOP cells (Fig. 7(e), Video S3).

It should be noted that the simulations shown in Fig. 7 are all isolated examples corresponding to single realisations. Although the purpose of this study is to identify p_b and p_d such that pattern refinement is achieved, the complex relation between such rates to guarantee convergence to the refined pattern may be hinted at by a thorough stochastic analysis, which is beyond the scope of this work.

Remarkably, if we look at the extreme case of sudden removal of protrusions (from the refined state), we find that such a state is stable under purely juxtacrine lateral inhibition (Fig. 7(e)). This is similar to taking $\epsilon = 0$ after pattern stabilisation. Patterns of such wavelength contrast with the ones predicted by LSA, but they do not contradict pattern selection under consideration of nonlinear terms [19], as discussed below.

Considering different approaches to noise-driven protrusions might help in better understanding the role of stochastic effects in patterning and refinement. For instance, avoiding the Bernoulli approximation on the Markov-type protrusion dynamics could hint at a more realistic description of filopodium behaviour and consequently pattern formation. Noise-mediated filopodium reach and orientation have been studied in [9]. Cellular automaton models have also been used to explain sparse and more complex patterns [10]. Dichotomous noise has also been applied in Langevin dynamics, in a broader scenario [36].

A natural alternative to this source of noise, is to study the role of intrinsic noise, driven by Langevin dynamics [37,38]. In the case of morphogen-mediated patterning of gene expression, intrinsic noise has proven to affect timescale dynamics of bistable switches [39]. Stochastic effects were shown to accelerate juxtacrine pattern formation and alternative lateral inhibition models [40] were found to be robust to intrinsic noise [14]. Statistical properties of protein concentration in gene-regulated networks were more generally discussed in [41]. In the particular case of Notch-Delta and protrusions, a recent implementation of Gillespie's Stochastic Simulation Algorithm (SSA) [38] was discussed in [42], for a more convoluted signalling system, following the model by Hadjivasiliou et al. [11]. Here, the authors interpreted the relevant concentrations at each cell as absolute molecular counts at some fixed system volume.

3.5. Robustness and pattern selection

We now explore how Fourier analysis describes pattern selection under LSA. Again, we discuss robustness to changes in two of the main parameters in the ϵ-Collier model: the Hill function switch parameters, given by the trans-interactions strength $r_t = 1/a$ and the ligand inhibition strength b. We study the convergence to the desired pattern with long-range signalling for different values of a and b. Here, we consider

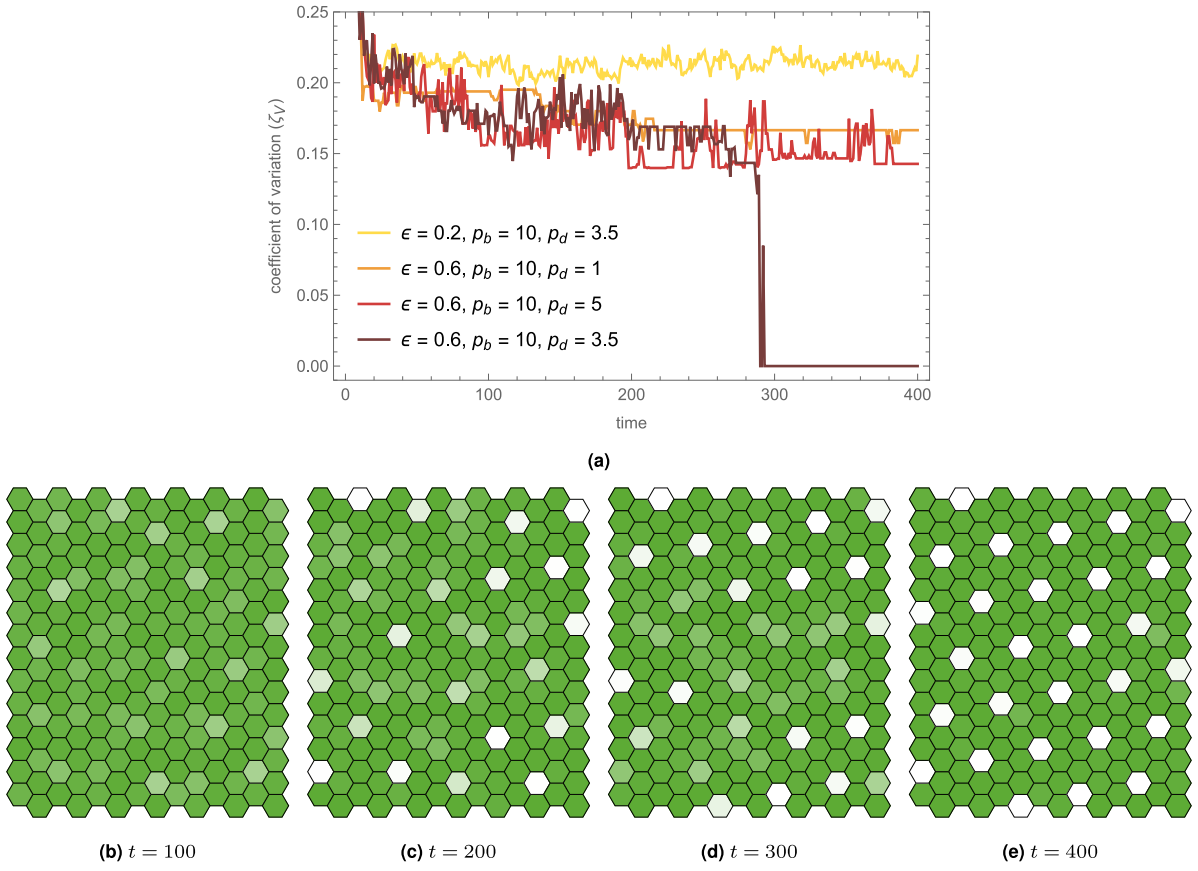

Fig. 7. Dynamics of stochastic protrusions.
(a) Stochastic behaviour of the coefficient of variation ζ_V in spacing between nearest Delta-expressing cells. **(b–e)** Pattern refinement may take a long time to stabilise. Once reaching the refined state at $t = 400$, the pattern hardly changes. The final pattern is also stable under no protrusions. Here, $\epsilon = 0.6$, $p_b = 10$ and $p_d = 3.5$. Other parameter values are shown in Table 1.

protrusions acting on the R_2 ring. In a system with two variables per cell like the linearised system

$$\frac{d}{dt}\tilde{n}_i = A\langle\tilde{d}_i\rangle - \tilde{n}_i \tag{45}$$

$$\frac{d}{dt}\tilde{d}_i = \nu B\tilde{n}_i - \nu\tilde{d}_i \tag{46}$$

the characteristic polynomial is of second order. As a consequence, each couple $(\bar{q},\bar{p})$ has two eigenvectors and eigenvalues. We then have that the solution of the linearised problem is given by

$$\begin{pmatrix}\tilde{n}_{j,k}(t)\\ \tilde{d}_{j,k}(t)\end{pmatrix} = \sum_{q=1}^{N}\sum_{p=1}^{M}\mathbf{A}(\bar{q},\bar{p})e^{2\pi\mathrm{i}(\bar{q}j+\bar{p}k)}, \tag{47}$$

where

$$\mathbf{A}(\bar{q},\bar{p}) \equiv C^{+}_{\bar{q},\bar{p}}e^{\lambda^{+}_{\bar{q},\bar{p}}t}\mathbf{v}^{+}_{\bar{q},\bar{p}} + C^{-}_{\bar{q},\bar{p}}e^{\lambda^{-}_{\bar{q},\bar{p}}t}\mathbf{v}^{-}_{\bar{q},\bar{p}}, \tag{48}$$

and where $\mathbf{v}^{\pm}_{\bar{q},\bar{p}}$ and $\lambda^{\pm}_{\bar{q},\bar{p}}$ are the eigenvectors and eigenvalues associated to $(\bar{q},\bar{p})$, respectively. $C^{+}_{\bar{q},\bar{p}}$ and $C^{-}_{\bar{q},\bar{p}}$ are constants depending on the initial conditions of the problem. In the case that at least one family of modes $(\bar{q},\bar{p})$ grows exponentially fast, it linearly destabilises the homogeneous solution and this family dominates over the rest, giving rise to a periodic pattern with the $(\bar{q},\bar{p})$-wavenumbers. At such critical modes, we have that the eigenvalue with the largest real part and respective eigenvector are given, as functions of ϵ, by

$$\lambda^{*}(\epsilon) = \frac{1}{2}\left(-(1+\nu) + \sqrt{(1+\nu)^2 - 4\nu(1-AB\Omega_{\min}(\epsilon))}\right) \tag{49}$$

$$\mathbf{v}^{*}(\epsilon) = \begin{pmatrix}\frac{1}{2}(\nu-1) + \sqrt{(1+\nu)^2 - 4\nu(1-AB\Omega_{\min}(\epsilon))}\\ \nu B\end{pmatrix}. \tag{50}$$

Hence, for large t, the dominant pattern is a superposition of modes with periodicity determined by $(\bar{q},\bar{p})$ and ϵ. Thus, for each family of critical modes $\mathcal{W}$, the solutions in Eq. (47) asymptotically satisfy

$$\begin{pmatrix}\tilde{n}_{j,k}\\ \tilde{d}_{j,k}\end{pmatrix} \simeq \mathbf{v}^{*}e^{\lambda^{*}t}\sum_{(\bar{q},\bar{p})\in\mathcal{W}} C^{+}_{\bar{q},\bar{p}}e^{2\pi\mathrm{i}(\bar{q}j+\bar{p}k)}, \tag{51}$$

where $\lambda^{*}, \mathbf{v}^{*}$ and $\mathcal{W}$ are all functions of ϵ. It is then clear that the long term behaviour of this solution is dependent on the amplitudes of the Fourier components in Eq. (51), which in turn depend on the initial conditions of the problem. In fact, since $\mathbf{v}^{*}e^{\lambda^{*}t}$ is independent of $(\bar{q},\bar{p})$ and $|e^{2\pi\mathrm{i}(\bar{q}j+\bar{p}k)}| = 1$, the relative amplitude is given by $C^{+}_{\bar{q},\bar{p}}$, which is implicitly determined by

$$C^{+}_{\bar{q},\bar{p}}\mathbf{v}^{+}_{\bar{q},\bar{p}} + C^{-}_{\bar{q},\bar{p}}\mathbf{v}^{-}_{\bar{q},\bar{p}} = \begin{pmatrix}\xi_{q,p}(0)\\ \eta_{q,p}(0)\end{pmatrix} \tag{52}$$

$$= \frac{1}{NM}\sum_{j=1}^{N}\sum_{k=1}^{M}\begin{pmatrix}\tilde{n}_{j,k}(0)\\ \tilde{d}_{j,k}(0)\end{pmatrix}e^{-2\pi\mathrm{i}(\bar{q}j+\bar{p}k)}. \tag{53}$$

Hence, depending on the choice of the initial conditions and consequently, $C^{+}_{\bar{q},\bar{p}}$, the long-term behaviour of the solution could yield different patterns and cell types. Similar to the analysis in [19], the generic pattern predicted by linear stability analysis might yield more than two cell types, depending on the choices of $C^{+}_{\bar{q},\bar{p}}$. Away from the bifurcation, cells usually opt for one of two possible fates, where, approximately, $(n,d) \in \{(0,1),(1,0)\}$. Therefore nonlinear effects are expected to play a role in determining the number of cell types. In particular, our model is robust because the final pattern of cell differentiation is not affected by the specific form of the Hill functions, as long as the feedback between cells is strong enough, similar to the lateral inhibition case ($\epsilon = 0$). Fig. 8 shows the pattern selection with corresponding fastest growing modes for different values of ϵ and $C^{+}_{\bar{q},\bar{p}} = 1$. From the vector in Eq. (51), we simply plot the real part of

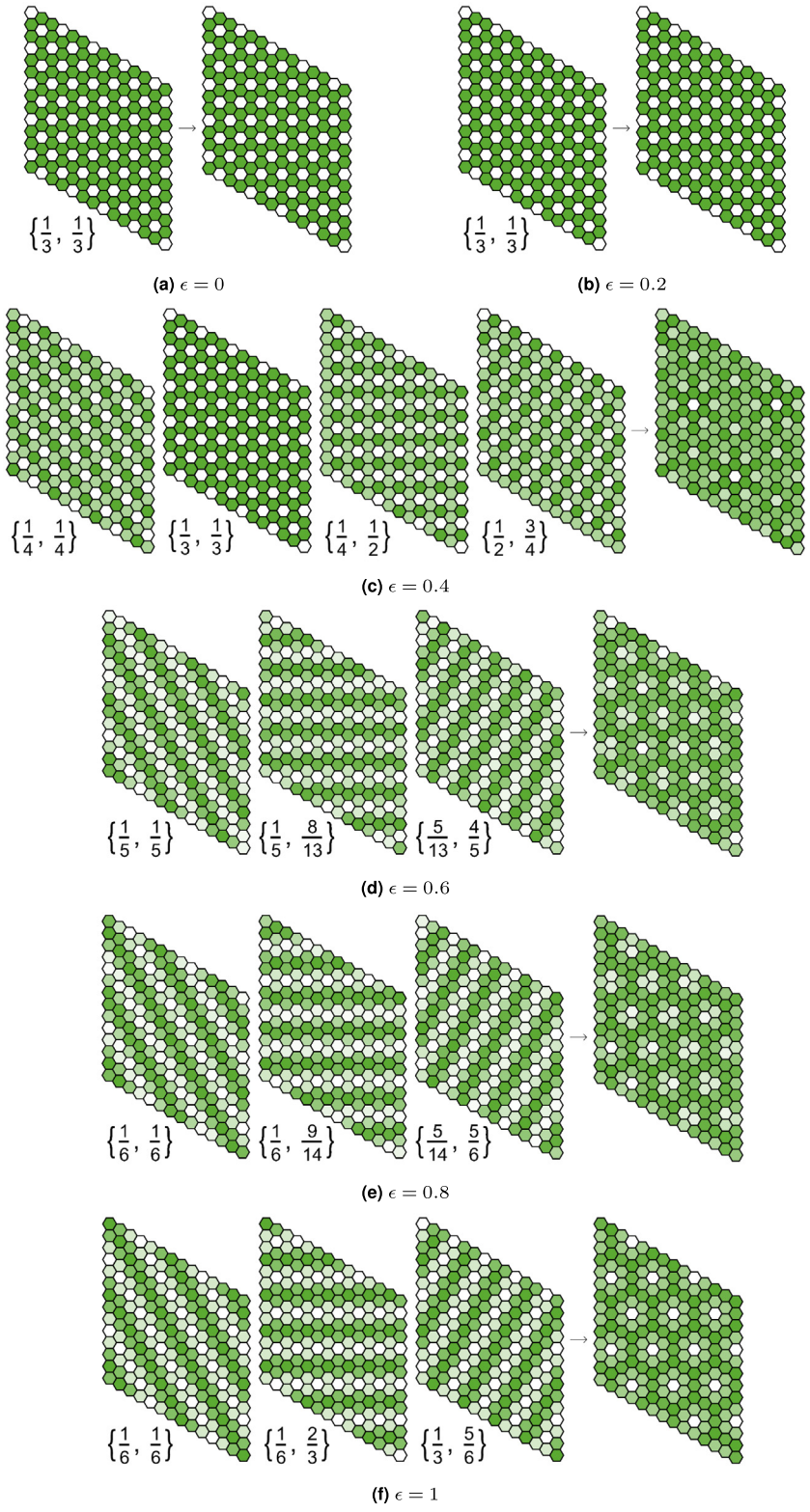

Fig. 8. Pattern selection via LSA: asymptotic solutions.
Eq. (51) decomposes the asymptotic solution to the linearised system in terms corresponding to different minimising modes $(\bar{q}, \bar{p})$. Each solution term is represented on the left of each of the subfigures **(a–f)**, for different values of ϵ, while their linearly combined solution is on the right. Due to symmetry, the pattern observed for each single mode $(\bar{q}, \bar{p})$ is the same for $(1-\bar{q}, 1-\bar{p})$ and thus we omit half of the single mode patterns. Here, $C^{+}_{\bar{q},\bar{p}} = 1 \ \forall(\bar{q}, \bar{p})$. The modes in **(d)** and **(e)** are rational approximations of the real values, as explained in the main text. Other parameter values are shown in Table 1.

the normalised sum values of its second term, corresponding to Delta activity (determining the opacity of each white cell). When necessary, and to illustrate the nature of the pattern, we provide rational approximations of the real values of the minimising $(\bar{q}, \bar{p})$-wavenumbers. While we do not expect, from LSA alone, to capture the main mechanisms required to explain longer wavelength patterns, pattern selection close to the bifurcations in Fig. 3 may be predicted and explained by such an analysis. For further results, a nonlinear approach is then required

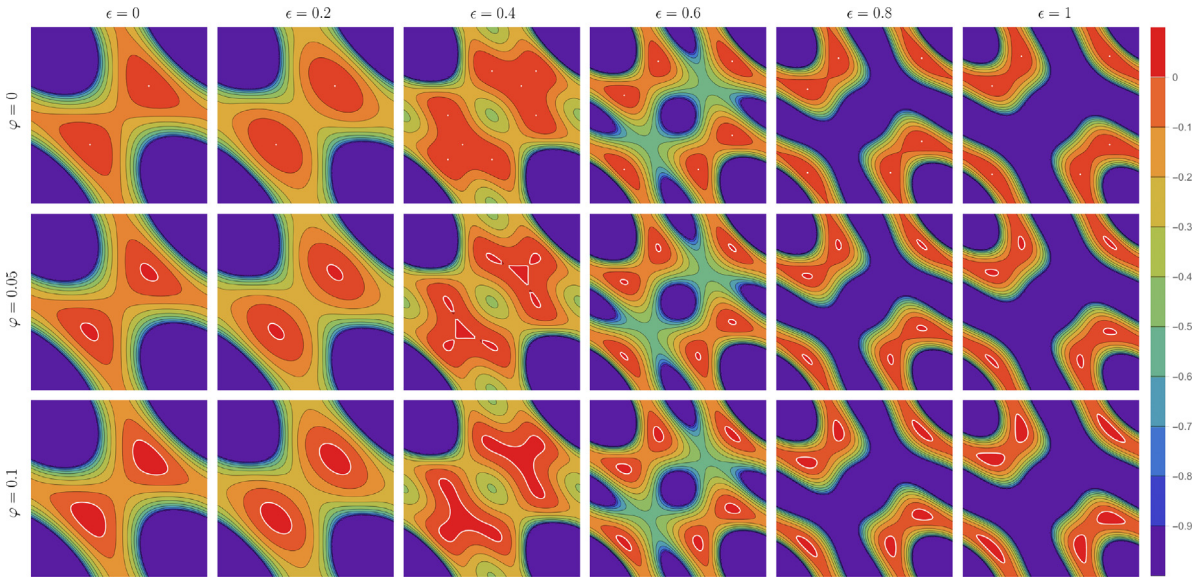

Fig. 9. Wavenumber level set bifurcation.
Contour plots of $\mathrm{Re}(\lambda^{+}_{\bar{q},\bar{p}})$ as a function of ϵ and φ, satisfying $AB - \varphi \leq 1/\Omega_{\min}(\epsilon)$. Here, we consider the critical feedback strength AB for each ϵ, so that, at $\varphi = 0$, $AB = 1/\Omega_{\min}(\epsilon)$. White contours are defined by $\mathrm{Re}(\lambda^{+}_{\bar{q},\bar{p}}) = 0$. For $\varphi = 0$, these correspond to the minimisers $\mathcal{W}$, As φ increases, initially disconnected and progressively larger wavenumber regions where $\mathrm{Re}(\lambda^{+}_{\bar{q},\bar{p}}) > 0$ emerge, corresponding to different level sets of the coupling function and determining instability robustness.

to extract some more information on the dynamics of such systems and pattern selection. We discuss both research avenues next.

3.5.1. Bifurcation analysis

In the context of studying long-range Notch-Delta signalling via protrusions in the ϵ-Collier model, both theoretical and numerical approaches can provide valuable insights into the system's behaviour near bifurcation points. While theoretical approaches such as centre manifold and normal form theory [43–46] can be useful, we focus on a numerical bifurcation analysis, which offers a more practical and computationally efficient way to study the system's dynamics [47,48]. By analysing the real part of the eigenvalues of the decoupled linearised system, we can gain insights into the bifurcation dynamics. In the case of Notch-Delta signalling, previous work has revealed intricate bifurcation dynamics in lateral inhibition models without protrusions, in a three-equation system [15,40,49]. These studies have revealed the presence of Hopf bifurcations, helping to understand the conditions that lead to oscillatory and stationary patterns in the signalling dynamics. In other work, also in a three-equation context, pitchfork bifurcations were shown to occur over critical values of Notch and Delta production rates, where antihexagon patterns emerged [50]. Bifurcations under long-range signalling were also studied by Chen et al. [51], to show that the neural pattern in *Ciona* may be explained and reproduced by a Notch-mediated gradient of long-range signalling. In our case, when $\nu = 1$, the eigenvalues of the decoupled linearised system are given by

$$\lambda^{\pm}_{\bar{q},\bar{p}} = -1 \pm \sqrt{\Omega_b}. \tag{54}$$

We can then study the bifurcation dynamics by varying the parameter $\Omega_b \equiv AB\Omega_{\bar{q},\bar{p}}$. The real part of the eigenvalues determines the stability of the fixed point and the nature of the bifurcation. As we vary Ω_b, we can observe the following bifurcation behaviour: When $\Omega_b < 1$, both eigenvalues have negative real parts, which indicates a stable fixed point. No bifurcation occurs in this region. When $\Omega_b = 1$, one of the eigenvalues has a real part equal to zero, marking a transition point where a bifurcation may occur. When $\Omega_b > 1$, one eigenvalue has a positive real part, and the other has a negative real part. This scenario corresponds to an unstable fixed point and indicates the presence of a saddle–node bifurcation.

While this holds in the frequency domain, stability around non-hyperbolic equilibria in the full nonlinear system is more complex. To better understand the dynamics around the bifurcation, we can plot the real part of the eigenvalues for varying neighbouring values of AB, with fixed critical $\Omega_{\bar{q},\bar{p}}$ (Fig. 9). This approach allows us to visualise the changes in the stability of the system as the bifurcation parameter AB varies, providing insights into the nature of the bifurcation and the behaviour of the system near the critical point. By analysing the real part of the eigenvalues for different values of AB, we can identify the transition point where a bifurcation occurs.

In the region near the bifurcation, we can virtually decrease the region of instability, approaching the bifurcation from an unstable region. In the context of pattern and wavenumber selection, this analysis is particularly useful, since it allows us to improve the predictive power of linear stability analysis, making it more likely that our numerical simulations will accurately capture the dynamics of the system near the critical point. In Fig. 10, we show numerical simulations of the ϵ-Collier model around multiple bifurcation points, where LSA is expected to predict pattern selection. In particular, we consider triples (r_t, b, ϵ) near the bifurcations defined in Fig. 3. We take $(r_t, b) \in \{(10, 10^2), (10^2, 10), (10^5, 10^{1.3})\}$.

In the vicinity of these parameter values, LSA effectively discerns the intrinsic dynamics governing pattern selection within the ϵ-Collier model. For instance, while small ϵ values appear to ensure sparse patterning away from these points, numerical simulations are consistent with wavelength selection via LSA for $\epsilon < 0.4$. Under these conditions, we anticipate short-ranged 3-period patterns to occur along the primary hexagonal axes, as illustrated in the first two columns of Fig. 10. As ϵ surpasses the bifurcation threshold ($\epsilon = 0.4$), the expression of directional clustering (stripes) and multiple cell types becomes increasingly dominant, owing to the diminishing strength of lateral inhibition in comparison to long-range signalling. This is also predicted by the linear analysis.

3.6. Multiscale methods

In addition to numerical bifurcation analysis, multiple scales methods can be used to further investigate the weakly nonlinear dynamics of the system [52–55]. These techniques involve the analysis of different timescales and spatial scales in the model, allowing for the identification of slow and fast dynamics and their interactions. Such an approach

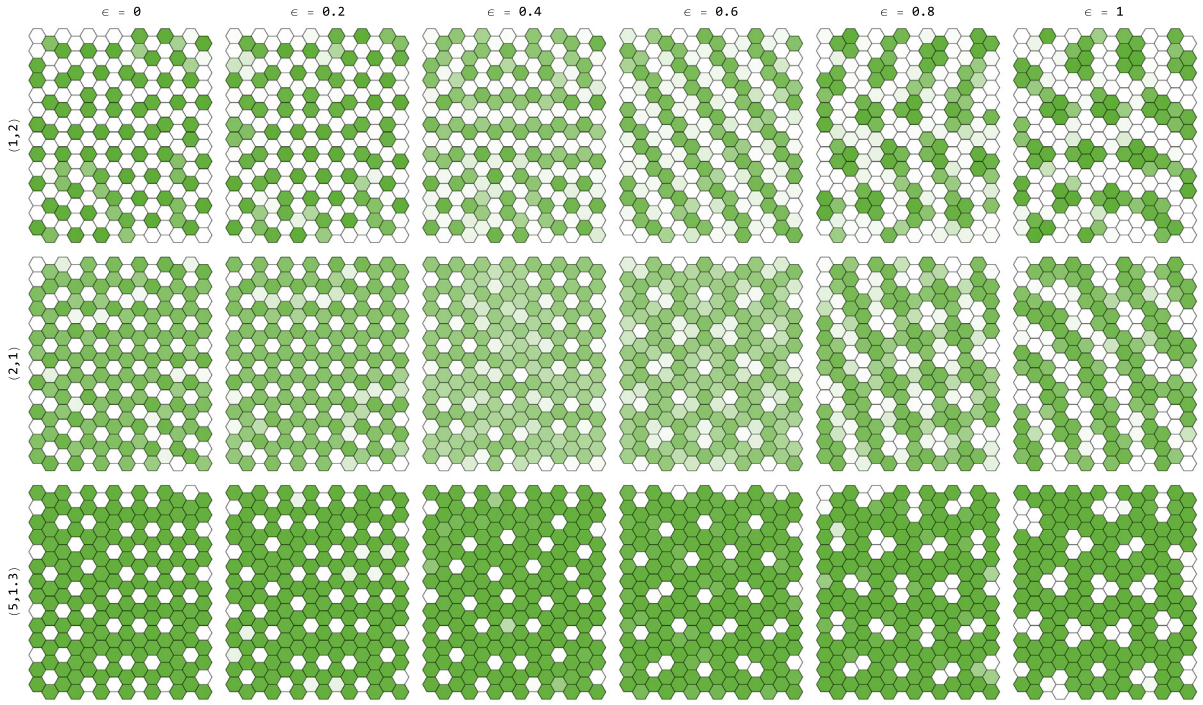

Fig. 10. Numerical simulations close to bifurcations.
Different patterns emerge around bifurcations. Here, we take $h = k = 6$ and consider three different parameter values near the bifurcations in Fig. 3, for varying ϵ: $(r_t, b) \in \{(10, 10^2), (10^2, 10), (10^5, 10^{1.3})\}$ ($log_{10} r_t, log_{10} b$ is shown on the y-axis). For $\epsilon < 0.4$, 3-period patterns are expected to emerge along the two main hexagonal axes, as predicted by LSA. In particular, around $(r_t, b) \simeq (10, 10^2)$, antihexagon patterns seem to emerge, as discussed in [50]. For intermediate values of ϵ ($0.4 < \epsilon < 0.6$), high trans-interactions strength (r_t) seems to ensure the robustness of sparser patterns, even close to a bifurcation, as seen at $(r_t, b) \simeq (10^5, 10^{1.3})$. Clustering of Delta-expressing cells becomes gradually more evident as ϵ increases, supported by the relatively large long-range signalling weighting, compared to lateral-inhibition. Multiple cell types are expected across a wide range of ϵ values, due to high-level branching of steady state solutions. r_t and b are correlated with φ via Eq. (21)–Eq. (22). Opacity levels are normalised at each simulation, and therefore white does not necessarily correspond to Delta activity equal to 1. The homogeneous steady states for each parameter pair are shown in Table 1.

can provide valuable insights into the complex behaviour of the long-range Notch-Delta signalling via protrusions, informing experimental studies and contributing to a better understanding of the signalling dynamics in biological systems. We discuss a brief application of such methods to our model, as well as their limitations.

Following Remark 1.1 in SN1, we aim to derive a continuum model upon the discrete model, so that we solve the decoupling issue with standard weakly nonlinear stability analysis (WNSA) on a translationally invariant system (see SN2). To do so, a homogenisation process must be employed. We follow the framework in [56,57]. For a hexagonal arrangement of cells, we denote the distance between cell centres by $\delta \ll 1$, introduce a slowly-varying continuum variable $\mathbf{x} = \delta i \mathbf{v}$, $\mathbf{v} \in \mathbb{R}^2$, and express the levels of Delta and Notch activity using the multiscale representation $n_i(t) = n(t, \mathbf{x})$ and $d_i(t) = d(t, \mathbf{x})$, where i represents the fast spatial variable and $\mathbf{x}$ represents the slow spatial variable. Second-order Taylor expanding in two variables leads to

$$d_{i+1}(t) \simeq d(t, \mathbf{x} + \delta \mathbf{v}) \tag{55}$$

$$\simeq d(t, \mathbf{x}) + \delta \nabla_{\mathbf{x}} d(t, \mathbf{x}) \cdot \mathbf{v} + \frac{\delta^2}{2} \mathbf{v}^T \mathbf{H}_d(\mathbf{x}) \mathbf{v}, \tag{56}$$

where $\nabla_{\mathbf{x}}$ and $\mathbf{H}_d$ are the (spatial) gradient and Hessian of d, respectively. We are interested in studying the dynamics of Delta across different directions. Without loss of generality, take the distance between any two adjacent cell centres to be 1. Hence, the relevant directions in our homogenisation correspond to the vectors between cell centres. Namely, with

$$\mathbf{U}_1 = \left\{ \left(\cos\left(\frac{k\pi}{3}\right), \sin\left(\frac{k\pi}{3}\right) \right) \right\}_{1 \le k \le 6} \tag{57}$$

$$\mathbf{U}_2 = \left\{ \left(\cos\left(\frac{k\pi}{3} + \frac{\pi}{6}\right), \sin\left(\frac{k\pi}{3} + \frac{\pi}{6}\right) \right) \right\}_{1 \le k \le 6}, \tag{58}$$

we define the following sets of vectors:

- First neighbour vectors (R_1): $\mathbf{V}_1 = \mathbf{U}_1$;
- Second neighbour vectors (R_2): $\mathbf{V}_2 = 2\mathbf{U}_1 \cup \sqrt{3}\mathbf{U}_2$.

Due to hexagonal symmetry, we have

$$\sum_{\mathbf{v} \in \mathbf{V}_1} d(t, \mathbf{x} + \delta \mathbf{v}) \simeq 6 d(t, \mathbf{x}) + \frac{3\delta^2}{2} \nabla_{\mathbf{x}}^2 d(t, \mathbf{x}) \tag{59}$$

$$\sum_{\mathbf{v} \in \mathbf{V}_2} d(t, \mathbf{x} + \delta \mathbf{v}) \simeq 12 d(t, \mathbf{x}) + \frac{21\delta^2}{2} \nabla_{\mathbf{x}}^2 d(t, \mathbf{x}), \tag{60}$$

where $\nabla_{\mathbf{x}}^2$ is the (spatial) Laplacian. Hence,

$$\langle d_i \rangle \simeq \frac{1-\epsilon}{6} \sum_{\mathbf{v} \in \mathbf{V}_1} d(t, \mathbf{x} + \delta \mathbf{v}) + \frac{\epsilon}{12} \sum_{\mathbf{v} \in \mathbf{V}_2} d(t, \mathbf{x} + \delta \mathbf{v}) \tag{61}$$

$$\simeq d(t, \mathbf{x}) + \delta(\epsilon) \nabla_{\mathbf{x}}^2 d(t, \mathbf{x}) + \mathcal{O}(\delta^4), \tag{62}$$

where $\delta(\epsilon) \equiv \delta^2(2 + 5\epsilon)/8$. The goal is now to study the equations at the timescale on which spatial coupling enters at $\mathcal{O}(\delta)$, which can be achieved with $\tau = \delta t$. Setting $A(t) \equiv \delta(\epsilon)$ in Eq. (S83) yields $b_m = 0$, $\forall m$ and so, in this case, Eq. (S131)–Eq. (S134) simplify to (see SN2 for full derivation details)

$$\mathbf{0} = \mathbf{J}(\mathbf{u}^*) \mathbf{v}_1 \tag{63}$$

$$\mathbf{0} = \mathbf{J}(\mathbf{u}^*) \mathbf{v}_2 + \frac{1}{2} \begin{pmatrix} \mathbf{v}_1^T \mathbf{H}_1(\mathbf{u}^*) \mathbf{v}_1 \\ \mathbf{v}_1^T \mathbf{H}_2(\mathbf{u}^*) \mathbf{v}_1 \end{pmatrix} \tag{64}$$

$$\mathbf{0} = \mathbf{J}(\mathbf{u}^*) \mathbf{v}_3 + \frac{1}{2} \begin{pmatrix} \mathbf{v}_2^T \mathbf{H}_1(\mathbf{u}^*) \mathbf{v}_1 \\ \mathbf{v}_2^T \mathbf{H}_2(\mathbf{u}^*) \mathbf{v}_1 \end{pmatrix} + \frac{1}{6} (D^3 \mathbf{F})_{\mathbf{u}^*} [(\mathbf{v}_1)^3], \tag{65}$$

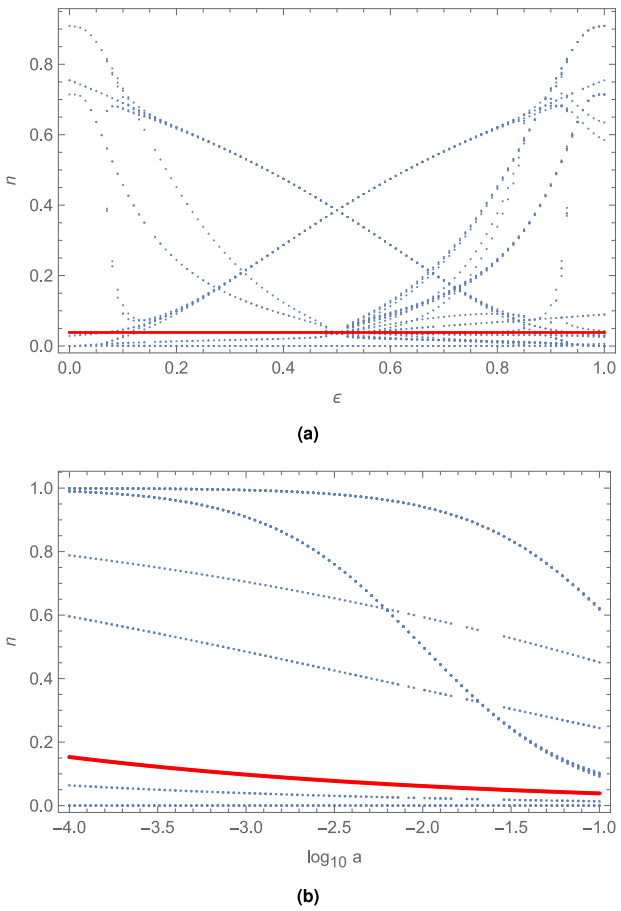

Fig. 11. Bifurcation diagrams in the ϵ-Collier model.
Bifurcation diagram for a 5-cell periodic system via the ϵ-Collier model. The homogeneous steady state n^* is shown in red for each case. **(a)** Steady states n for varying ϵ, with $h = k = 2$, $a = 10^{-1}$, and $b = 10^4$. $n^* \simeq 0.03848$, for all ϵ. At $\epsilon = 0.5$, first and second neighbours equally contribute to signalling. **(b)** Steady states n for varying a, with $\epsilon = 0.2$, $h = k = 2$, and $b = 10^4$.

where $\mathbf{u} \equiv (n, d)$. We are then looking for solutions of the form

$$\mathbf{u}(t) = \mathbf{u}^* + \mathbf{v}_1\delta(\epsilon) + \mathbf{v}_2\delta(\epsilon)^2 + \mathbf{v}_3\delta(\epsilon)^3 + O(\delta^4). \tag{66}$$

The case $\epsilon = 0$ was discussed in [57] for 3-period patterns along the main hexagonal axes. In this case, three distinct cell types were considered. For $\epsilon > 0$, however, there is a dramatic rise in mathematical complexity as a result of the variety of new patterning possibilities. In particular, it becomes challenging to track the perturbations around bifurcations, as these drastically increase in number. To illustrate the complexity induced by long-range signalling, we consider a simplified model along one of the main hexagonal axes. Considering a 5-cell system with periodic boundary conditions (so that R_2 is now a non-overlapping pair of second-neighbours), we plot the bifurcation diagrams under variation of ϵ and a (Fig. 11). Here, we do not distinguish between stable and unstable states, but multiple pitchfork bifurcations are expected from $AB < 1/\Omega_{\min}$. The case $h > 2$ is computationally more demanding to solve and does not invalidate the discussion here. The homogeneous steady states are shown in red. The various branches reveal the difficulty in performing multiscale analysis on our particular system. While 5-period patterns may be expected from linear analysis (Fig. 8(d)), applying multiscale methods to our wavelength selection is, in general, a challenging task, which adds to the contrast between lateral-inhibition models and a model of long-range signalling such as the ϵ-Collier model.

Overall, multiple scale analysis is a powerful technique for studying systems with distinct temporal or spatial scales. However, its application to systems with numerous bifurcations is debatable, due to the complexity of bifurcations, sensitivity to initial conditions, and parameter dependence, which is more pronounced in a model like ours. Bifurcations introduce intricate behaviours that blur the boundaries between scales, while the sensitivity to initial conditions and parameter dependence makes it difficult to determine appropriate scales for analysis. To overcome these limitations, future work could focus on designing adaptive multiscale techniques that dynamically adjust to evolving system dynamics, in general lattices and signalling networks [58,59].

In the supplementary information, and motivated by reaction–diffusion systems, we explore a possible application of WNSA to patterning derived from long-range signalling, and discuss its limitations in our system's coupling dynamics [17,60–62]. Compared to LSA, and as detailed in SN2, decoupling seems mathematically unfeasible in the case of translationally invariant Notch-Delta signalling systems, given the complexity generated by the higher-order terms. Any decoupling methodology as systematic as the linear case seems to be out of reach within our framework.

4. Discussion

In this work, we have outlined some of the main tools for analysing a general long-range signalling model. We developed such a model by taking a relative signalling approach. Long-range signalling via filopodia is weighted by a parameter ϵ, while the juxtacrine contribution is weighted by $1-\epsilon$. This constitutes the ϵ-Collier model, understood as a long-range extension of the original Collier model [19]. We found that sparser patterns on periodic hexagonal lattices are robust and tend to emerge for a wide range of ϵ values. To comprehend the linear effects of long-range signalling, we first employed a linear stability analysis for generally coupled and translationally invariant systems (SN1), followed by a direct application to the ϵ-Collier model. We explored various protrusion modelling frameworks, including short- and long-range protrusions, and stochastic protrusion dynamics. We discovered that patterning timing is highly dependent on ϵ, as supported by our stability analysis.

Overall, LSA proved to be a useful tool for identifying the fastest-growing modes under Fourier analysis, and, in addition to solely juxtacrine models, LSA was able to predict short and sparse patterning across a broad range of ϵ values. In particular, we examined parameters closer to the bifurcation point at which the homogeneous state becomes linearly unstable (dashed lines in Fig. 3). Here, it was anticipated that the model behaves more linearly; hence, LSA may match the simulation outcomes better, which we confirmed with numerical simulations for specific critical bifurcation neighbourhoods. If this does not occur, it may indicate we are near a subcritical bifurcation (as opposed to a supercritical one), and when a subcritical bifurcation occurs, LSA does not necessarily predict the patterning outcome [63,64]. Away from critical points, nonlinear effects play a significant role in sparse pattern selection and alternative methods were discussed, including multiple scales methods and weakly nonlinear stability analysis inspired by reaction–diffusion literature.

Multiple scales methods have proven to be indispensable tools for investigating Notch-Delta signalling, as they facilitate the analysis of the complex interplay between molecular interactions and cellular behaviour across spatial and temporal scales [56,57]. These methods elucidate the intricate dynamics of signalling networks, which can become mathematically intractable as the network expands, and demonstrated by the increasing number of steady-state bifurcations in the case of the ϵ-Collier model. Furthermore, these methods often involve bridging the gap between discrete and continuum descriptions of cellular processes, taking into account stochastic fluctuations, reaction–diffusion kinetics, and the spatial organisation of signalling components. The continuum approach requires a thorough rethinking of the ϵ parameter, which determines the relative signalling strength between lateral inhibition and protrusion-based signalling.

Motivated by the multiscale approach, we devised a framework for weakly nonlinear stability analysis in order to achieve expanded

qualitative conclusions on wavelength selection in Fourier-transformed coupling functions. Specifically, we presented the main methodology behind a potential framework for WNSA of translationally invariant Notch-Delta systems. We expanded well-known reaction–diffusion techniques to coupled spatially discrete systems, such as the ϵ-Collier model on a periodic hexagonal lattice, by considering harmonic-based Landau-type solutions. We found that the decoupling mechanism in translationally invariant systems appears impractical in WNSA.

Ultimately, this work outlines a framework for understanding pattern formation in relatively general long-range signalling systems, highlighting some of the primary mathematical challenges in such a theory and indicating possible generalisations and future research avenues, in the context of both linear and weakly nonlinear methodologies. Furthermore, the single-parameter adaptability of the ϵ-Collier model encompasses a whole family of long-range signalling phenomena, which can be adjusted for a variety of modelling approaches. Our findings have significant implications for understanding the behaviour of natural systems, such as the SOP patterning in the fly notum and the skin patterns of different *danio* species, where sparse patterns are observed. In particular, the ϵ-Collier model will be adapted in a subsequent publication to study the emergence of sensory organ precursors on the wing pouch of *Drosophila melanogaster* during the late third instar, which is a crucial aspect of wing development.

The fact that such patterns arise for a broad range of ϵ values suggests that the interplay between long-range signalling and juxtacrine contribution plays a key role in cell fate commitment. Understanding its underlying dynamics could be useful for developing new strategies to monitor or control patterning in biological systems, such as tissue engineering or regenerative medicine.

5. Computational methods

5.1. Simulations

All simulations were performed using *Interactive Epithelium* (IEp), a *Wolfram Mathematica* tool for hybrid Notch-Delta epithelial signalling and patterning simulations. IEp aims to provide a practical tool for testing parameter robustness while simulating the dynamics of the Notch-Delta signalling pathway in an epithelium. Table 1 in Supplementary Note 3 contains the precise parameter values for the simulation plots shown in this work.

5.2. Code availability

The source code and data that were used to develop the main conclusions and analyses presented in this work are available on the following repository hosted on GitHub: https://github.com/fberkemeier/Notch-Delta-Coupling.git. The relevant video simulations can also be found in this repository. Previous versions are available upon request. For any comments/suggestions, as well as copyright issues, please contact fp409@cam.ac.uk.

Declaration of competing interest

The authors declare that they have no known competing financial interests or personal relationships that could have appeared to influence the work reported in this paper.

Data availability

No external data is required. See *Code availability* for further details.

Acknowledgments

We would like to thank Drs. M. Dalwadi, P. Pearce, R. Pérez-Carrasco, and G. Paci, and Profs. Y. Mao, B. Baum and N. Monk for their helpful discussions and comments that greatly improved the manuscript. This research was made possible by a UCL Studentship Award from the Department of Mathematics and the Leverhulme Trust Research Project Grant RPG-2022-028.

Appendix A. Supplementary data

Supplementary material related to this article can be found online at https://doi.org/10.1016/j.mbs.2023.109012.

References

[1] S.M. Cohen, Long-range signalling by touch, Nature 426 (6966) (2003) 503–504.
[2] C. De Joussineau, J. Soule, M. Martin, C. Anguille, P. Montcourrier, D. Alexandre, Delta-promoted filopodia mediate long-range lateral inhibition in drosophila, Nature 426 (6966) (2003) 555–559.
[3] H. Hamada, M. Watanabe, H.E. Lau, T. Nishida, T. Hasegawa, D.M. Parichy, S. Kondo, Involvement of delta/notch signaling in zebrafish adult pigment stripe patterning, Development 141 (2) (2014) 318–324.
[4] G.L. Hunter, L. He, N. Perrimon, G. Charras, E. Giniger, B. Baum, A role for actomyosin contractility in notch signaling, BMC Biol. 17 (1) (2019) 1–15.
[5] F.-A. Ramírez-Weber, T.B. Kornberg, Cytonemes: cellular processes that project to the principal signaling center in drosophila imaginal discs, Cell 97 (5) (1999) 599–607.
[6] A.-C. Gradilla, I. Guerrero, Cytoneme-mediated cell-to-cell signaling during development, Cell Tissue Res. 352 (1) (2013) 59–66.
[7] T.B. Kornberg, S. Roy, Cytonemes as specialized signaling filopodia, Development 141 (4) (2014) 729–736.
[8] N.M. Sherer, W. Mothes, Cytonemes and tunneling nanotubules in cell–cell communication and viral pathogenesis, Trends Cell Biol. 18 (9) (2008) 414–420.
[9] M. Cohen, M. Georgiou, N.L. Stevenson, M. Miodownik, B. Baum, Dynamic filopodia transmit intermittent delta-notch signaling to drive pattern refinement during lateral inhibition, Dev. Cell 19 (1) (2010) 78–89.
[10] M. Cohen, B. Baum, M. Miodownik, The importance of structured noise in the generation of self-organizing tissue patterns through contact-mediated cell–cell signalling, J. R. Soc. Interface 8 (59) (2010) 787–798.
[11] Z. Hadjivasiliou, G.L. Hunter, B. Baum, A new mechanism for spatial pattern formation via lateral and protrusion-mediated lateral signalling, J. R. Soc. Interface 13 (124) (2016) 20160484.
[12] Z. Hadjivasiliou, R.E. Moore, R. McIntosh, G.L. Galea, J.D. Clarke, P. Alexandre, Basal protrusions mediate spatiotemporal patterns of spinal neuron differentiation, Dev. Cell 49 (6) (2019) 907–919.
[13] D.T. Gillespie, The chemical langevin equation, J. Chem. Phys. 113 (1) (2000) 297–306.
[14] T. Rudge, K. Burrage, Effects of intrinsic and extrinsic noise can accelerate juxtacrine pattern formation, Bull. Math. Biol. 70 (4) (2008) 971–991.
[15] S.D. Webb, M.R. Owen, Oscillations and patterns in spatially discrete models for developmental intercellular signalling, J. Math. Biol. 48 (4) (2004) 444–476.
[16] B. Zakirov, G. Charalambous, R. Thuret, I.M. Aspalter, K. Van-Vuuren, T. Mead, K. Harrington, E.R. Regan, S.P. Herbert, K. Bentley, Active perception during angiogenesis: filopodia speed up notch selection of tip cells in silico and in vivo, Phil. Trans. R. Soc. B 376 (1821) (2021) 20190753.
[17] A. Turing, The chemical basis of morphogenesis, Phil. Trans. R. Soc. B 237 (641) (1952) 37–72.
[18] G. Vasilopoulos, K.J. Painter, Pattern formation in discrete cell tissues under long range filopodia-based direct cell to cell contact, Math. Biosci. 273 (2016) 1–15.
[19] J.R. Collier, N.A. Monk, P.K. Maini, J.H. Lewis, Pattern formation by lateral inhibition with feedback: a mathematical model of delta-notch intercellular signalling, J. Theoret. Biol. 183 (4) (1996) 429–446.
[20] A. Mogilner, B. Rubinstein, The physics of filopodial protrusion, Biophys. J. 89 (2) (2005) 782–795.
[21] P. Formosa-Jordan, M. Ibañes, Diffusible ligand and lateral inhibition dynamics for pattern formation, J. Stat. Mech. Theory Exp. 2009 (03) (2009) P03019.
[22] J. Murray, Mathematical Biology II: Spatial Models and Biomedical Applications, Springer New York, 2001.
[23] D.S. Eom, E.J. Bain, L.B. Patterson, M.E. Grout, D.M. Parichy, Long-distance communication by specialized cellular projections during pigment pattern development and evolution, Elife 4 (2015) e12401.
[24] S. Kondo, M. Watanabe, S. Miyazawa, Studies of turing pattern formation in zebrafish skin, Phil. Trans. R. Soc. A 379 (2213) (2021) 20200274.
[25] U. Binshtok, D. Sprinzak, Modeling the notch response, in: Molecular Mechanisms of Notch Signaling, Springer, 2018, pp. 79–98.

[26] J. Moreira, A. Deutsch, Pigment pattern formation in zebrafish during late larval stages: A model based on local interactions, Dev. Dyn. Off Pub. Am. Assoc. Anatom. 232 (1) (2005) 33–42.
[27] W.F. Marshall, J.L. Rosenbaum, Intraflagellar transport balances continuous turnover of outer doublet microtubules: implications for flagellar length control, J. Cell Biol. 155 (3) (2001) 405–414.
[28] P. Narayanan, P. Chatterton, A. Ikeda, S. Ikeda, D.P. Corey, J.M. Ervasti, B.J. Perrin, Length regulation of mechanosensitive stereocilia depends on very slow actin dynamics and filament-severing proteins, Nature Commun. 6 (1) (2015) 1–8.
[29] M.D. Koch, C. Fei, N.S. Wingreen, J.W. Shaevitz, Z. Gitai, Competitive binding of independent extension and retraction motors explains the quantitative dynamics of type IV pili, Proc. Natl. Acad. Sci. 118 (8) (2021) e2014926118.
[30] S. Patra, D. Chowdhury, Length fluctuations of long cell protrusions: statistics of passage times, random and extremal excursions, 2020, arXiv preprint arXiv: 2008.09851.
[31] S. Patra, D. Chowdhury, F. Jülicher, Length control of long cell protrusions: rulers, timers and transport, Phys. Rep. 987 (2022) 1–51.
[32] M. Kac, A stochastic model related to the telegrapher's equation, Rocky Mountain J. Math. 4 (3) (1974) 497–509.
[33] I. Bena, C. Van den Broeck, R. Kawai, K. Lindenberg, Nonlinear response with dichotomous noise, Phys. Rev. E 66 (4) (2002) 045603.
[34] A.D. Kolesnik, N. Ratanov, Telegraph Processes and Option Pricing, Vol. 204, Springer, 2013.
[35] O. López, N. Ratanov, On the asymmetric telegraph processes, J. Appl. Probab. 51 (2) (2014) 569–589.
[36] D. Barik, P.K. Ghosh, D.S. Ray, Langevin dynamics with dichotomous noise; direct simulation and applications, J. Stat. Mech. Theory Exp. 2006 (03) (2006) P03010.
[37] D.T. Gillespie, A general method for numerically simulating the stochastic time evolution of coupled chemical reactions, J. Comput. Phys. 22 (4) (1976) 403–434.
[38] D.T. Gillespie, Exact stochastic simulation of coupled chemical reactions, J. Phys. Chem. 81 (25) (1977) 2340–2361.
[39] R. Perez-Carrasco, P. Guerrero, J. Briscoe, K.M. Page, Intrinsic noise profoundly alters the dynamics and steady state of morphogen-controlled bistable genetic switches, PLoS Comput. Biol. 12 (10) (2016) e1005154.
[40] H.J. Wearing, M.R. Owen, J.A. Sherratt, Mathematical modelling of juxtacrine patterning, Bull. Math. Biol. 62 (2) (2000) 293–320.
[41] M. Thattai, A. Van Oudenaarden, Intrinsic noise in gene regulatory networks, Proc. Natl. Acad. Sci. 98 (15) (2001) 8614–8619.
[42] S. Engblom, Stochastic simulation of pattern formation in growing tissue: a multilevel approach, Bull. Math. Biol. 81 (8) (2019) 3010–3023.
[43] S. Wiggins, S. Wiggins, M. Golubitsky, Introduction To Applied Nonlinear Dynamical Systems and Chaos, Vol. 2, (3) Springer, 2003.
[44] Y.A. Kuznetsov, I.A. Kuznetsov, Y. Kuznetsov, Elements of Applied Bifurcation Theory, vol. 112, Springer, 1998.
[45] M. Markakis, P. Douris, An efficient center manifold technique for hopf bifurcation of n-dimensional multi-parameter systems, Appl. Math. Model. 50 (2017) 300–313.
[46] D. Sattinger, Group representation theory, bifurcation theory and pattern formation, J. Funct. Anal. 28 (1) (1978) 58–101.
[47] H.G. Meijer, F. Dercole, B.E. Oldeman, et al., Numerical bifurcation analysis., 2009.
[48] W. Marszalek, H. Podhaisky, J. Sadecki, Computing two-parameter bifurcation diagrams for oscillating circuits and systems, IEEE Access 7 (2019) 115829–115835.
[49] M.R. Owen, J.A. Sherratt, Mathematical modelling of juxtacrine cell signalling, Math. Biosci. 153 (2) (1998) 125–150.
[50] E. Teomy, D.A. Kessler, H. Levine, Ordered hexagonal patterns via notch–delta signaling, Phys. Biol. 18 (6) (2021) 066006.
[51] J.S. Chen, A.M. Gumbayan, R.W. Zeller, J.M. Mahaffy, An expanded notch-delta model exhibiting long-range patterning and incorporating microrna regulation, PLoS Comput. Biol. 10 (6) (2014) e1003655.
[52] K. Fujimura, Methods of centre manifold and multiple scales in the theory of weakly nonlinear stability for fluid motions, Proc. R. Soc. Lond. Ser. A Math. Phys. Eng. Sci. 434 (1892) (1991) 719–733.
[53] N.E. Sanchez, The method of multiple scales: asymptotic solutions and normal forms for nonlinear oscillatory problems, J. Symbolic Comput. 21 (2) (1996) 245–252.
[54] A.H. Nayfeh, Perturbation Methods, John Wiley & Sons, 2008.
[55] A. Luongo, On the use of the multiple scale method in solving 'difficult'bifurcation problems, Math. Mech. Solids 22 (5) (2017) 988–1004.
[56] R.D. O'Dea, J.R. King, Multiscale analysis of pattern formation via intercellular signalling, Math. Biosci. 231 (2) (2011) 172–185.
[57] R.D. O'Dea, J.R. King, Continuum limits of pattern formation in hexagonal-cell monolayers, J. Math. Biol. 64 (2012) 579–610.
[58] E. Plahte, Pattern formation in discrete cell lattices, J. Math. Biol. 43 (5) (2001) 411–445.
[59] E. Plahte, L. Øyehaug, Pattern-generating travelling waves in a discrete multicellular system with lateral inhibition, Physica D 226 (2) (2007) 117–128.
[60] J. Stuart, On the non-linear mechanics of wave disturbances in stable and unstable parallel flows part 1. The basic behaviour in plane poiseuille flow, J. Fluid Mech. 9 (3) (1960) 353–370.
[61] J. Watson, On the non-linear mechanics of wave disturbances in stable and unstable parallel flows part 2. The development of a solution for plane poiseuille flow and for plane couette flow, J. Fluid Mech. 9 (3) (1960) 371–389.
[62] D.J. Wollkind, V.S. Manoranjan, L. Zhang, Weakly nonlinear stability analyses of prototype reaction-diffusion model equations, Siam Rev. 36 (2) (1994) 176–214.
[63] J.D. Crawford, Introduction to bifurcation theory, Rev. Modern Phys. 63 (4) (1991) 991.
[64] I. Stefanou, S. Alevizos, Fundamentals of bifurcation theory and stability analysis, Instabilities Modeling in Geomechanics (2016) 31–71.

Supplementary Information

Supplementary Note 1: Linear stability analysis

This section provides an introductory and fairly general approach to linear stability analysis (LSA). First, we discuss the main methods used in LSA and present some examples and applications, leading to the main study case: the Notch-Delta signalling pathway, in the main text. Many of the methodologies outlined here can be found in a variety of textbooks and should be familiar to most readers, but we opt for a self-contained approach to better shape the narrative towards the particular analysis of Notch-Delta signalling systems.

One-dimensional array

We start by looking at the one-dimensional periodic array consisting of N cells with two species x and y, in which concentrations in cell j are governed by

$$\dot{x}_j = F_x(x_j, \{x_r\}, y_j, \{y_r\}) \tag{S1}$$
$$\dot{y}_j = F_y(x_j, \{x_r\}, y_j, \{y_r\}), \tag{S2}$$

where F_x and F_y are general nonlinear functions. Here, $\{x_r\}$ and $\{y_r\}$ are the sets of all the variables corresponding to cells that are not cell j. That is, $r \neq j$. We use j as the focal cell index instead of i to avoid confusion with the imaginary number i, though indexation with i is interchangeably used in the following sections and main text. Eq. (S1)-Eq. (S2) is translationally invariant, implying that the system written in matrix form, for all cells, contains a banded circulant matrix. Note that we have a total of $2N$ equations. A homogeneous steady state of the system, (x^*, y^*), requires $\dot{x}_j = \dot{y}_j = 0$ when $(x_j, y_j) = (x^*, y^*)$, for any cell j. This results in the homogeneous system

$$0 = F_x(x^*, \{x^*\}, y^*, \{y^*\}) \tag{S3}$$
$$0 = F_y(x^*, \{x^*\}, y^*, \{y^*\}). \tag{S4}$$

Next, we perturb this solution by setting $(x_j, y_j) = (x^* + \tilde{x}_j, y^* + \tilde{y}_j)$ and, following linearisation, we get

$$\frac{d}{dt}\begin{pmatrix}\tilde{x}_j \\ \tilde{y}_j\end{pmatrix} \simeq \mathbf{J}\begin{pmatrix}\tilde{x}_j \\ \tilde{y}_j\end{pmatrix} + \sum_{r\neq j}\mathbf{J}^r\begin{pmatrix}\tilde{x}_r \\ \tilde{y}_r\end{pmatrix}, \tag{S5}$$

where

$$\mathbf{J} = \left.\begin{pmatrix}\frac{\partial F_x}{\partial x_j} & \frac{\partial F_x}{\partial y_j} \\ \frac{\partial F_y}{\partial x_j} & \frac{\partial F_y}{\partial y_j}\end{pmatrix}\right|_{(x^*,y^*)} \text{and } \mathbf{J}^r = \left.\begin{pmatrix}\frac{\partial F_x}{\partial x_r} & \frac{\partial F_x}{\partial y_r} \\ \frac{\partial F_y}{\partial x_r} & \frac{\partial F_y}{\partial y_r}\end{pmatrix}\right|_{(x^*,y^*)}. \tag{S6}$$

Expanding the previous expressions, we rewrite the linearised system as

$$\frac{d}{dt}\begin{pmatrix}\tilde{x}_j \\ \tilde{y}_j\end{pmatrix} = \begin{pmatrix}\mathbf{J}_{11}\tilde{x}_j + \mathbf{J}_{12}\tilde{y}_j + \sum_{r\neq j}\left[\mathbf{J}^r_{11}\tilde{x}_r + \mathbf{J}^r_{12}\tilde{y}_r\right] \\ \mathbf{J}_{21}\tilde{x}_j + \mathbf{J}_{22}\tilde{y}_j + \sum_{r\neq j}\left[\mathbf{J}^r_{21}\tilde{x}_r + \mathbf{J}^r_{22}\tilde{y}_r\right]\end{pmatrix}. \tag{S7}$$

Next, we decouple the system of $2N$ equations by performing a discrete Fourier transform with respect to j and changing the variables as follows, for $1 \leq q \leq N$,

$$\tilde{x}_j = \sum_{q=1}^{N}\xi_q e^{2\pi \mathrm{i} qj/N} \tag{S8}$$
$$\tilde{y}_j = \sum_{q=1}^{N}\eta_q e^{2\pi \mathrm{i} qj/N}, \tag{S9}$$

which may also be written as

$$\xi_q = \frac{1}{N}\sum_{j=1}^{N}\tilde{x}_j e^{-2\pi \mathrm{i} qj/N} \tag{S10}$$
$$\eta_q = \frac{1}{N}\sum_{j=1}^{N}\tilde{y}_j e^{-2\pi \mathrm{i} qj/N}. \tag{S11}$$

Eq. (S8) and Eq. (S9) are Fourier transforms in the *exponential form* (Bracewell and Bracewell, 1986). In order to rewrite the system for (ξ_q, η_q), start by differentiating ξ_q and substituting in Eq. (S7), as follows, with $\bar{q} \equiv q/N$,

$$\frac{d\xi_q}{dt} = \frac{1}{N}\sum_{j=1}^{N} \frac{d\tilde{x}_j}{dt} e^{-2\pi \mathrm{i}\bar{q}j} \tag{S12}$$

$$= \frac{1}{N}\sum_{j=1}^{N} \left[\mathbf{J}_{11}\tilde{x}_j + \mathbf{J}_{12}\tilde{y}_j + \sum_{r\neq j} [\mathbf{J}_{11}^r \tilde{x}_r + \mathbf{J}_{12}^r \tilde{y}_r] \right] e^{-2\pi \mathrm{i}\bar{q}j} \tag{S13}$$

$$= \frac{\mathbf{J}_{11}}{N}\sum_{j=1}^{N} \tilde{x}_j e^{-2\pi \mathrm{i}\bar{q}j} + \frac{\mathbf{J}_{12}}{N}\sum_{j=1}^{N} \tilde{y}_j e^{-2\pi \mathrm{i}\bar{q}j} + \frac{1}{N}\sum_{j=1}^{N}\sum_{r\neq j} [\mathbf{J}_{11}^r \tilde{x}_r + \mathbf{J}_{12}^r \tilde{y}_r] e^{-2\pi \mathrm{i}\bar{q}j} \tag{S14}$$

$$= \mathbf{J}_{11}\xi_q + \mathbf{J}_{12}\eta_q + \frac{1}{N}\sum_{j=1}^{N}\sum_{r\neq j} [\mathbf{J}_{11}^r \tilde{x}_r + \mathbf{J}_{12}^r \tilde{y}_r] e^{-2\pi \mathrm{i}\bar{q}j}, \tag{S15}$$

where we used the definitions in Eq. (S10) and Eq. (S11). The third term of Eq. (S15) requires more thought. The goal is to write it in terms of ξ_q exclusively. Let us focus on the terms involving $\tilde{x}_r$ first. Take $r = j + \Delta j$, $\Delta j \in S$, where S is the set of all integers such that $j + \Delta j$ is an index of a cell and $\Delta j \neq 0$. Notice that the indexation of $\mathbf{J}_{11}^r = \mathbf{J}_{11}^{j+\Delta j}$ is always relative to Δj and therefore constant on j (F_x and F_y do not change with j). Thus we may take $\mathbf{J}_{11}^r \equiv \mathbf{J}_{11}^{\Delta j}$ and write

$$\frac{1}{N}\sum_{j=1}^{N}\sum_{r\neq j} \mathbf{J}_{11}^r \tilde{x}_r e^{-2\pi \mathrm{i}\bar{q}j} = \sum_{\Delta j \in S} \mathbf{J}_{11}^{\Delta j} \frac{1}{N}\sum_{j=1}^{N} \tilde{x}_{j+\Delta j} e^{-2\pi \mathrm{i}\bar{q}j} = \sum_{\Delta j \in S} \mathbf{J}_{11}^{\Delta j} \xi_q e^{2\pi \mathrm{i}\bar{q}\Delta j}. \tag{S16}$$

The last equality is obtained by seeing that, excluding the sum over Δj, we have

$$\frac{1}{N}\sum_{j=1}^{N} \tilde{x}_{j+\Delta j} e^{-2\pi \mathrm{i}\bar{q}j} = \frac{e^{2\pi \mathrm{i}\bar{q}\Delta j}}{N}\sum_{j=1}^{N} \tilde{x}_{j+\Delta j} e^{-2\pi \mathrm{i}\bar{q}(j+\Delta j)} \tag{S17}$$

$$= \frac{e^{2\pi \mathrm{i}\bar{q}\Delta j}}{N}\sum_{j=1}^{N} \tilde{x}_j e^{-2\pi \mathrm{i}\bar{q}j} \tag{S18}$$

$$= \xi_q e^{2\pi \mathrm{i}\bar{q}\Delta j}, \tag{S19}$$

where we used the fact that we are working on the $\mathbb{Z}/N$ ring, thus $\tilde{x}_j = \tilde{x}_{j+N}$ and the sum term is N-periodic. We apply a similar analysis to $\tilde{y}$. This shows that any term involving $\tilde{x}_{j+\Delta j}$ or $\tilde{y}_{j+\Delta j}$, $\forall \Delta j \in S$, can be transformed into a linear term involving ξ_q or η_q, respectively. Hence, we have that

$$\frac{1}{N}\sum_{j=1}^{N}\sum_{r\neq j} [\mathbf{J}_{11}^r \tilde{x}_r + \mathbf{J}_{12}^r \tilde{y}_r] e^{-2\pi \mathrm{i}\bar{q}j} = \sum_{\Delta j \in S} \left[\mathbf{J}_{11}^{\Delta j}\xi_q + \mathbf{J}_{12}^{\Delta j}\eta_q \right] e^{2\pi \mathrm{i}\bar{q}\Delta j} \tag{S20}$$

$$= \xi_q \sum_{\Delta j \in S} \mathbf{J}_{11}^{\Delta j} e^{2\pi \mathrm{i}\bar{q}\Delta j} + \eta_q \sum_{\Delta j \in S} \mathbf{J}_{12}^{\Delta j} e^{2\pi \mathrm{i}\bar{q}\Delta j}. \tag{S21}$$

We may say that such linearisation leads to four functions that take into account the spatial coupling terms of each equation, depending solely on q. In matrix form, such functions can be captured by

$$\mathbf{\Omega}_{\bar{q}} \equiv \mathbf{\Omega}_{\bar{q}}(q) = \sum_{\Delta j \in S} \begin{pmatrix} \mathbf{J}_{11}^{\Delta j} e^{2\pi \mathrm{i}\bar{q}\Delta j} & \mathbf{J}_{12}^{\Delta j} e^{2\pi \mathrm{i}\bar{q}\Delta j} \\ \mathbf{J}_{21}^{\Delta j} e^{2\pi \mathrm{i}\bar{q}\Delta j} & \mathbf{J}_{22}^{\Delta j} e^{2\pi \mathrm{i}\bar{q}\Delta j} \end{pmatrix} = \sum_{\Delta j \in S} \mathbf{J}^{\Delta j} e^{2\pi \mathrm{i}\bar{q}\Delta j}. \tag{S22}$$

In general, it is then possible to rewrite Eq. (S1)-Eq. (S2) with respect to (ξ_q, η_q) to get the following system of constant-coefficient linear differential equations

$$\dot{\xi}_q = F_\xi(\xi_q, \eta_q) \simeq (\mathbf{J}_{11} + \mathbf{\Omega}_{\bar{q}11})\xi_q + (\mathbf{J}_{12} + \mathbf{\Omega}_{\bar{q}12})\eta_q \tag{S23}$$

$$\dot{\eta}_q = F_\eta(\xi_q, \eta_q) \simeq (\mathbf{J}_{21} + \mathbf{\Omega}_{\bar{q}21})\xi_q + (\mathbf{J}_{22} + \mathbf{\Omega}_{\bar{q}22})\eta_q \tag{S24}$$

or simply

$$\frac{d}{dt}\begin{pmatrix} \xi_q \\ \eta_q \end{pmatrix} \simeq \mathbf{L}_{\bar{q}} \begin{pmatrix} \xi_q \\ \eta_q \end{pmatrix}, \tag{S25}$$

where $\mathbf{L}_{\bar{q}} = \mathbf{J} + \mathbf{\Omega}_{\bar{q}}$. The general solution of Eq. (S25) is then given by

$$\begin{pmatrix} \xi_q \\ \eta_q \end{pmatrix} = C^+_{\bar{q}} \mathbf{v}^+_{\bar{q}} e^{\lambda^+_{\bar{q}} t} + C^-_{\bar{q}} \mathbf{v}^-_{\bar{q}} e^{\lambda^-_{\bar{q}} t}, \tag{S26}$$

where $\lambda^\pm_{\bar{q}}$ and $\mathbf{v}^\pm_{\bar{q}}$ are the eigenvalues and eigenvectors of $\mathbf{L}_{\bar{q}}$. $C^+_{\bar{q}}$ and $C^-_{\bar{q}}$ are constants depending on the initial conditions of the problem (note that they are different for each q, since each yields a separate system). We have

$$\lambda^\pm_{\bar{q}} = \frac{\tau_{\bar{q}} \pm \sqrt{\tau^2_{\bar{q}} - 4\sigma_{\bar{q}}}}{2} \tag{S27}$$

$$= \frac{1}{2}\left(\mathbf{L}_{\bar{q}11} + \mathbf{L}_{\bar{q}22} \pm \sqrt{(\mathbf{L}_{\bar{q}11} + \mathbf{L}_{\bar{q}22})^2 - 4(\mathbf{L}_{\bar{q}11}\mathbf{L}_{\bar{q}22} - \mathbf{L}_{\bar{q}12}\mathbf{L}_{\bar{q}21})} \right), \tag{S28}$$

where, in this case,

$$\tau_{\bar{q}} = \mathrm{Tr}(\mathbf{L}_{\bar{q}}) = \mathbf{L}_{\bar{q}11} + \mathbf{L}_{\bar{q}22} \tag{S29}$$

$$\sigma_{\bar{q}} = \det(\mathbf{L}_{\bar{q}}) = \mathbf{L}_{\bar{q}11}\mathbf{L}_{\bar{q}22} - \mathbf{L}_{\bar{q}12}\mathbf{L}_{\bar{q}21}. \tag{S30}$$

The solution of Eq. (S5) follows by applying the variable change Eq. (S8)-Eq. (S9) to the previous solution, leading to

$$\begin{pmatrix} \tilde{x}_j \\ \tilde{y}_j \end{pmatrix} = \sum_{q=1}^{N} \left[C^+_{\bar{q}} \mathbf{v}^+_{\bar{q}} e^{\lambda^+_{\bar{q}} t} + C^-_{\bar{q}} \mathbf{v}^-_{\bar{q}} e^{\lambda^-_{\bar{q}} t} \right] e^{2\pi \mathrm{i} \bar{q} j}. \tag{S31}$$

We argue that a homogeneous steady state (x^*, y^*) is linearly stable if and only if $\mathrm{Re}(\lambda^\pm_{\bar{q}}) < 0$, $\forall q$. We are now interested in studying what happens to the patterning solutions as $t \to \infty$. The real parts of the eigenvalues characterise the exponential growth rate along the eigenvectors, and so, if $\mathrm{Re}(\lambda^\pm_{\bar{q}}) < 0$, $\forall \bar{q}$, perturbations do not grow and the homogeneous solution is linearly stable. In contrast, the maximum value of $\mathrm{Re}(\lambda^\pm_{\bar{q}})$ indicates the fastest growing mode or wavelength $\bar{q}$ at the onset of instability. When such a value is positive, the homogeneous state is linearly unstable, and a pattern with the characteristic wavelength of the set of modes $\bar{q}$ that maximise $\mathrm{Re}(\lambda^\pm_{\bar{q}})$ arises for small t. For large t, we expect a dominant pattern to emerge and a consequent simplification of Eq. (S31) given by the superposition of the fastest growing modes, although this may not be true if nonlinearities determine emergent patterning. This translates into a maximisation problem over all $\bar{q}$ (note that N, in this case, is simply a refinement of the discretisation and, therefore, does not affect the maximisation problem). That is, we want to solve

$$\max_{\bar{q}} \mathrm{Re}(\lambda^+_{\bar{q}}) = \max_{\bar{q}} \mathrm{Re}\left[\frac{\tau_{\bar{q}} + \sqrt{\tau^2_{\bar{q}} - 4\sigma_{\bar{q}}}}{2} \right] \tag{S32}$$

$$= \frac{1}{2} \max_{\bar{q}} \mathrm{Re}\left[\mathbf{L}_{\bar{q}11} + \mathbf{L}_{\bar{q}22} + \sqrt{(\mathbf{L}_{\bar{q}11} + \mathbf{L}_{\bar{q}22})^2 - 4(\mathbf{L}_{\bar{q}11}\mathbf{L}_{\bar{q}22} - \mathbf{L}_{\bar{q}12}\mathbf{L}_{\bar{q}21})} \right]. \tag{S33}$$

Since $\mathbf{J}$ is independent of $\bar{q}$, we only need to look into optimising the terms involving $\mathbf{\Omega}_{\bar{q}}$. This may be hard in general, but, despite the complexity in Eq. (S33), the coupling terms regard only the terms $\mathbf{\Omega}_{\bar{q}12}$ and $\mathbf{\Omega}_{\bar{q}21}$ in many applications, as we will see in Example 1.1 and the case of Notch-Delta below. Once the set of fastest-growing modes (maximisers) $\mathcal{W}$ is obtained, the sum in Eq. (S31) is restricted to this set and becomes, asymptotically,

$$\begin{pmatrix} \tilde{x}_j \\ \tilde{y}_j \end{pmatrix} \approx \mathbf{v}^* e^{\lambda^* t} \sum_{\bar{q} \in \mathcal{W}} C^+_{\bar{q}} e^{2\pi \mathrm{i} \bar{q} j}, \tag{S34}$$

where λ^* is the growth rate corresponding to the fastest growing mode (eigenvalue with the largest real part) and $\mathbf{v}^*$ its corresponding eigenvector. Small perturbations grow exponentially on a time scale of order $1/\mathrm{Re}(\lambda^*)$.

Two-dimensional array

Consider now a $N \times M$ two-dimensional lattice where each cell is labelled by (j,k), with $1 \leq j \leq N, 1 \leq k \leq M$. We ignore the lattice shape for now. Again, we study the dynamics of two species x and y. Notice first that the main difference between this case and the one-dimensional array studied before is that now our decoupling and change of variables must account for two indices as well. Therefore, we relabel $j \equiv (j,k)$ in our previous analysis and aim to solve the system

$$\dot{x}_{j,k} = F_x(x_{j,k}, \{x_r\}, y_{j,k}, \{y_r\}) \tag{S35}$$

$$\dot{y}_{j,k} = F_y(x_{j,k}, \{x_r\}, y_{j,k}, \{y_r\}), \tag{S36}$$

where $r \neq (j,k)$. Linearisation leads to

$$\frac{d}{dt}\begin{pmatrix}\tilde{x}_{j,k}\\ \tilde{y}_{j,k}\end{pmatrix} \simeq \mathbf{J}\begin{pmatrix}\tilde{x}_{j,k}\\ \tilde{y}_{j,k}\end{pmatrix} + \sum_{r\neq(j,k)} \mathbf{J}^r \begin{pmatrix}\tilde{x}_r\\ \tilde{y}_r\end{pmatrix}. \tag{S37}$$

Using the two-dimensional Fourier transform, we may change the variables to get, for $1 \leq q \leq N$ and $1 \leq p \leq M$,

$$\tilde{x}_{j,k} = \sum_{q=1}^{N}\sum_{p=1}^{M} \xi_{q,p} e^{2\pi \mathrm{i}(qj/N + pk/M)} \tag{S38}$$

$$\tilde{y}_{j,k} = \sum_{q=1}^{N}\sum_{p=1}^{M} \eta_{q,p} e^{2\pi \mathrm{i}(qj/N + pk/M)}, \tag{S39}$$

with inverted transform given by

$$\xi_{q,p} = \frac{1}{MN}\sum_{k=1}^{M}\sum_{j=1}^{N} \tilde{x}_{j,k} e^{-2\pi \mathrm{i}(qj/N + pk/M)} \tag{S40}$$

$$\eta_{q,p} = \frac{1}{MN}\sum_{k=1}^{M}\sum_{j=1}^{N} \tilde{y}_{j,k} e^{-2\pi \mathrm{i}(qj/N + pk/M)}. \tag{S41}$$

Following the steps in the previous section, we easily see that the spatial coupling function is now given by

$$\mathbf{\Omega}_{\bar{q},\bar{p}} \equiv \mathbf{\Omega}_{\bar{q},\bar{p}}(q,p) = \sum_{\Delta jk \in S} \mathbf{J}^{\Delta jk} e^{2\pi \mathrm{i}(\bar{q}\Delta j + \bar{p}\Delta k)}, \tag{S42}$$

where $(\bar{q},\bar{p}) = (q/N, p/M)$ and $\Delta jk = (\Delta j, \Delta k)$. In this case, we took $r = (j+\Delta j, k+\Delta k)$, $(\Delta j, \Delta k) \in S$, where S is now the set of all pairs of integers such that $(j+\Delta j, k+\Delta k)$ is an index of a cell and $(\Delta j, \Delta k) \neq (0,0)$. $\mathbf{J}^{\Delta jk}$ is given, as before, by Eq. (S6). One interesting aspect of this generalised analysis is that it is independent of the lattice shape, as long as the connectivity matrix corresponds to a regular graph (S is independent of indexes). Notice that a generalisation to any spatial dimension follows easily from this step. The particular case when weighting is symmetric is discussed in Example 1.1. We then obtain the system

$$\frac{d}{dt}\begin{pmatrix}\xi_{q,p}\\ \eta_{q,p}\end{pmatrix} \simeq \mathbf{L}_{\bar{q},\bar{p}}\begin{pmatrix}\xi_{q,p}\\ \eta_{q,p}\end{pmatrix}, \tag{S43}$$

where $\mathbf{L}_{\bar{q},\bar{p}} = \mathbf{J} + \mathbf{\Omega}_{\bar{q},\bar{p}}$. The general solution of Eq. (S43) is then given by

$$\begin{pmatrix}\xi_{q,p}\\ \eta_{q,p}\end{pmatrix} = C^+_{\bar{q},\bar{p}} e^{\lambda^+_{\bar{q},\bar{p}} t}\mathbf{v}^+_{\bar{q},\bar{p}} + C^-_{\bar{q},\bar{p}} e^{\lambda^-_{\bar{q},\bar{p}} t}\mathbf{v}^-_{\bar{q},\bar{p}}, \tag{S44}$$

where $\lambda^{\pm}_{\bar{q},\bar{p}}$ and $\mathbf{v}^{\pm}_{\bar{q},\bar{p}}$ are the eigenvalues and eigenvectors of the matrix $\mathbf{L}_{\bar{q},\bar{p}}$. $C^+_{\bar{q},\bar{p}}$ and $C^-_{\bar{q},\bar{p}}$ are constants depending on the initial conditions of the problem. The solution to Eq. (S37) is then given by

$$\begin{pmatrix}\tilde{x}_{j,k}\\ \tilde{y}_{j,k}\end{pmatrix} = \sum_{q=1}^{N}\sum_{p=1}^{M}\left[C^+_{\bar{q},\bar{p}} e^{\lambda^+_{\bar{q},\bar{p}} t}\mathbf{v}^+_{\bar{q},\bar{p}} + C^-_{\bar{q},\bar{p}} e^{\lambda^-_{\bar{q},\bar{p}} t}\mathbf{v}^-_{\bar{q},\bar{p}}\right] e^{2\pi \mathrm{i}(\bar{q}j + \bar{p}k)}. \tag{S45}$$

Similar to the one-dimensional case, the fastest growing modes are obtained by maximizing the real part of the growth rates over $\bar{q}$ and $\bar{p}$, and the asymptotic behaviour of the solution of the linearised problem is dominated by the terms corresponding to the fastest growing modes

$$\begin{pmatrix}\tilde{x}_{j,k}\\ \tilde{y}_{j,k}\end{pmatrix} \approx \mathbf{v}^* e^{\lambda^* t} \sum_{(\bar{q},\bar{p})\in\mathcal{W}} C^+_{\bar{q},\bar{p}} e^{2\pi \mathrm{i}(\bar{q}j + \bar{p}k)}, \tag{S46}$$

where λ^* is the growth rate corresponding to the fastest growing modes, which comprise $\mathcal{W}$, and $\mathbf{v}^*$ its corresponding eigenvector. When nonlinearities affect the solution, we do not expect, in general, solutions of the form Eq. (S46) to arise in the full nonlinear system. The two-dimensional system will be the main focus in this paper.

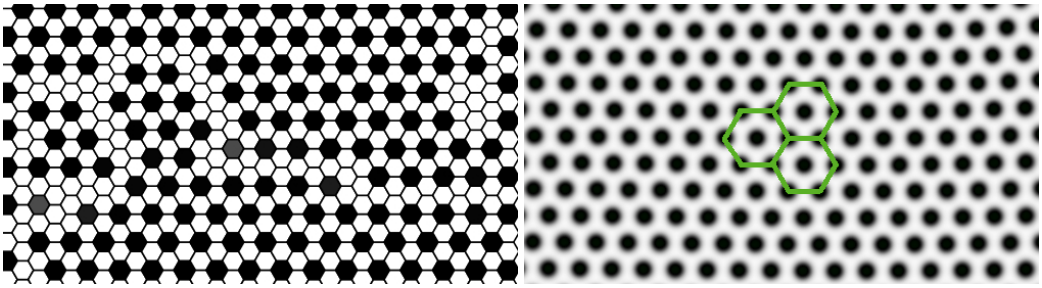

(a) (b)

Figure S1. Reaction-diffusion systems mimic juxtacrine signalling.
(a) Lateral inhibition patterning. **(b)** Soliton-type patterning via the Gray-Scott Model of a reaction-diffusion system resembles lateral inhibition on a hexagonal lattice (sketched in green). Here $F = 0.03$, $\kappa = 0.062$ and $D_n = 2D_d$.

Remark 1.1 (Continuum limit and reaction-diffusion systems) Feedback interactions between morphogens (understood as long-range diffusible ligands in many contexts (Lawrence and Struhl, 1996; Vincent and Briscoe, 2001; Tabata and Takei, 2004)) have previously been discussed by Alan Turing regarding skin patterning in his famous paper (Turing, 1952). Many of the patterns discussed in this work share similar features with the type of patterns expected from long-range signalling via filopodia (Meinhardt, 2003, 2008; Kondo, 2009). While diffusion is a linear process where the flux is proportional to the concentration gradient of morphogens, discrete lattice-based long-range signalling imposes nonlinear effects on patterning, often due to the production functions (Hill functions in our case). Nonetheless, as suggested in Binshtok and Sprinzak (2018); Hamada et al. (2014), the mathematical equivalence between the two approaches is worth noticing.
Consider the one-dimensional translationally invariant system given by

$$\frac{du_i}{dt} = f(u_i, v_{i-1}, v_{i+1}) \tag{S47}$$

$$\frac{dv_i}{dt} = g(u_i, v_i). \tag{S48}$$

By considering the continuum limit $u_i \to u(i\Delta)$ (and similarly for v_i), we get

$$\frac{\partial u(t,x)}{\partial t} = f(u(t,x), v(t,x-\Delta), v(t,x+\Delta)) \tag{S49}$$

$$\frac{\partial v(t,x)}{\partial t} = g(u(t,x), v(t,x)). \tag{S50}$$

Expanding to second order in Δ leads to

$$\frac{\partial u(t,x)}{\partial t} \simeq f(u(t,x), v(t,x) - \Delta\partial_x v + \frac{1}{2}\Delta^2\partial_{xx}v, v(t,x) + \Delta\partial_x v + \frac{1}{2}\Delta^2\partial_{xx}v) \tag{S51}$$

$$\frac{\partial v(t,x)}{\partial t} = g(u(t,x), v(t,x)). \tag{S52}$$

A consistent expansion of f will lead to the reaction-diffusion form, possibly with a convection (∂_x) term (in the general case). If, for example, $f(u_i, v_{i-1}, v_{i+1}) = v_{i-1} + v_{i+1}$, we may identify $v_{i-1} + v_{i+1} \sim 2v + h\partial_{xx}v$, for some small $h \equiv \Delta^2$.
Figure S1 compares a simulation of the Collier model with the Gray-Scott model of reaction-diffusion (Doelman et al., 1997; McGough and Riley, 2004), given by

$$\frac{\partial n}{\partial t} = -nd^2 + \mathcal{F}(1-n) + D_n\nabla n \tag{S53}$$

$$\frac{\partial d}{\partial t} = nd^2 - (\mathcal{F}+\kappa)d + D_d\nabla d, \tag{S54}$$

where $\mathcal{F}$ is the feed rate, κ is the kill rate and D_n and D_d are the diffusion rates. Lateral inhibition is mimicked for specific ranges of such rates. Sparser patterns might be expected under similar regimes.

Examples

So far, we have been discussing linear stability methods in a fairly general way. This section discusses coupling simplifications based on symmetry and presents an application to a one-dimensional system. The two-dimensional case will be studied in the particular case of Notch-Delta signalling.

Example 1.1 (Simplification of coupling functions) In many cases, the coupling functions $\mathbf{\Omega}_{\bar{q}}$ can be simplified under specific conditions. In the one-dimensional ring, for example, if the dependence on x_r, $r \neq j$, is given as a sum of indexed terms corresponding to immediate neighbours, that is, $r \in \{j-1, j+1\}$ ($\Delta j = \pm 1$) and

$$F_x(x_j, \{x_r\}, y_j, \{y_r\}) \equiv F_x(x_{j-1} + x_{j+1}) \tag{S55}$$
$$F_y(x_j, \{x_r\}, y_j, \{y_r\}) \equiv F_y(x_j, y_j), \tag{S56}$$

then

$$\mathbf{J}^{\pm 1} = \begin{pmatrix} F_x'(2x^*) & 0 \\ 0 & 0 \end{pmatrix}. \tag{S57}$$

Without loss of generality, take $F_x'(2x^*) = 1$. Thus the only non-zero term in $\mathbf{\Omega}_{\bar{q}}$ is

$$\mathbf{\Omega}_{\bar{q}11} = e^{2\pi \mathrm{i}\bar{q}} + e^{-2\pi \mathrm{i}\bar{q}} = 2\cos(2\pi\bar{q}). \tag{S58}$$

Generalising to the mth neighbour of cell j, that is, $\Delta j \in S^m \equiv \{\pm m\}$, leads to

$$\mathbf{\Omega}_{\bar{q}11} = 2\cos(2\pi\bar{q}m). \tag{S59}$$

Notice now that if we consider F_x of the form $F_x\left(\sum_{\Delta j \in \Sigma S^m} x_{j+\Delta j}\right)$, with $\Sigma S^m = \{\pm 1, ..., \pm m\}$, then the coupling function is easily obtained by summing, up to m, the previous terms. Other simplifications are possible depending on the nature of $\mathbf{J}$.

In two dimensions, we have more interesting cases to look at. First, depending on the lattice shape, $(\Delta j, \Delta k)$ might mean different things regarding which cells are neighbours of a focal cell (j,k). The analysis, however, is independent of this. Thus we merely refer to lattice shapes as motivation for the choices of S, as mentioned before. In a squared lattice, one of two cases is often relevant: either a cell is affected by only 4 neighbours or all 8 (Figure S2a). In the first case, we take $S = \{(0, \pm 1), (\pm 1, 0)\}$. Here, we use the notation $\Omega_{\bar{q},\bar{p}} \equiv [\mathbf{\Omega}_{\bar{q},\bar{p}}]_{11}$ as a simplification (it is irrelevant which variable is affected). Again, we take equally weighted sums of the neighbours' terms. In this case, we get, from Eq. (S42),

$$\Omega_{\bar{q},\bar{p}} = \sum_{\Delta j \in S} e^{2\pi \mathrm{i}(\bar{q}\Delta j + \bar{p}\Delta k)} = 2\left[\cos(2\pi\bar{q}) + \cos(2\pi\bar{p})\right]. \tag{S60}$$

In the case of the regular hexagonal lattice, we have several labelling possibilities. Using the labelling in Figure S2b, we get, for immediate neighbours, $S = \{(\pm 1, 0), (0, \pm 1), \pm(1,1)\}$ and

$$\Omega_{\bar{q},\bar{p}} = 2\left[\cos(2\pi\bar{q}) + \cos(2\pi\bar{p}) + \cos\left(2\pi\left(\bar{q} + \bar{p}\right)\right)\right]. \tag{S61}$$

More generally, if the coupling weights, captured by $\mathbf{J}^{\Delta jk}$, are symmetric, that is, $\mathbf{J}^{\Delta jk} = \mathbf{J}^{\Delta(-j)(-k)}$, then

$$\mathbf{\Omega}_{\bar{q},\bar{p}} = \sum_{\Delta jk \in S} \mathbf{J}^{\Delta jk} \cos(2\pi(\bar{q}\Delta j + \bar{p}\Delta k)). \tag{S62}$$

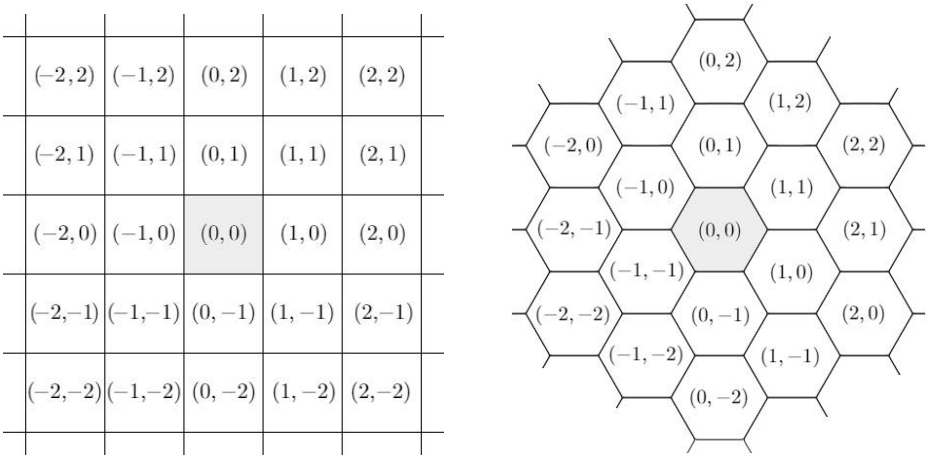

(a) Squared lattice **(b)** Hexagonal lattice

Figure S2. Cell lattices and relative indexation.

Example 1.2 (Ring of cells) Consider two species x and y governed by the following equations on a ring of N cells

$$\frac{dx_j}{dt} = f\left(\frac{y_{j-1}+y_{j+1}}{2}\right) + \mu x_j \tag{S63}$$

$$\frac{dy_j}{dt} = g(x_j) + \rho y_j, \tag{S64}$$

where $\mu, \rho \in \mathbb{R}$. Define

$$F_x(x_j, y_j, y_{j-1}, y_{j+1}) = f\left(\frac{y_{j-1}+y_{j+1}}{2}\right) + \mu x_j \tag{S65}$$

$$F_y(x_j, y_j, y_{j-1}, y_{j+1}) = g(x_j) + \rho y_j. \tag{S66}$$

Following linearisation around a homogeneous steady state, the relevant matrices are given by

$$\mathbf{J} = \begin{pmatrix} \mu & 0 \\ g'(x_j) & \rho \end{pmatrix}\Bigg|_{(x^*,y^*)} = \begin{pmatrix} \mu & 0 \\ g'(x^*) & \rho \end{pmatrix} \tag{S67}$$

$$\mathbf{J}^{\pm 1} = \begin{pmatrix} 0 & \frac{1}{2}f'\left(\frac{y_{j-1}+y_{j+1}}{2}\right) \\ 0 & 0 \end{pmatrix}\Bigg|_{(x^*,y^*)} = \begin{pmatrix} 0 & \frac{1}{2}f'(y^*) \\ 0 & 0 \end{pmatrix}. \tag{S68}$$

In this case, we have $S = \{-1, 1\}$ and $\mathbf{J}^1 = \mathbf{J}^{-1}$ (not to be confused with the inverse of a matrix). Thus we may use Eq. (S62) from Example 1.1 and write

$$\mathbf{\Omega}_{\bar{q}} = \sum_{\Delta j \in S} \mathbf{J}^{\Delta j} \cos(2\pi \bar{q} \Delta j) \tag{S69}$$

$$= \begin{pmatrix} 0 & f'(y^*)(\cos(2\pi\bar{q}) + \cos(-2\pi\bar{q})) \\ 0 & 0 \end{pmatrix} \tag{S70}$$

$$= \begin{pmatrix} 0 & 2f'(y^*)\cos(2\pi\bar{q}) \\ 0 & 0 \end{pmatrix} \tag{S71}$$

and so

$$\mathbf{L}_{\bar{q}} = \mathbf{J} + \mathbf{\Omega}_{\bar{q}} = \begin{pmatrix} \mu & 2f'(y^*)\cos(2\pi\bar{q}) \\ g'(x^*) & \rho \end{pmatrix}. \tag{S72}$$

We define the coupling term by $\Omega_{\bar{q}} \equiv 2\cos(2\pi\bar{q})$ (not to be confused with the matrix counterpart, $\mathbf{\Omega}_{\bar{q}}$, in bold) and let $A = f'(y^*)$ and $B = g'(x^*)$. In fact, in this case, $\Omega_{\bar{q}} = \mathbf{\Omega}_{\bar{q}12}/A$. The eigenvalues of $\mathbf{L}$ are then given by

$$\lambda^{\pm}_{\bar{q}} = \frac{1}{2}\left(\mathbf{L}_{\bar{q}11} + \mathbf{L}_{\bar{q}22} \pm \sqrt{(\mathbf{L}_{\bar{q}11} + \mathbf{L}_{\bar{q}22})^2 - 4(\mathbf{L}_{\bar{q}11}\mathbf{L}_{\bar{q}22} - \mathbf{L}_{\bar{q}12}\mathbf{L}_{\bar{q}21})}\right) \tag{S73}$$

$$= \frac{1}{2}\left(\mu + \rho \pm \sqrt{(\mu+\rho)^2 - 4(\mu\rho - AB\Omega_{\bar{q}})}\right). \tag{S74}$$

From the previous analysis, the homogeneous solution is linearly stable if and only if $\mu + \rho < 0$ and $\mu\rho > AB\Omega_{\bar{q}}$ for all $\bar{q}$. Maximising $\mathrm{Re}(\lambda^{\pm}_{\bar{q}})$ with respect to $\bar{q}$ relies then on maximising $AB\Omega_{\bar{q}}$, since $AB\Omega_{\bar{q}} > \mu\rho$ leads to a heterogeneous solution.

Remark 1.2 (Euclidean and hexagonal distances)

For a focal cell i (R_0), the recursive definition of the signalling rings R_k as the set of cells that are immediate neighbours of cells in R_{k-1} and are not in $\bigcup_{n=1}^{k-1} R_n$ can be a bit ambiguous regarding the realistic reach of protrusions and the regular hexagonal lattice. First, notice that a hexagonal-Manhattan-type distance, $d_H(i,j)$, provides an alternative definition of such sets in the following way: a cell i is in R_k if it is not in $\bigcup_{n=1}^{k-1} R_n$ and $d_H(i,j) = k$ (between cell centres and assuming the Euclidean distance between the cell centres of two neighbouring cells is 1). d_H is hereafter named the *El Alto distance*, inspired by the peculiar hexagonally shaped urbanisation located in El Alto, Bolivia (Figure S3[1]).

Figure S3. Hexagonal layout on a neighbourhood of El Alto, Bolivia.

We recall that we assume signalling between a cell and any of its non-immediate neighbours occurs if it is within reach of protrusions. That is, if the Euclidean distance between both cell centres, $d_E(i,j)$, is less than a certain fixed threshold. It is then possible to write an equivalent definition of R_k using the Euclidean distance by defining the threshold $k-1 < d_E(i,j) \leq k$. However, this is only valid up to a specific value of k, so there is an important geometric difference between distances d_H and d_E on the hexagonal lattice.

In other words, above a specific k, the distance thresholds define different sets of cells. This first equivalence break occurs when the Euclidean distance to a cell in R_{k+1} is less than the El Alto distance to a cell in R_k. Hence, we want to find the smallest integer k such that

$$d_E(i, j \in R_{k+1}) < d_H(i, j \in R_k) \iff d_E(i, j \in R_{k+1}) < k. \tag{S75}$$

To determine the expression for $d_E(i, j \in R_{k+1})$, we first notice that such cells will be positioned towards the middle vertical section of the hexagonal lattice depicted in Figure S4a. To find the first k for which equivalence breaks, two minimal paths are possible, depending on the parity of k. The triangles in Figure S4b depict both the shortest Euclidean distance and a corresponding possible El Alto path for each R_k. Hence, we have two possibilities for the Euclidean distance, given by

$$d_E(i, j \in R_k) = \begin{cases} \frac{k\sqrt{3}}{2} & k \text{ even}, \\ \frac{\sqrt{3k^2+1}}{2} & k \text{ odd}. \end{cases} \tag{S76}$$

Then, it follows that

$$d_E(i, j \in R_{k+1}) < k \iff \begin{cases} \frac{\sqrt{3(k+1)^2+1}}{2} < k & k \text{ even}, \\ \frac{(k+1)\sqrt{3}}{2} < k & k \text{ odd}. \end{cases} \tag{S77}$$

$$\iff \begin{cases} k > 3 + \sqrt{13} \simeq 6.6056 & k \text{ even}, \\ k > \frac{\sqrt{3}}{2-\sqrt{3}} \simeq 6.4641 & k \text{ odd}. \end{cases} \tag{S78}$$

Hence, the equivalence between definitions fails for $k \geq 7$, meaning the R_k Euclidean definition for R_7 would already include cells in R_8. This observation shows that these two definitions would yield slightly different analysis for signalling at distant rings. We argue, however, that realistic protrusions do not usually reach R_7, and therefore the equivalent definitions work for most applications. However, the main text also discusses the analysis of such systems for theoretically longer protrusions under the El Alto distance definition.

Alternative definitions of R_k are possible with fixed Euclidean distance thresholds and can lead to different levels of complexity (Figures S4c-S4f). Interesting patterns emerge when considering signalling rings purely defined by their Euclidean radius. That is, cells belong to the same ring provided they have precisely the same Euclidean distance to the focal cell i (Figure S4d). By alternating the colouring of successive signalling rings, based on this definition and ordered from the distance to R_0, somewhat chaotic patterns emerge from such simple labelling (Figure S4f). In other words, we colour cells black or white dependent on their distance from the focal cell, alternating colour whenever a new set of cell centres intersects a circumference with an increasing radius, centered at R_0. If the number of greyscale colouring steps is increased (starting with the binary black

[1] Attribution information: Google Maps, Imagery ©2022 CNES / Airbus, Maxar Technologies, Map data ©2022.

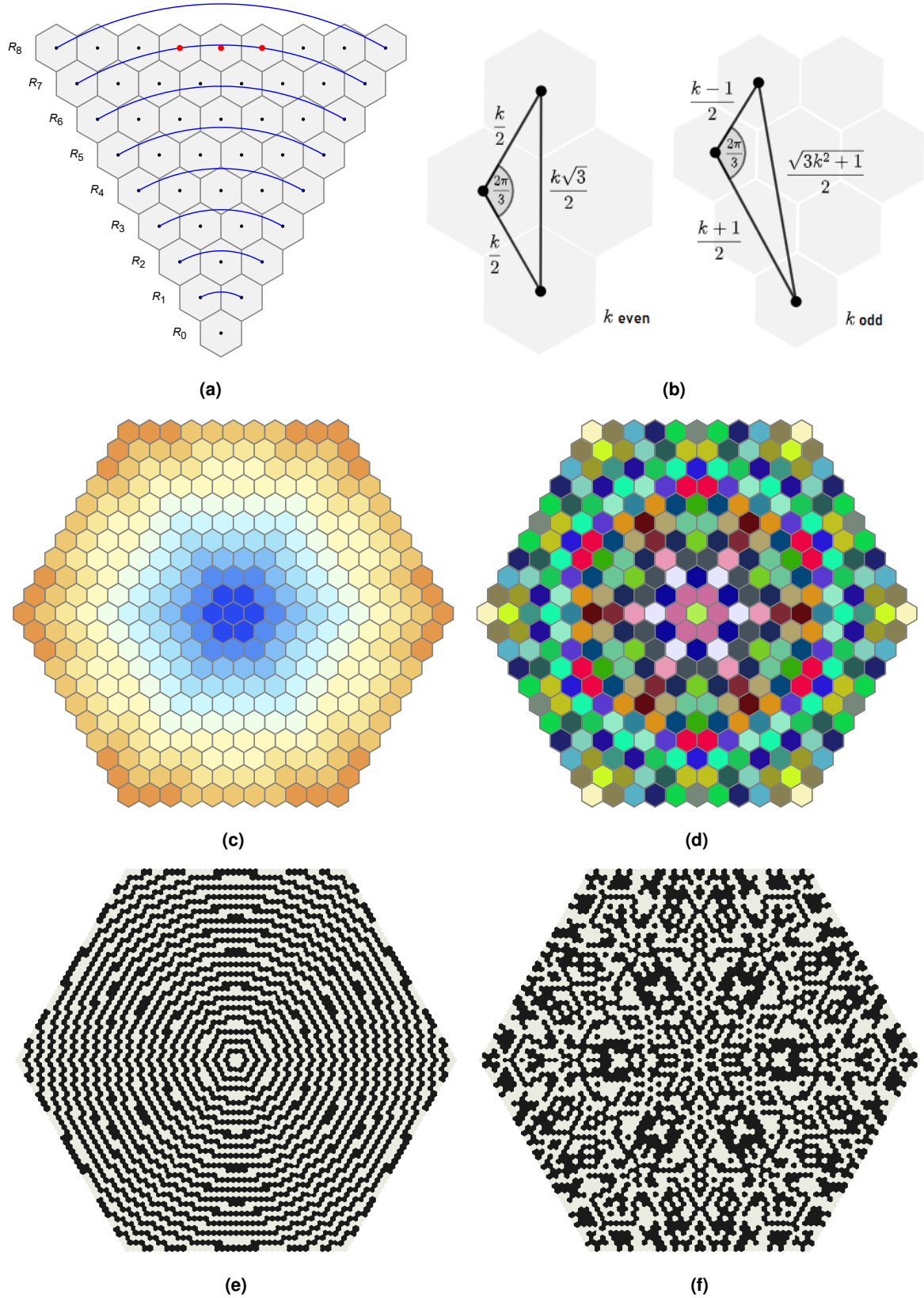

Figure S4. (Caption overleaf.)

Figure S4. (Overleaf.) **Euclidean and El Alto distances on hexagonal lattices.**
(a) The fixed Euclidean distance (radius of the blue arcs) defined at R_7 is greater or equal to the distance of three cell centres (in red) in R_8, breaking the definition equivalence. **(b)** Two minimal paths are possible, depending on the parity of k. **(c-d)** Signalling rings based on two different distance-based definitions. Cells are in the same ring (same colour) if **(c)** $k-1 < d_E(i,j) \leq k$, or **(d)** they have exactly the same Euclidean distance to cell i. $k \leq 10$. **(e-f)** Intricate patterns emerge by alternating colouring of successive signalling rings based on the respective two definitions. $k \leq 40$.

or white), further fractal-like patterns arise (Video S4). The only coinciding rings under all definitions are R_0 and R_1. Since realistic cells are not regular hexagons, and protrusions are also subject to stochastic effects (such as different lengths and lifespans), we argue that the hexagonally isotropic signalling rings R_k provide a more realistic approximation of the signalling reach of protrusions when compared to the alternative discrete distance-based definition we presented.

Robustness and pattern selection

As discussed in the main text, Fourier analysis helps in describing pattern selection under LSA. We recall that the solution to the linearised problem is given by

$$\begin{pmatrix} \tilde{n}_{j,k}(t) \\ \tilde{d}_{j,k}(t) \end{pmatrix} = \sum_{q=1}^{N}\sum_{p=1}^{M} \left[C^{+}_{\bar{q},\bar{p}} e^{\lambda^{+}_{\bar{q},\bar{p}} t} \mathbf{v}^{+}_{\bar{q},\bar{p}} + C^{-}_{\bar{q},\bar{p}} e^{\lambda^{-}_{\bar{q},\bar{p}} t} \mathbf{v}^{-}_{\bar{q},\bar{p}} \right] e^{2\pi \mathrm{i}(\bar{q}j + \bar{p}k)}, \tag{S79}$$

where $\mathbf{v}^{\pm}_{\bar{q},\bar{p}}$ and $\lambda^{\pm}_{\bar{q},\bar{p}}$ are the eigenvectors and eigenvalues associated to $(\bar{q},\bar{p})$, respectively. $C^{+}_{\bar{q},\bar{p}}$ and $C^{-}_{\bar{q},\bar{p}}$ are constants depending on the initial conditions of the problem. Figure S6 shows the comparison between the final patterns from Figure 8 with a sensory organ precursor (SOP) cell filtering based on a specific threshold (percentage of steady state solution) and a numerical simulation. Figure S7 shows the dependence of cell fates on the choice of $C^{+}_{\bar{q},\bar{p}}$, as predicted by LSA.
Figure S6 compares the final patterns from Figure 8 with an SOP cell filtering based on a specific threshold (percentage of steady state solution) and a numerical simulation. In other words, the plots in each middle panel correspond to the selection of cells whose Delta level is above a specific threshold (d_T). It is noticeable that LSA predicts sparse patterning for a wide range of values of ϵ around bifurcations. It is only for $\epsilon \geq 0.4$ that sparser patterns emerge, yet more than two cell types are observable prior to filtering. Figure S7 shows the dependence of cell fates on the choice of $C^{+}_{\bar{q},\bar{p}}$. Similar to the conclusions for lateral inhibition in Collier et al. (1996), different choices of constants lead to fundamentally different SOP cell patterns and cell types. Considering imaginary constants, for example, leads to intermediary cell types in the case of $0 \leq \epsilon < 0.4$ (Figure S7a). This can also be seen for different values of h and k (O'Dea and King, 2011). Note that the bifurcation of $\Omega_{\bar{q},\bar{p}}$ at $\epsilon = 0.4$ (Figure 2b) can be mathematically shown by solving $\Omega_{\frac{1}{3},\frac{1}{3}}(\epsilon) = \Omega_{\bar{q},\bar{p}}(\epsilon)$ for ϵ and a minimising pair $(\bar{q},\bar{p}) \notin \{(1/3,1/3),(2/3,2/3)\}$. Given the minimisers in Figure 8b, we have that, with $(\bar{q},\bar{p}) = (1/4,1/4)$ for example, $\Omega_{\frac{1}{3},\frac{1}{3}}(\epsilon) = \Omega_{\frac{1}{4},\frac{1}{4}}(\epsilon) \Leftrightarrow \epsilon = 0.4$. As detailed in the main text, patterning timing was also studied in the deterministic scenario. Figure S5 shows some of the averaging results for parameter values near the bifurcations in Figure 3.

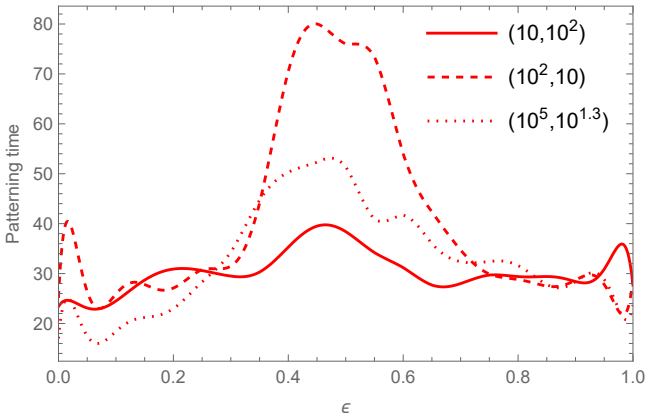

Figure S5. Patterning time with long-range signalling.
Average patterning time for different values of ϵ on 14×14 lattices, for each critical point. Here, $\overline{d} = 0.001$, and simulations were run over 30 different tissues per ϵ. The values of (r_t, b) are given on the plot.

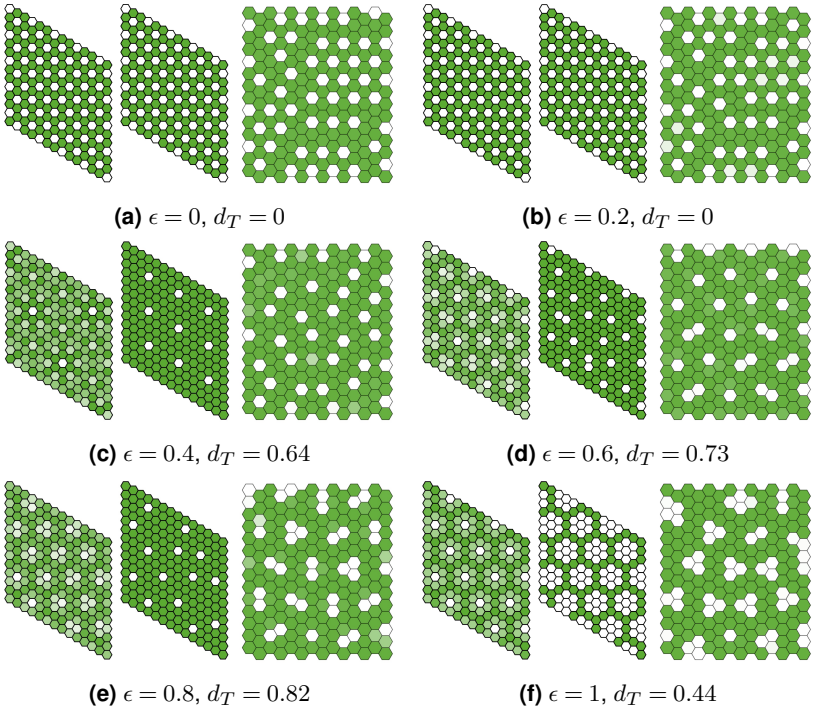

(a) $\epsilon = 0$, $d_T = 0$ **(b)** $\epsilon = 0.2$, $d_T = 0$

(c) $\epsilon = 0.4$, $d_T = 0.64$ **(d)** $\epsilon = 0.6$, $d_T = 0.73$

(e) $\epsilon = 0.8$, $d_T = 0.82$ **(f)** $\epsilon = 1$, $d_T = 0.44$

Figure S6. Pattern selection: threshold solutions and numerical comparisons.
Here are shown the final patterns predicted by LSA (left), threshold-based SOP cell detection with $d_i > d_T$ (middle) and a numerical simulation close to a bifurcation (right), for different values of ϵ and d_T. $C^+_{\bar{q},\bar{p}} = 1\ \forall(\bar{q},\bar{p})$, $h = k = 6$, $a = 10^{-5}$, $b = 10^{1.3}$ and $\nu = 1$.

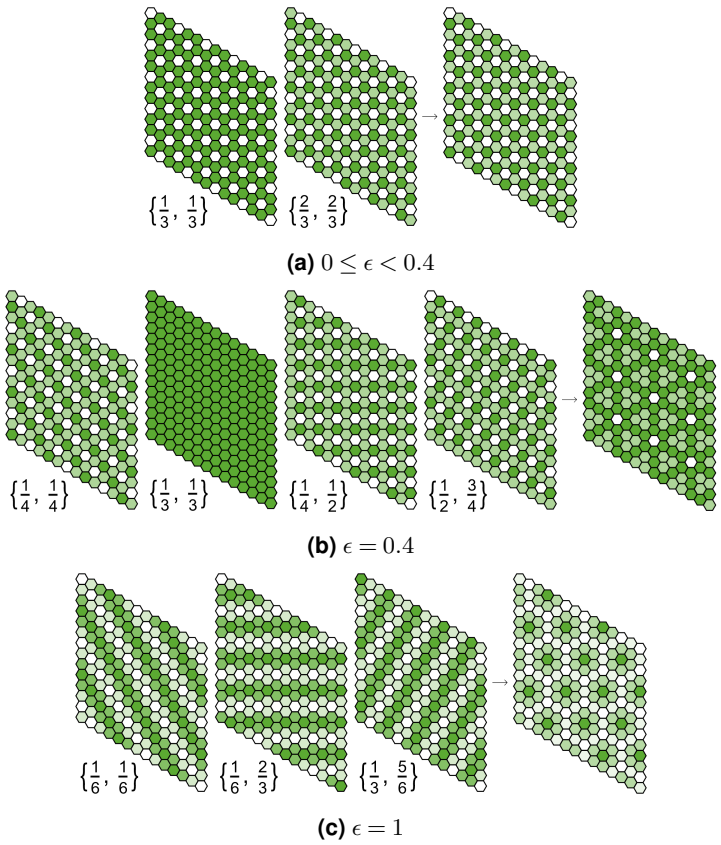

(a) $0 \leq \epsilon < 0.4$

(b) $\epsilon = 0.4$

(c) $\epsilon = 1$

Figure S7. Pattern selection: dependence on initial conditions.
(a) $\epsilon = 0$. $C^+_{\frac{1}{3},\frac{1}{3}} = 1$, $C^+_{\frac{2}{3},\frac{2}{3}} = 0.7$i. **(b)** $\epsilon = 0.4$, $C^+_{\frac{1}{3},\frac{1}{3}} = C^+_{\frac{2}{3},\frac{2}{3}} = 0$, $C^+_{\bar{q},\bar{p}} = 1$, $\forall \bar{q},\bar{p} \notin \{\{\frac{1}{3},\frac{1}{3}\}\{\frac{2}{3},\frac{2}{3}\}\}$. **(c)** $\epsilon = 1$, $C^+_{\bar{q},\bar{p}} = -1$, $\forall \bar{q},\bar{p}$.

Supplementary Note 2: Weakly nonlinear stability analysis

Motivated by theory from reaction-diffusion systems (Turing, 1952; Wollkind et al., 1994), we perform weakly nonlinear stability analysis (WNSA) to better understand the effects of nonlinear terms, based on the amplitude dynamics of the Fourier components corresponding to the fastest growing modes, expanding on LSA to deduce further patterning features derived from long-range signalling. The following discussion is presented in gradually increasing levels of complexity of differential systems.

One-dimensional systems

When performing LSA, we have looked for solutions to the following system

$$\frac{du}{dt} = F(u) \tag{S80}$$

of the type

$$u(t) = u^* + \tilde{u}, \tag{S81}$$

where u^* is the homogeneous solution and $\tilde{u}$ is a small perturbation which is solution to the linearised problem $\frac{d\tilde{u}}{dt} = F'(u^*)\tilde{u}$.
Motivated by the theory in reaction-diffusion systems, where the governing equations are nonlinear partial differential equations (PDEs), an approximation to the solution is obtained by introducing the finite amplitude function $A(t,x)$, where x is the spatial variable (Wollkind and Segel, 1970; Wollkind et al., 1984; Wollkind and Vislocky, 1990). For the space-independent system, we take solutions of the type

$$u(t) = \sum_{m=0}^{\infty} v_m A^m(t). \tag{S82}$$

A satisfies the following Landau equation (Aranson and Kramer, 2002)

$$\frac{dA}{dt}(t) = \sum_{m=0}^{\infty} b_m A^m(t), \tag{S83}$$

where $\{v_m\}$ are constants and $\{b_m\}$ are coefficients depending on the problem itself. $\{b_m\}$ are also known as Landau constants. This formulation, often named the Stuart-Watson nonlinear extension (Stuart, 1960; Watson, 1960), allows us to modify the linear expansion approach inherent to Eq. (S81) so that it will be applicable to higher-order terms. Approximate solutions are obtained by a severe truncation of the infinite series. Here, we take

$$u(t) = \sum_{m=0}^{K} v_m A^m(t) + O(A^{K+1}) \tag{S84}$$

and

$$\frac{dA}{dt}(t) = \sum_{m=0}^{K} b_m A^m(t) + O(A^{K+1}). \tag{S85}$$

In this case, substituting into Eq. (S80) leads to

$$\frac{du}{dt} = \sum_{m=0}^{K} v_m \frac{d}{dt}\left[A^m(t)\right] \tag{S86}$$

$$= \sum_{m=0}^{K} m v_m A^{m-1}(t) \frac{dA}{dt}(t) \tag{S87}$$

$$= \sum_{m=0}^{K} \sum_{j=0}^{K} m v_m b_j A^{m+j-1}(t). \tag{S88}$$

Solving Eq. (S84)-Eq. (S85) with fixed K for coefficients $\{v_m\}$ and $\{b_m\}$ leads to a sequence of m vector systems, each corresponding to a nonzero term of the form $v_m A^m(t)$ appearing explicitly in Eq. (S84). In general, we start by solving Eq. (S85) and then deduce $\{v_m\}$ and $\{b_m\}$ by differentiating Eq. (S84) and Taylor-expanding $F_A(A) \equiv F(u)$

around $A=0$. Previous works have solved this with $K=3$ for reaction-diffusion equations in different applications (Stephenson and Wollkind, 1995; Bozzini et al., 2015; Liu et al., 2018). We then need to solve the following system

$$\frac{du}{dt} = F_A(A) \tag{S89}$$

for the tuples (b_0,b_1,b_2,b_3) and (v_0,v_1,v_2,v_3), where

$$u(t) = v_0 + v_1 A(t) + v_2 A^2(t) + v_3 A^3(t) + O(A^4) \tag{S90}$$

$$\frac{dA}{dt}(t) = b_0 + b_1 A(t) + b_2 A^2(t) + b_3 A^3(t) + O(A^4). \tag{S91}$$

We take $v_0 \equiv u^*$. Then, substituting Eq. (S90)-Eq. (S91) into $\frac{du}{dt}$ yields

$$\begin{aligned}\frac{du}{dt} = {} & b_0 v_1 + (b_1 v_1 + 2 b_0 v_2)\, A(t) + (b_2 v_1 + 2 b_1 v_2 + 3 b_0 v_3)\, A^2(t) \\ & + (b_3 v_1 + 2 b_2 v_2 + 3 b_1 v_3)\, A^3(t) + O(A^4).\end{aligned} \tag{S92}$$

Taylor-expanding $F_A(A)$ around $A=0$ leads to

$$F_A(A) \equiv F(u^* + v_1 A(t) + v_2 A^2(t) + v_3 A^3(t)) \tag{S93}$$

$$\begin{aligned}& \simeq F(u^*) + v_1 F'(u^*)\, A(t) + \left(\frac{1}{2} v_1^2 F''(u^*) + v_2 F'(u^*)\right) A^2(t) \\ & + \left(\frac{1}{6} v_1^3 F^{(3)}(u^*) + v_2 v_1 F''(u^*) + v_3 F'(u^*)\right) A^3(t) + O(A^4).\end{aligned} \tag{S94}$$

Finally, equating the coefficients of $A^m(t)$ $(0 \le m \le 3)$ defines the system of 4 equations and 7 variables (excluding the trivial case $v_0 = u^*$)

$$m=0: \qquad b_0 v_1 = F(u^*) = 0 \tag{S95}$$

$$m=1: \qquad b_1 v_1 + 2 b_0 v_2 = v_1 F'(u^*) \tag{S96}$$

$$m=2: \qquad b_2 v_1 + 2 b_1 v_2 + 3 b_0 v_3 = \frac{1}{2} v_1^2 F''(u^*) + v_2 F'(u^*) \tag{S97}$$

$$m=3: \qquad b_3 v_1 + 2 b_2 v_2 + 3 b_1 v_3 = \frac{1}{6} v_1^3 F^{(3)}(u^*) + v_2 v_1 F''(u^*) + v_3 F'(u^*) \tag{S98}$$

from which, with $v_1 \neq 0$, we deduce

$$b_0 = 0 \tag{S99}$$

$$b_1 = F'(u^*) \tag{S100}$$

$$b_2 = \frac{v_1^2 F''(u^*) - 2 v_2 F'(u^*)}{2 v_1} \tag{S101}$$

$$b_3 = \frac{v_1^4 F^{(3)}(u^*) - 12 v_1 v_3 F'(u^*) + 12 v_2^2 F'(u^*)}{6 v_1^2}. \tag{S102}$$

This method provides a straightforward tool to explicitly determine weakly nonlinear approximations of the form Eq. (S90) for autonomous systems in one dimension.
Amplitude-based solutions of the form Eq. (S90) are assumed to capture the effects of harmonics of the fastest growing modes, appearing as space-independent components. In many cases, solutions have been restricted to amplitude equations of the form

$$\frac{dA}{dt}(t) = \lambda^* A(t) - \kappa A^3(t) + O(A^5), \tag{S103}$$

where λ^* is the fastest growth rate of weakly nonlinear perturbations. The sign of the Landau constant κ in this differential equation is relevant: if it is positive, then the effect of the term $-\kappa A^3(t)$ is to arrest the exponential growth of $A(t)$ at the value $\sqrt{\lambda^*/\kappa}$ (Turing, 1952). Given $(b_0,b_1,b_2,b_3) = (0,\lambda^*,0,-\kappa)$, we have that $F'(u^*) = \lambda^*$ and

$$(v_0,v_1,v_2,v_3) = \left(u^*, v_1, \frac{v_1^2 F''(u^*)}{2\lambda^*}, \frac{v_1\left(6\kappa\lambda^* + \lambda^* v_1^2 F^{(3)}(u^*) + 3 v_1^2 F''(u^*)^2\right)}{12 {\lambda^*}^2}\right) \tag{S104}$$

by Eq. (S99)-Eq. (S102) and where v_1 is arbitrary. Without loss of generality, we take $v_1 = 1$. Hence, we are interested in solutions of the form

$$u(t) = u^* + A(t) + \frac{F''(u^*)}{2\lambda^*}A^2(t) + \frac{\left(6\kappa\lambda^* + \lambda^* F^{(3)}(u^*) + 3F''(u^*)^2\right)}{12{\lambda^*}^2}A^3(t). \tag{S105}$$

$A(t)$ is a solution of Eq. (S91), given by

$$A(t) = \frac{\sqrt{\lambda^*}e^{\lambda(t-C_1)}}{\sqrt{\kappa e^{2\lambda^*(t-C_1)} - 1}}, \tag{S106}$$

where C_1 is an integration constant and $\kappa > e^{-2\lambda^*(t-C_1)}$. We shall return to this solution, after discussing the multidimensional analysis next.

Multidimensional systems

The generalisation of WNSA to multidimensional systems requires further machinery from calculus. Before we delve into the Notch-motivated two-dimensional system, we present the general Taylor expansion of vector-valued multivariable functions.

Consider a function $\mathbf{F}: \mathbb{R}^n \to \mathbb{R}^m$ given by $\mathbf{F}(\mathbf{u}) = (F_1(\mathbf{u}), ..., F_m(\mathbf{u}))$, where $\mathbf{u} = (u_0, ..., u_n)$. The general Kth-order Taylor expansion of $\mathbf{F}(\mathbf{u}+\mathbf{u}_0)$ about a point $\mathbf{u}_0 \in \mathbb{R}^n$ is given by

$$\mathbf{F}(\mathbf{u}+\mathbf{u}_0) \simeq \sum_{j=0}^{K} \frac{1}{j!}(D^j\mathbf{F})_{\mathbf{u}_0}[(\mathbf{u})^j], \tag{S107}$$

where the Frechet-derivative terms $(D^j\mathbf{F})_{\mathbf{u}_0}[(\mathbf{u})^j]$ may be written in vector form as

$$(D^j\mathbf{F})_{\mathbf{u}_0}[(\mathbf{u})^j] = \begin{pmatrix} \sum_{i_1,...,i_j=1}^{n} \frac{\partial^j F_1}{\partial u_{i_1}\cdots\partial u_{i_j}}(\mathbf{u}_0)(u_{i_1}\cdots u_{i_j}) \\ \vdots \\ \sum_{i_1,...,i_j=1}^{n} \frac{\partial^j F_m}{\partial u_{i_1}\cdots\partial u_{i_j}}(\mathbf{u}_0)(u_{i_1}\cdots u_{i_j}) \end{pmatrix} \tag{S108}$$

using the notation

$$\sum_{i_1,...,i_j=1}^{n} = \sum_{i_1=1}^{n}\cdots\sum_{i_j=1}^{n}. \tag{S109}$$

For a two-variable two-dimensional ($n = m = 2$) vector function $\mathbf{F}(\mathbf{u}) = (F_1(\mathbf{u}), F_2(\mathbf{u}))$, where $\mathbf{u} = (u_1, u_2)$, the third-order Taylor expansion of such function around $\mathbf{u}_0 = \mathbf{u}^* = (u_1^*, u_2^*)$ is given by

$$\begin{aligned}\mathbf{F}(\mathbf{u}) \simeq\ & (D^0\mathbf{F})_{\mathbf{u}^*}[(\mathbf{u}-\mathbf{u}^*)^0] + (D^1\mathbf{F})_{\mathbf{u}^*}[(\mathbf{u}-\mathbf{u}^*)^1] \\ & + \frac{1}{2}(D^2\mathbf{F})_{\mathbf{u}^*}[(\mathbf{u}-\mathbf{u}^*)^2] + \frac{1}{6}(D^3\mathbf{F})_{\mathbf{u}^*}[(\mathbf{u}-\mathbf{u}^*)^3],\end{aligned} \tag{S110}$$

which may be simplified as follows

$$(D^0\mathbf{F})_{\mathbf{u}^*}[(\mathbf{u}-\mathbf{u}^*)^0] = \mathbf{F}(\mathbf{u}^*) \tag{S111}$$

$$(D^1\mathbf{F})_{\mathbf{u}^*}[(\mathbf{u}-\mathbf{u}^*)^1] = \begin{pmatrix} \sum_{i_1=1}^{2} \frac{\partial F_1}{\partial u_{i_1}}(\mathbf{u}^*)\left[(u_{i_1}-u_{i_1}^*)\right] \\ \sum_{i_1=1}^{2} \frac{\partial F_2}{\partial u_{i_1}}(\mathbf{u}^*)\left[(u_{i_1}-u_{i_1}^*)\right] \end{pmatrix} = \mathbf{J}(\mathbf{u}^*)(\mathbf{u}-\mathbf{u}^*) \tag{S112}$$

$$(D^2\mathbf{F})_{\mathbf{u}^*}[(\mathbf{u}-\mathbf{u}^*)^2] = \begin{pmatrix} \sum_{i_1=1}^{2}\sum_{i_2=1}^{2} \frac{\partial^2 F_1}{\partial u_{i_1}\partial u_{i_2}}(\mathbf{u}^*)\left[(u_{i_1}-u_{i_1}^*)(u_{i_2}-u_{i_2}^*)\right] \\ \sum_{i_1=1}^{2}\sum_{i_2=1}^{2} \frac{\partial^2 F_2}{\partial u_{i_1}\partial u_{i_2}}(\mathbf{u}^*)\left[(u_{i_1}-u_{i_1}^*)(u_{i_2}-u_{i_2}^*)\right] \end{pmatrix} \tag{S113}$$

$$= \begin{pmatrix} (\mathbf{u}-\mathbf{u}^*)^T\mathbf{H}_1(\mathbf{u}^*)(\mathbf{u}-\mathbf{u}^*) \\ (\mathbf{u}-\mathbf{u}^*)^T\mathbf{H}_2(\mathbf{u}^*)(\mathbf{u}-\mathbf{u}^*) \end{pmatrix} \tag{S114}$$

$$\begin{aligned}&(D^3\mathbf{F})_{\mathbf{u}^*}[(\mathbf{u}-\mathbf{u}^*)^3] \\ &= \begin{pmatrix} \sum_{i_1=1}^{2}\sum_{i_2=1}^{2}\sum_{i_3=1}^{2} \frac{\partial^3 F_1}{\partial u_{i_1}\partial u_{i_2}\partial u_{i_3}}(\mathbf{u}^*)\left[(u_{i_1}-u_{i_1}^*)(u_{i_2}-u_{i_2}^*)(u_{i_3}-u_{i_3}^*)\right] \\ \sum_{i_1=1}^{2}\sum_{i_2=1}^{2}\sum_{i_3=1}^{2} \frac{\partial^3 F_2}{\partial u_{i_1}\partial u_{i_2}\partial u_{i_3}}(\mathbf{u}^*)\left[(u_{i_1}-u_{i_1}^*)(u_{i_2}-u_{i_2}^*)(u_{i_3}-u_{i_3}^*)\right] \end{pmatrix}.\end{aligned} \tag{S115}$$

$\mathbf{J}$ is the Jacobian matrix of $\mathbf{F}$, and $\mathbf{H}_1$ and $\mathbf{H}_2$ are the Hessian matrices of functions F_1 and F_2, respectively. The third derivative term given by $(D^3\mathbf{F})_{\mathbf{u}^*}[(\mathbf{u}-\mathbf{u}^*)^3]$ has no straightforward simplification. Hence

$$\begin{aligned}\mathbf{F}(\mathbf{u}) \simeq\ & \mathbf{F}(\mathbf{u}^*)+\mathbf{J}(\mathbf{u}^*)(\mathbf{u}-\mathbf{u}^*) \\ & +\frac{1}{2}\begin{pmatrix}(\mathbf{u}-\mathbf{u}^*)^T\mathbf{H}_1(\mathbf{u}^*)(\mathbf{u}-\mathbf{u}^*) \\ (\mathbf{u}-\mathbf{u}^*)^T\mathbf{H}_2(\mathbf{u}^*)(\mathbf{u}-\mathbf{u}^*)\end{pmatrix}+\frac{1}{6}(D^3\mathbf{F})_{\mathbf{u}^*}[(\mathbf{u}-\mathbf{u}^*)^3]. \end{aligned} \tag{S116}$$

In the following, we drop the differential evaluation at the homogeneous state $\mathbf{u}^*$ when convenient. Again, we fix $K=3$ and consider solutions to

$$\frac{d\mathbf{u}}{dt}=\mathbf{F}(\mathbf{u}) \tag{S117}$$

of the form

$$\mathbf{u}(t)=\mathbf{v}_0+\mathbf{v}_1A(t)+\mathbf{v}_2A^2(t)+\mathbf{v}_3A^3(t)+O(A^4) \tag{S118}$$

$$=\begin{pmatrix}v_{01}\\ v_{02}\end{pmatrix}+\begin{pmatrix}v_{11}\\ v_{12}\end{pmatrix}A(t)+\begin{pmatrix}v_{21}\\ v_{22}\end{pmatrix}A^2(t)+\begin{pmatrix}v_{31}\\ v_{32}\end{pmatrix}A^3(t)+O(A^4), \tag{S119}$$

where $A(t)$ satisfies Eq. (S91) and $\mathbf{v}_m$ $(0\le m\le 3)$ are now constant vectors. Using the general Taylor expansion Eq. (S116), we now aim to find the tuples (b_0,b_1,b_2,b_3), $(v_{01},v_{11},v_{21},v_{31})$ and $(v_{02},v_{12},v_{22},v_{32})$ such that the weakly nonlinear approximation holds in the two-dimensional system.
Substituting Eq. (S119) into $\frac{d\mathbf{u}}{dt}$ we get, for $j\in\{1,2\}$,

$$\begin{aligned}\frac{du_j}{dt}=\ & b_0v_{1,j}+(b_1v_{1,j}+2b_0v_{2,j})\,A(t)+(b_2v_{1,j}+2b_1v_{2,j}+3b_0v_{3,j})\,A^2(t) \\ & +(b_3v_{1,j}+2b_2v_{2,j}+3b_1v_{3,j})\,A^3(t)+O(A^4).\end{aligned} \tag{S120}$$

Given Eq. (S116), we have that the Taylor expansion of $\mathbf{F}_A(A)\equiv\mathbf{F}(\mathbf{u})$ around $A=0$ satisfies

$$F_{Aj}(A)=F_j(\mathbf{v}_1A(t)+\mathbf{v}_2A^2(t)+\mathbf{v}_3A^3(t)) \tag{S121}$$

$$\simeq\mathbf{T}_{0,j}(\mathbf{v})+\mathbf{T}_{1,j}(\mathbf{v})A(t)+\mathbf{T}_{2,j}(\mathbf{v})A^2(t)+\mathbf{T}_{3,j}(\mathbf{v})A^3(t)+O(A^4), \tag{S122}$$

where $\mathbf{v}\equiv(\mathbf{v}_0,\mathbf{v}_1,\mathbf{v}_2,\mathbf{v}_3)$ and

$$\mathbf{T}_{0,j}(\mathbf{v})=F_j=0 \tag{S123}$$

$$\mathbf{T}_{1,j}(\mathbf{v})=v_{11}\frac{\partial F_j}{\partial u_1}+v_{12}\frac{\partial F_j}{\partial u_2} \tag{S124}$$

$$\mathbf{T}_{2,j}(\mathbf{v})=v_{21}\frac{\partial F_j}{\partial u_1}+v_{22}\frac{\partial F_j}{\partial u_2}+\frac{v_{11}^2}{2}\frac{\partial^2F_j}{\partial u_1^2}+\frac{v_{12}^2}{2}\frac{\partial^2F_j}{\partial u_2^2}+v_{11}v_{12}\frac{\partial^2F_j}{\partial u_1\partial u_2} \tag{S125}$$

$$\begin{aligned}\mathbf{T}_{3,j}(\mathbf{v})=\ & v_{31}\frac{\partial F_j}{\partial u_1}+v_{32}\frac{\partial F_j}{\partial u_2} \\ & +v_{11}v_{21}\frac{\partial^2F_j}{\partial u_1^2}+v_{12}v_{22}\frac{\partial^2F_j}{\partial u_2^2}+(v_{21}v_{12}+v_{11}v_{22})\frac{\partial^2F_j}{\partial u_1\partial u_2} \\ & +\frac{v_{11}^3}{6}\frac{\partial^3F_j}{\partial u_1^3}+\frac{v_{12}^3}{6}\frac{\partial^3F_j}{\partial u_2^3}+\frac{v_{11}^2v_{12}}{2}\frac{\partial^3F_j}{\partial u_1^2\partial u_2}+\frac{v_{11}v_{12}^2}{2}\frac{\partial^3F_j}{\partial u_1\partial u_2^2}.\end{aligned} \tag{S126}$$

Equating the coefficients of Eq. (S120) and Eq. (S122) yields an intricate system of 8 equations and 10 variables (excluding the trivial cases $v_{01}=u_1^*$ and $v_{02}=u_2^*$), leading to a series of relations between b_m and $v_{m',j}$ $(1\le m,m'\le 3,\ j\in\{1,2\})$. By defining $\mathbf{T}_m\equiv(\mathbf{T}_{m,1},\mathbf{T}_{m,2})^T$, for $0\le m\le K$, we have

$$\mathbf{T}_0(\mathbf{v})=\mathbf{0} \tag{S127}$$

$$\mathbf{T}_1(\mathbf{v})=\mathbf{J}(\mathbf{u}^*)\mathbf{v}_1 \tag{S128}$$

$$\mathbf{T}_2(\mathbf{v})=\mathbf{J}(\mathbf{u}^*)\mathbf{v}_2+\frac{1}{2}\begin{pmatrix}\mathbf{v}_1^T\mathbf{H}_1(\mathbf{u}^*)\mathbf{v}_1\\ \mathbf{v}_1^T\mathbf{H}_2(\mathbf{u}^*)\mathbf{v}_1\end{pmatrix} \tag{S129}$$

$$\mathbf{T}_3(\mathbf{v})=\mathbf{J}(\mathbf{u}^*)\mathbf{v}_3+\frac{1}{2}\begin{pmatrix}\mathbf{v}_2^T\mathbf{H}_1(\mathbf{u}^*)\mathbf{v}_1\\ \mathbf{v}_2^T\mathbf{H}_2(\mathbf{u}^*)\mathbf{v}_1\end{pmatrix}+\frac{1}{6}(D^3\mathbf{F})_{\mathbf{u}^*}[(\mathbf{v}_1)^3] \tag{S130}$$

and so the coefficient relations are given by

$$b_0\mathbf{v}_1 = \mathbf{0} \tag{S131}$$

$$b_1\mathbf{v}_1 = \mathbf{J}(\mathbf{u}^*)\mathbf{v}_1 \tag{S132}$$

$$(2b_1\mathbf{I}-\mathbf{J}(\mathbf{u}^*))\mathbf{v}_2 = \frac{1}{2}\begin{pmatrix}\mathbf{v}_1^T\mathbf{H}_1(\mathbf{u}^*)\mathbf{v}_1\\ \mathbf{v}_1^T\mathbf{H}_2(\mathbf{u}^*)\mathbf{v}_1\end{pmatrix} - b_2\mathbf{v}_1 \tag{S133}$$

$$(3b_1\mathbf{I}-\mathbf{J}(\mathbf{u}^*))\mathbf{v}_3 = \frac{1}{2}\begin{pmatrix}\mathbf{v}_2^T\mathbf{H}_1(\mathbf{u}^*)\mathbf{v}_1\\ \mathbf{v}_2^T\mathbf{H}_2(\mathbf{u}^*)\mathbf{v}_1\end{pmatrix} + \frac{1}{6}(D^3\mathbf{F})_{\mathbf{u}^*}[(\mathbf{v}_1)^3] - b_3\mathbf{v}_1 - 2b_2\mathbf{v}_2. \tag{S134}$$

We now motivate a choice for $\mathbf{v}_1 = (v_{11}, v_{12})$. Notice first that this method mimics the LSA approach when $K = 1$, $\mathbf{v}_0 = \mathbf{u}^*$ and $b_0 = 0$. Eq. (S132) holds provided b_1 and $\mathbf{v}_1$ are an eigenvalue and a corresponding eigenvector of the Jacobian matrix $\mathbf{J}$ of $\mathbf{F}$ evaluated at $\mathbf{u}^*$. Assuming $A(t) = e^{\lambda^* t}$, we take $b_1 = \lambda^*$ and $\mathbf{v}_1 = \mathbf{v}^*$, where λ^* is the fastest growth rate and $\mathbf{v}^*$ its corresponding eigenvector (which is not unique), as in Eq. (49)-Eq. (50). The general solution would, in this case, correspond to the asymptotic solution in Eq. (51). The remaining coefficient relations between Eq. (S120) and Eq. (S122) follow from this choice of $\mathbf{v}_1$ via the other coefficient identities.

WNSA of Notch-Delta signalling dynamics

In the following, we take $\mathbf{u}_i = (n_i, d_i)$ and

$$\frac{d\mathbf{u}_i}{dt} = \mathbf{F}(n_i, d_i) = \begin{pmatrix}F_1(n_i, d_i)\\ F_2(n_i, d_i)\end{pmatrix} = \begin{pmatrix}f(\langle d_i\rangle) - n_i\\ \nu(g(n_i) - d_i)\end{pmatrix} \tag{S135}$$

for each cell i. We may interchange cell indexation between i and (j,k) as convenient, as well as the conditions $r \neq i$, $r \neq (j,k)$ and $\Delta jk \in S$ (see previous sections for details on such notation). As previously seen, we aim to extend the linear approach to consider solutions of Eq. (S135) in the harmonic form

$$\mathbf{u}_i(t) = \mathbf{u}^* + \mathbf{v}_1^i A(t) + \mathbf{v}_2^i A^2(t) + \mathbf{v}_3^i A^3(t) + O(A^4), \tag{S136}$$

where

$$\frac{dA}{dt}(t) = \lambda^* A(t) - \kappa A^3(t) + O(A^5). \tag{S137}$$

We have seen that discrete Fourier transforms Eq. (S38)-Eq. (S41) may be used to decouple the original system of $2NM$ equations (NM is the number of cells on a $N \times M$ hexagonal lattice). We recall from Eq. (S37) that, when $K = 1$, linearisation led to

$$\frac{d\mathbf{u}_i}{dt} \simeq \mathbf{J}\mathbf{u}_i + \sum_{r\neq i}\mathbf{J}^r\mathbf{u}_r, \tag{S138}$$

which was then rewritten by introducing the following coupling function derived from the Jacobian matrix (with $i \equiv (j,k)$ in the case of a two-dimensional lattice)

$$\mathbf{\Omega}_{\bar{q},\bar{p}} \equiv \mathbf{\Omega}_{\bar{q},\bar{p}}(q,p) = \sum_{\Delta jk\in S}\mathbf{J}^{\Delta jk}e^{2\pi\mathrm{i}(\bar{q}\Delta j + \bar{p}\Delta k)} \tag{S139}$$

leading to the decoupled linearised problem

$$\frac{d}{dt}\begin{pmatrix}\xi_{q,p}\\ \eta_{q,p}\end{pmatrix} \simeq \mathbf{L}_{\bar{q},\bar{p}}\begin{pmatrix}\xi_{q,p}\\ \eta_{q,p}\end{pmatrix}, \tag{S140}$$

where $\mathbf{L}_{\bar{q},\bar{p}} = \mathbf{J} + \mathbf{\Omega}_{\bar{q},\bar{p}}$. Given exponential-based solutions of the linearised Eq. (S140), our problem relied then on minimising $\mathbf{\Omega}_{\bar{q},\bar{p}}$ in order to find the fastest growing modes $(\bar{q},\bar{p})$. This problem changes and becomes relatively trickier in the case of WNSA due to multiple mathematical obstacles, as discussed below.

The extension of Eq. (S139) to the weakly nonlinear solution Eq. (S136) is not trivial and, in general, we should not expect a higher-order extension of decomposition Eq. (S138) to occur due to cross-derivative terms. To see this, take a general function $\mathbf{F}(\mathbf{u}) = (F_1(\mathbf{u}), F_2(\mathbf{u}))$, where $\mathbf{u} = (n_i, d_i, d_{i-1}, d_{i+1})$ (corresponding, for example, to the one-dimensional ring of cells in Example 1.2). The second-order term of the Taylor expansion for F_1 around $\mathbf{u}^*$ includes the cross-derivative terms

$$n_i d_{i-1}\frac{\partial^2 F_1}{\partial n_i \partial d_{i-1}} + n_i d_{i+1}\frac{\partial^2 F_1}{\partial n_i \partial d_{i+1}} + d_i d_{i-1}\frac{\partial^2 F_1}{\partial d_i \partial d_{i-1}} + d_i d_{i+1}\frac{\partial^2 F_1}{\partial d_i \partial d_{i+1}}. \tag{S141}$$

Such terms would naturally complicate the decoupling of the relative-index terms d_{i-1} and d_{i+1}. However, in our case, with $\mathbf{F}$ given by Eq. (S135), the derivatives in Eq. (S141) are all zero (and consequently any higher-order cross-derivatives). Thus we may hope for a smoother decoupling. Hence, according to Eq. (S107) and generalising Eq. (S138), we may write

$$\frac{d\mathbf{u}_i}{dt} \simeq \sum_{j=0}^{K} \frac{1}{j!}(D^j\mathbf{F})_{\mathbf{u}^*}[(\mathbf{u}_i)^j] + \sum_{r\neq i}\left[\sum_{j=0}^{K}\frac{1}{j!}(D^j\mathbf{F})_{\mathbf{u}^*}[(\mathbf{u}_r)^j]\right]. \tag{S142}$$

All that remains now is to find a simplification of the right-hand side term of Eq. (S142) so that the decoupling is complete and we may write the entire expression as a function of (n_i, d_i). In other words, we aim to determine the coefficient contribution of the coupling term to Eq. (S131)-Eq. (S134).
To simplify notation and considering the candidate solution Eq. (S136), we begin by Taylor-expanding $\mathbf{F}_A(A) \equiv \mathbf{F}(\mathbf{u})$ around $A = 0$, rewriting Eq. (S142) as follows

$$\mathbf{F}_A(A) \simeq \sum_{m=0}^{3}\mathbf{T}_m^i(\mathbf{v})A^m(t) + \sum_{r\neq i}\sum_{m=0}^{3}\mathbf{T}_m^r(\mathbf{v})A^m(t). \tag{S143}$$

With $i \equiv (j,k)$, we apply the following change of variables (Fourier transform)

$$\boldsymbol{\zeta}_{q,p} = \frac{1}{NM}\sum_{k=1}^{M}\sum_{j=1}^{N}\mathbf{u}_{j,k}e^{-2\pi\mathrm{i}(\bar{q}j+\bar{p}k)} \tag{S144}$$

$$= \frac{1}{NM}\sum_{k=1}^{M}\sum_{j=1}^{N}\left[\mathbf{u}^* + \mathbf{v}_1^{j,k}A(t) + \mathbf{v}_2^{j,k}A^2(t) + \mathbf{v}_3^{j,k}A^3(t)\right]e^{-2\pi\mathrm{i}(\bar{q}j+\bar{p}k)} \tag{S145}$$

$$= \sum_{m=0}^{3}\boldsymbol{\zeta}_{q,p}^m, \tag{S146}$$

where

$$\boldsymbol{\zeta}_{q,p}^m \equiv \frac{1}{NM}\sum_{k=1}^{M}\sum_{j=1}^{N}\mathbf{v}_m^{j,k}A^m(t)e^{-2\pi\mathrm{i}(\bar{q}j+\bar{p}k)}. \tag{S147}$$

From the methods discussed before, it follows that

$$\frac{d\boldsymbol{\zeta}_{q,p}}{dt} = \frac{1}{NM}\sum_{k=1}^{M}\sum_{j=1}^{N}\frac{d\mathbf{u}_{j,k}}{dt}e^{-2\pi\mathrm{i}(\bar{q}j+\bar{p}k)} \tag{S148}$$

$$= \frac{1}{NM}\sum_{k=1}^{M}\sum_{j=1}^{N}\left[\sum_{m=0}^{3}\mathbf{T}_m^{j,k}(\mathbf{v})A^m(t) + \sum_{r\neq(j,k)}\sum_{m=0}^{3}\mathbf{T}_m^r(\mathbf{v})A^m(t)\right]e^{-2\pi\mathrm{i}(\bar{q}j+\bar{p}k)}. \tag{S149}$$

We now aim to decouple the terms

$$\boldsymbol{\Omega}_{\bar{q},\bar{p}}^{3,m}(\mathbf{v}) \equiv \frac{1}{NM}\sum_{k=1}^{M}\sum_{j=1}^{N}\left[\sum_{r\neq(j,k)}\mathbf{T}_m^r(\mathbf{v})A^m(t)\right]e^{-2\pi\mathrm{i}(\bar{q}j+\bar{p}k)} \tag{S150}$$

for each $0 \leq m \leq 3$:

- $m = 0$. $\boldsymbol{\Omega}_{\bar{q},\bar{p}}^{3,0}(\mathbf{v}) = \mathbf{0}$.
- $m = 1$. This case mimics the deduction of Eq. (S42), as follows

$$\boldsymbol{\Omega}_{\bar{q},\bar{p}}^{3,1}(\mathbf{v}) = \frac{1}{NM}\sum_{k=1}^{M}\sum_{j=1}^{N}\left[\sum_{r\neq(j,k)}\mathbf{T}_1^r(\mathbf{v})A(t)\right]e^{-2\pi\mathrm{i}(\bar{q}j+\bar{p}k)} \tag{S151}$$

$$= \frac{A(t)}{NM}\sum_{k=1}^{M}\sum_{j=1}^{N}\left[\sum_{r\neq(j,k)}\mathbf{J}^r\mathbf{v}_1^r\right]e^{-2\pi\mathrm{i}(\bar{q}j+\bar{p}k)} \tag{S152}$$

$$= \frac{A(t)}{NM} \sum_{\Delta jk \in S} \mathbf{J}^{\Delta jk} \left[\sum_{k=1}^{M} \sum_{j=1}^{N} \mathbf{v}_1^{(j,k)+\Delta jk} e^{-2\pi \mathrm{i}(\bar{q}j+\bar{p}k)} \right] \tag{S153}$$

$$= \sum_{\Delta jk \in S} \mathbf{J}^{\Delta jk} \boldsymbol{\zeta}^1_{q,p} e^{2\pi \mathrm{i}(\bar{q}\Delta j+\bar{p}\Delta k)} \tag{S154}$$

$$= \boldsymbol{\zeta}^1_{q,p} \boldsymbol{\Omega}_{\bar{q},\bar{p}}, \tag{S155}$$

where $\boldsymbol{\Omega}_{\bar{q},\bar{p}}$ is given by Eq. (S139).

- $m = 2$. We have

$$\boldsymbol{\Omega}^{3,2}_{\bar{q},\bar{p}}(\mathbf{v}) = \frac{1}{NM} \sum_{k=1}^{M} \sum_{j=1}^{N} \left[\sum_{r \neq (j,k)} \mathbf{T}^r_2(\mathbf{v}) A^2(t) \right] e^{-2\pi \mathrm{i}(\bar{q}j+\bar{p}k)} \tag{S156}$$

$$= \frac{A^2(t)}{NM} \sum_{k=1}^{M} \sum_{j=1}^{N} \left[\sum_{r \neq (j,k)} \left[\mathbf{J}^r \mathbf{v}^r_2 + \frac{1}{2} \begin{pmatrix} \mathbf{v}^r_1{}^T \mathbf{H}^r_1 \mathbf{v}^r_1 \\ \mathbf{v}^r_1{}^T \mathbf{H}^r_2 \mathbf{v}^r_1 \end{pmatrix} \right] \right] e^{-2\pi \mathrm{i}(\bar{q}j+\bar{p}k)}. \tag{S157}$$

While the term involving $\mathbf{J}^r$ can be simplified like the $m = 1$ case, the other term yields a higher level of complexity (Remark 2.1). To see this, we exclude both $A^2(t)$ and the index sum, and track the first component of such term, as follows

$$\frac{1}{2NM} \sum_{k=1}^{M} \sum_{j=1}^{N} \left[{v^r_{11}}^2 \frac{\partial^2 F_1}{\partial {v^r_{11}}^2} + {v^r_{12}}^2 \frac{\partial^2 F_1}{\partial {v^r_{12}}^2} + 2 v^r_{11} v^r_{12} \frac{\partial^2 F_1}{\partial v^r_{11} \partial v^r_{12}} \right] e^{-2\pi \mathrm{i}(\bar{q}j+\bar{p}k)}. \tag{S158}$$

Given the type of variable change Eq. (S144), we do not expect, in general, to be able to manipulate Eq. (S158) so that it is written in terms of $\boldsymbol{\zeta}^2_{q,p}$ in order to second-order decouple the original system. The same can be argued for the case $m = 3$.

- $m = 3$. See $m = 2$ and discussion below.

Given the complexity generated by the cases $m = 2$ and $m = 3$ any methodology as systematic as the linear case seems to be out of reach. Therefore, WNSA is insufficient to describe quantitative dynamics of long-range signalling, without further assumptions.

We have presented the main methodology behind a potential framework for weakly nonlinear analysis of translationally invariant Notch-Delta systems. Considering different changes of variables or taking cell-dependent amplitude functions $A_{q,p}(t)$ could help in simplifying decoupling. In the main text, we discuss an additional multiscale alternative to our LSA and WNSA approaches for studying Notch-Delta systems, as well as some suggestions for how these methodologies might be improved.

Remark 2.1 (High-order decoupling) Part of the problem in decoupling the second-order term in Eq. (S156) relies on understanding how a term in the form

$$\sum_{j=1}^{N} a_j^2 e^{\frac{2\pi \mathrm{i}}{N} j} \tag{S159}$$

relates to the quadratic form

$$\left(\sum_{j=1}^{N} a_j e^{\frac{2\pi \mathrm{i}}{N} j} \right)^2, \tag{S160}$$

where $a_j = v^r_{11}$, for example. While a linear manipulation does not seem promising in this case (compared to the $m = 1$ case), alternative approaches might hint at further simplification.

Supplementary Note 3: Simulation parameters

Table 1 shows the model parameters used in the simulations shown in the main text. In all simulations, $h = k = 6$, $\nu = 1$, and the initial conditions $n_i(0)$ and $d_i(0)$ have arbitrary values around the respective homogeneous steady state (n^*, d^*): $n_i(0) \sim N(n^*, 0.01)$ and $d_i(0) \sim N(d^*, 0.01)$.

Figures	p_ℓ	ϵ	$\log_{10} r_t$	$\log_{10} b$	(n^*, d^*)
1c-1f	2.1	$\{0, 0.2, 0.6, 1\}$	8	2	$(0.744, 0.055)$
2g-2i	2.1	$\{0.2, 0.4, 0.6\}$	8	2	$(0.744, 0.055)$
3	2.1	$\{0, 0.2, 0.4, 0.8, 1\}$	8	2	$(0.744, 0.055)$
4	2.1	$\{0.09, 0.78\}$	8	2	$(0.744, 0.055)$
5a-5c	4	$\{0.2, 0.4, 0.6\}$	8	2	$(0.744, 0.055)$
6a-6c	$\{2, 3, 4\}$	0.6	8	2	$(0.744, 0.055)$
7b-7e	2.1	0.6	8	2	$(0.744, 0.055)$
8	-	$\{0, 0.2, 0.4, 0.6, 0.8, 1\}$	-	-	-
9	-	$\{0, 0.2, 0.4, 0.6, 0.8, 1\}$	-	-	-
10 (row 1)	2.1	$\{0, 0.2, 0.4, 0.6, 0.8, 1\}$	1	2	$(0.420, 0.646)$
10 (row 2)	2.1	$\{0, 0.2, 0.4, 0.6, 0.8, 1\}$	2	1	$(0.671, 0.523)$
10 (row 3)	2.1	$\{0, 0.2, 0.4, 0.6, 0.8, 1\}$	5	1.3	$(0.781, 0.181)$

Table 1. Simulation parameters.

References

Aranson, I. S. and Kramer, L. The world of the complex Ginzburg–Landau equation. *Reviews of Modern Physics*, 74(1):99, 2002.

Binshtok, U. and Sprinzak, D. *Modeling the Notch response*. Springer, 2018.

Bozzini, B., Gambino, G., Lacitignola, D., Lupo, S., Sammartino, M., and Sgura, I. Weakly nonlinear analysis of Turing patterns in a morphochemical model for metal growth. *Computers & Mathematics with Applications*, 70(8):1948–1969, 2015.

Bracewell, R. N. and Bracewell, R. N. *The Fourier transform and its applications*, volume 31999. McGraw-Hill New York, 1986.

Collier, J. R., Monk, N. A., Maini, P. K., and Lewis, J. H. Pattern formation by lateral inhibition with feedback: a mathematical model of Delta-Notch intercellular signalling. *Journal of Theoretical Biology*, 183(4):429–446, 1996.

Doelman, A., Kaper, T. J., and Zegeling, P. A. Pattern formation in the one-dimensional Gray–Scott model. *Nonlinearity*, 10(2):523, 1997.

Hamada, H., Watanabe, M., Lau, H. E., Nishida, T., Hasegawa, T., Parichy, D. M., and Kondo, S. Involvement of Delta/Notch signaling in zebrafish adult pigment stripe patterning. *Development*, 141(2):318–324, 2014.

Kondo, S. How animals get their skin patterns: fish pigment pattern as a live Turing wave. *Systems Biology*, pages 37–46, 2009.

Lawrence, P. A. and Struhl, G. Morphogens, compartments, and pattern: lessons from Drosophila? *Cell*, 85(7):951–961, 1996.

Liu, S., Xia, S.-N., Yan, R., Wan, Z.-H., and Sun, D.-J. Linear and weakly nonlinear analysis of Rayleigh–Bénard convection of perfect gas with non-Oberbeck–Boussinesq effects. *Journal of Fluid Mechanics*, 845:141–169, 2018.

McGough, J. S. and Riley, K. Pattern formation in the Gray–Scott model. *Nonlinear Analysis: Real World Applications*, 5(1):105–121, 2004.

Meinhardt, H. Models of biological pattern formation: common mechanism in plant and animal development. *International Journal of Developmental Biology*, 40(1):123–134, 2003.

Meinhardt, H. Models of biological pattern formation: from elementary steps to the organization of embryonic axes. *Current Topics in Developmental Biology*, 81:1–63, 2008.

O'Dea, R. D. and King, J. R. Multiscale analysis of pattern formation via intercellular signalling. *Mathematical biosciences*, 231(2):172–185, 2011.

Stephenson, L. E. and Wollkind, D. J. Weakly nonlinear stability analyses of one-dimensional Turing pattern formation in activator-inhibitor/immobilizer model systems. *Journal of Mathematical Biology*, 33(8):771–815, 1995.

Stuart, J. On the non-linear mechanics of wave disturbances in stable and unstable parallel flows part 1. the basic behaviour in plane Poiseuille flow. *Journal of Fluid Mechanics*, 9(3):353–370, 1960.

Tabata, T. and Takei, Y. *Morphogens, their identification and regulation*. Oxford University Press for The Company of Biologists Limited, 2004.

Turing, A. The chemical basis of morphogenesis. *Philosophical Transactions of the Royal Society of London. Series B, Biological Sciences*, 237(641):37–72, 1952.

Vincent, J.-P. and Briscoe, J. Morphogens. *Current Biology*, 11(21):R851–R854, 2001.

Watson, J. On the non-linear mechanics of wave disturbances in stable and unstable parallel flows Part 2. The development of a solution for plane Poiseuille flow and for plane Couette flow. *Journal of Fluid Mechanics*, 9(3):371–389, 1960.

Wollkind, D. J. and Segel, L. A. A nonlinear stability analysis of the freezing of a dilute binary alloy. *Philosophical Transactions of the Royal Society of London. Series A, Mathematical and Physical Sciences*, 268(1191):351–380, 1970.

Wollkind, D. J. and Vislocky, M. An interfacial model equation for the bifurcation of solidification patterns during lpee processes. *Earth-Science Reviews*, 29(1-4):349–368, 1990.

Wollkind, D., Oulton, D., and Sriranganathan, R. A nonlinear stability analysis of a model equation for alloy solidification. *Journal de Physique*, 45(3):505–516, 1984.

Wollkind, D. J., Manoranjan, V. S., and Zhang, L. Weakly nonlinear stability analyses of prototype reaction-diffusion model equations. *Siam Review*, 36(2):176–214, 1994.